

SINGLE MOLECULE TRACKING STUDIES OF LOWER CRITICAL SOLUTION
TEMPERATURE TRANSITION BEHAVIOR IN POLY(N-ISOPROPYLACRYLAMIDE)

BY

LINDSAY C. C. ELLIOTT

DISSERTATION

Submitted in partial fulfillment of the requirements
for the degree of Doctor of Philosophy in Chemistry
in the Graduate College of the
University of Illinois at Urbana-Champaign, 2011

Urbana, Illinois

Doctoral Committee:

Professor Paul V. Braun, Chair
Professor Paul W. Bohn, Director of Research
Professor Alexander Scheeline
Professor Jeffrey S. Moore

ABSTRACT

In this thesis project, single molecule tracking, SMT, experiments in poly(*n*-isopropylacrylamide, pNIPAAm, were carried out using probe fluorophores that had partitioned into the polymer. When the pNIPAAm switches from expanded to collapsed at elevated temperatures, the free volume accessible to the diffusing molecules decreases and trajectories become more confined.

The work presented here can be best understood when organized into two categories- SMT trajectory analysis techniques and SMT results in pNIPAAm. In the first category, four techniques for analyzing SMT data – confinement level analysis, time series analysis and statistical analysis of lateral diffusion, multistate kinetics, and a newly developed, radius of gyration evolution analysis – were compared using a set of sample fluorophore trajectories obtained from diffuse probe in surface-tethered pNIPAAm. The five SMT trajectories, ranging in length from 41 to 273 steps, were all successfully analyzed by all four techniques, provided two important criteria were met: enough steps to define the motion were acquired in the trajectory, generally on the order of 50 steps, and the fast and slow diffusion coefficients differed by at least a factor of 5. Beyond that, the four trajectory analysis methods studied provide partially confirmatory and partially complementary information. SMT data resulting from more complex physical behavior may well benefit from using these techniques in succession to identify and sort populations.

In the second category of research, spatial and temporal heterogeneities in expanded and collapsed surface bound pNIPAAm films were studied by SMT experiments. Tracking data were analyzed using two methods involving radius of gyration (R_g) evolution and confinement

level calculations. These two analysis techniques were used to elucidate the range of behaviors displayed by hundreds of single molecules, which exhibited complex diffusion. The main conclusions that were drawn from this work were: 1) small molecule probe behavior in pNIPAAm is dictated by the free volume within surface tethered chains, and the distribution of probe behavior can be used to gain nanometer-scale information about the state of the polymer brush at high and low temperatures, 2) confinement level calculations and radius of gyration evolution results show a larger degree of confinement at higher temperatures, measurable in higher percentage of confined steps in a trajectory, longer periods of confined events, and smaller area of confined zones.

TABLE OF CONTENTS

Chapter 1- Introduction to hydrogels and lower critical solution temperature transitions in poly(N-isopropylacrylamide)	1
1.1 Hydrogels and stimulus-responsive polymers	1
1.2 Historical development of hydrogels and pNIPAAm	3
1.3 Lower critical solution temperature mechanism in pNIPAAm.....	5
1.4 Measuring spatial and temporal variations within pNIPAAm	7
1.5 References	10
 Chapter 2- Theoretical background for TIRF and investigations of pNIPAAm LCST response.....	17
2.1 Theoretical background for total internal reflection fluorescence	17
2.2 Phase transition in surface tethered pNIPAAm brushes	21
2.3 References	34
 Chapter 3- Surface tethered pNIPAAm brushes: preparation and characterization.....	39
3.1 Sample preparation.....	39
3.2 Sample characterization	43
3.3 Reaction time calibration	45
3.4 Single molecule tracking quality samples.....	48
3.5 Lower critical solution temperature characterization.....	50
3.6 References	53

Chapter 4- Single molecule fluorescence microscopy, optics, and automated tracking.....55

4.1	Single molecule fluorescence microscopy	55
4.2	Optics and fluorophores	57
4.3	Experimental achievement of total internal reflection	61
4.4	Instrument capabilities	63
4.5	Microscope characterization	64
4.6	Single molecule tracking software	68
4.7	Single molecule tracking considerations.....	73
4.8	References	74

Chapter 5- Single molecule tracking trajectory analysis76

5.1	Single molecule trajectory analysis.....	76
5.2	Analysis software	79
5.3	Single molecule diffusion simulations	79
5.4	Trajectory analysis of intermittent simulations.....	82
5.5	Experimental single molecule tracking data	99
5.6	Trajectory analysis of experimental data	101
5.7	Conclusions	117
5.8	References	118

Chapter 6- Variable temperature single molecule tracking in hydrated pNIPAAm121

6.1	Sample preparation, microscopy, and analysis techniques	123
-----	---	-----

6.2 Single molecule tracking in pNIPAAm results and discussion	125
6.3 Conclusions	141
6.4 References	142
 Chapter 7- Future directions	146
7.1 Summary	146
7.2 Future directions.....	146
7.3 References	151
 Appendix A	153
A.1 Supplementary material from Chapter 5	153
 Author's Curriculum Vitae.....	163

CHAPTER 1

INTRODUCTION TO HYDROGELS AND LOWER CRITICAL SOLUTION TEMPERATURE TRANSITIONS IN POLY(N-ISOPROPYLACRYLAMIDE)

The material of interest in this thesis, poly(N-isopropylacrylamide), pNIPAAm, exhibits a lower critical solution temperature (LCST) phase transition and is one of the most widely studied thermo-responsive polymers. Starting from a general point of view, this introduction will cover the applications, research history and basic LCST mechanism of pNIPAAm.

1.1 Hydrogels and stimulus-responsive polymers.

Hydrogels are a class of polymers that absorb large amounts of water, 10-1000X their dry weight without dissolving, when placed in contact with water.¹ In general, the hydrophilic character of these polymers is due to hydroxyl, carboxyl, amide, sulfide, or other polar functional groups that are covalently bound to the carbon backbone. When a hydrogel takes on water, the spacing between polymer chains increases and the material swells within the limits of molecular constraints, such as degree of crosslinking.

Adding a degree of control to the swelling, some hydrogels are sensitive to external perturbations, in which case they are called stimulus-responsive polymers, SRPs, or smart materials.²⁻⁴ SRPs can rapidly change configuration or dimension under the influence of temperature,⁵ electric field,⁶ solvent,^{7,8} light,⁹ magnetic field,¹⁰ moisture/water,¹¹ pH,¹² and specific molecules such as glucose, antigens, and enzymes.¹³ Stimulus-responsive properties have been observed in synthetic and naturally occurring polymers and in biochemical processes.^{14,15} Examples of natural responsive polysaccharides include alginate, which is Ca^{2+}

sensitive, found in brown algae, and used in molecular gastronomy;¹⁶ chitosan, which is pH sensitive, derived from chitin, and exhibits controllable biodegradability and biocompatibility;^{16,17} and κ -carrageenan, derived from red seaweed, which is K^+ responsive and selectively binds pullanase enzyme from *Bacillus acidopullulyticus*.¹⁸ In addition, dramatic temperature-induced conformational and structural changes resulting in the helix-to-coil transition of polypeptides were noted by Peller in 1959,¹⁹ Lifson and Roig in 1961,²⁰ Flory and Miller in 1966,²¹ and Poland and Scheraga in 1970.²²

As detailed below, biological applications were the impetus for pioneering hydrogel research in the 1950s. SRPs are attractive candidates for cell support, tissue engineering, and biomedical applications because they exhibit a similar degree of flexibility to natural tissue.²³ More recently, synthetic SRPs have been used in other applications such as smart textiles and apparel,^{24,25} intelligent medical instruments and auxiliaries,^{26,27} artificial muscles,²⁸ electrochemical devices,²⁹ robotics,³⁰ biomimetic devices,^{31,32} heat shrinkable materials for electronics packaging,³³ micro-electro-mechanical systems,³⁴ miniature manipulator,³⁵ and actuators and sensors.^{36,37}

Among the most attractive SRPs are those that respond to temperature. Temperature-responsive polymers have been used in smart textiles,³⁸ gene delivery vectors,³⁹ drug carriers and delivery media,⁴⁰⁻⁴³ and bioseparations.^{44,44-46} Despite evidence supporting the neurotoxicity of unreacted NIPAAm monomer,⁴⁷ pNIPAAm is a top candidate for controlled drug delivery due to the proximity of its LCST to body temperature.^{39,48} In addition, there are many examples of tailoring the responses of pNIPAAm copolymerized with other SRPs and modified with enzyme specific groups.³ Molecular gating is another attractive application for pNIPAAm in which several groups, including the Bohn group, have assembled devices with temperature-responsive

components to separate, isolate, react, and detect small samples and low concentrations of analytes.⁴⁹⁻⁵² Cell growth and release is also an area of technological interest for pNIPAAm, in which it has been used for cell scaffolds and synthetic extracellular matrices.^{3,53,54} Recently, pNIPAAm and its copolymers have been functionalized with recognition moieties (e.g., synthetic peptides) that interact with cell components. Ebara *et al.* used stimulus-responsive pNIPAAm-based copolymers to expose or mask arginine–glycine–aspartic acid recognition sequences for cell binding.⁵⁵ Other applications include temperature dependent protein binding sites and recyclable sequestration agents for heavy metals.^{56,57}

1.2 Historical development of hydrogels and pNIPAAm

Some of the earliest research interest in synthetic hydrogels and eventually SRPs began with Wichterle and Lim in the late 1950's.^{58,59} The authors were interested in using polymers in biological applications involving prolonged or permanent contact with living tissue, and they specifically focused on contact lenses. They were in search of suitable 'plastics' that possessed: inertness to normal biological processes, a structure permitting desired water content, and permeability to metabolites. Glycolmonomethacrylate was among the hydrogels that showed promise in the manufacture of contact lenses and arteries.

Although methacrylates were among the initially promising SRPs, pNIPAAm, first synthesized in 1956 by polymer scientists at Rohm & Haas and CIBA Ltd.,⁶⁰⁻⁶² quickly became popular. One reason for its popularity was the lower critical solution temperature, first noted for free pNIPAAm chains in solution in 1967 by Scarpa *et al.*⁶³ The authors observed an 'inverse temperature coefficient of solubility' that led to a precipitation from solution. Their report was closely followed in 1968 by Heskins and Guillet with a more extensive report on LCST

properties of pNIPAAm in solution.⁶⁴ The authors were inspired by three previous research reports on phase changes at increased temperatures in aqueous solutions of polar polymers in which the LCST phenomenon was attributed to entropy effects balancing out enthalpy factors in solution.⁶⁵⁻⁶⁷ Heskins and Guillet tested this theory by investigating the thermodynamic properties near the volume transition, however, the large, sharp changes in volume that were later characterized for pNIPAAm in solution^{51,68} were not noted.

The first large volume changes in a hydrogel were observed in crosslinked poly(acrylamide) gels in aqueous solution at -17°C by Tanaka *et al.* in 1977.⁶⁹ The following year, the full analyses of the thermodynamics underlying this reversible, controlled collapse were published by Tanaka.^{70,71} This analysis formed the basis for understanding the analogous collapse in pNIPAAm. According to Dagani,⁷² after initial skepticism due to the low transition temperature, these reports led to the acceptance of acrylamide gels as ‘smart’ polymers that responded to small changes in external stimuli by swelling or collapsing by orders of magnitude.

In 1984 Tanaka *et al.* followed the initial papers on stimulus-responsive polymers with a report of a discontinuous phase transition in pNIPAAm.⁷³ The authors show experimental evidence that follows mean-field theory predictions concerning the relationship between the type of volume transition – continuous or first order discontinuous – and the proportion of ionizable groups in the polymer network and the stiffness of the polymer chains. Further studies on the phase transition behavior of pNIPAAm were carried out in various solvents.⁷⁴

Soon after the LCST of pNIPAAm was established, new research areas sprung up as innovative materials were synthesized, such as temperature sensitive microgels that consisted of colloidal particles by Pelton and Chibante (1986).⁷⁵ In 1991, gels were mentioned by de Gennes in his Nobel acceptance speech as part of the importance of soft materials.⁷⁶ Interest continued

to swell, as evidenced by the number of publications about hydrogels and stimulus-responsive polymers shown in Figure 1.1.

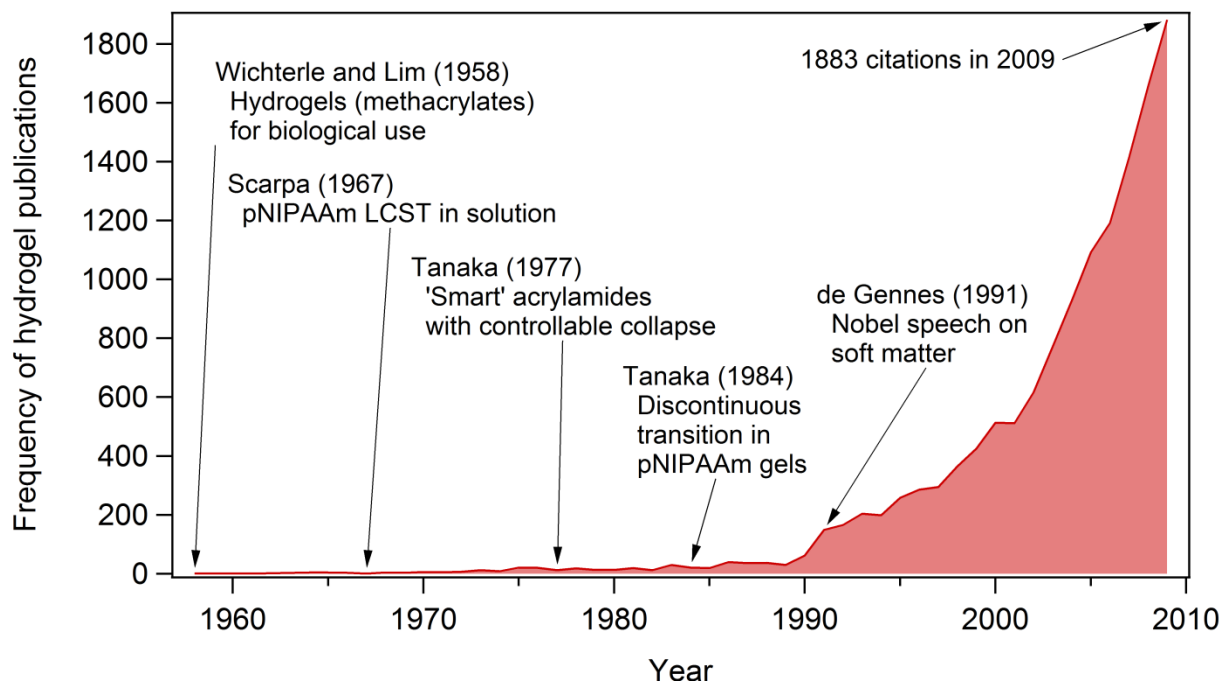


Figure 1.1: Histogram of publications on hydrogels between 1958 and 2009, bin size is 1 year.

1.3 Lower critical solution temperature mechanism in pNIPAAm

As discussed above, the identification of an LCST in pNIPAAm, chemical structure shown in Figure 1.2, was important for applications such as controlled drug delivery, molecular gating, and synthetic cell substrates. Seminal work on the deswelling mechanism in pNIPAAm, with an LCST close to body temperature of $\sim 32^{\circ}\text{C}$,³⁹ was carried out by Hoffman *et al.*⁷⁷ A notable characteristic of most polymers with an LCST is the presence of hydrophobic alkyl groups. These are the isopropyl groups in the case of pNIPAAm, which contribute to the interplay between hydrophilic and hydrophobic forces that results in a collapse of the polymer

chains as water is expelled from the material and a corresponding expansion as water is pulled into the material.⁷⁸

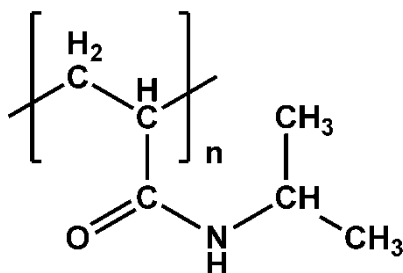


Figure 1.2: Chemical structure of poly(N-isopropylacrylamide), pNIPAAm.

At $T < T_{LCST}$, a hydrophilic regime dominates in which water molecules occupy large amounts of space around the polymer chains and the system exists in a state of hydrogen bonding between N-H and C=O on the amide functional groups and water. At $T > T_{LCST}$, the system shifts to a hydrophobic regime in which the bound water molecules are transported out of the polymer region. Intra- and inter-molecular hydrogen bonds form as the isopropyl groups fold in and the polymer collapses on itself.^{79,80} The phenomenon of collapse, schematically represented in Figure 1.3, can also be considered in thermodynamic terms as a balance between entropy effects (from dissolution of the polymer and from the ordered state of water molecules in hydrogen bonding with the polymer) and enthalpy effects (from inter- and intramolecular forces and from solvation of the system). At lower temperatures the enthalpic contributions dominate while at higher temperature the entropic influences dominate.^{15,39,78,81} This balance can be altered by modifying or copolymerizing the pNIPAAm with polar (increases LCST) or non-polar (decreases LCST) moieties.^{12,82-87}

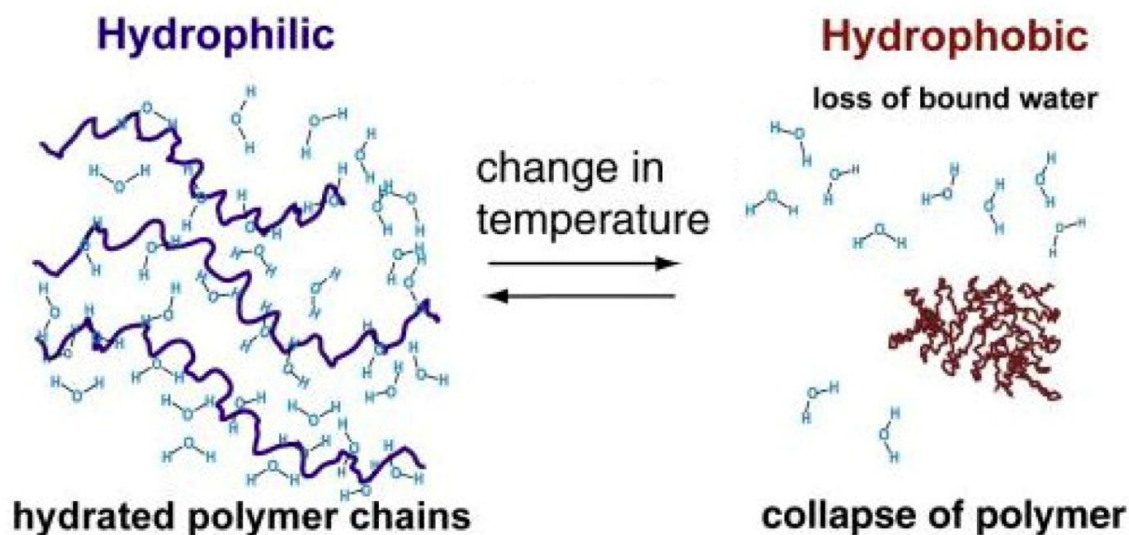


Figure 1.3: Inverse solubility collapse of a thermoresponsive polymer such as pNIPAAm, with a lower critical solution temperature transition. At higher temperature, bound water is expelled from the polymer and the polymer reorients to form intra- and inter-molecular hydrogen bonds. Modified from Pennadam *et al.*⁸⁸

1.4 Measuring spatial and temporal variations within pNIPAAm

Despite successes in building devices with temperature-responsive polymers, realizing the full potential of these technological advances requires a better understanding of the fundamental properties of pNIPAAm over small length and timescales. Instead of empirically determining temperature responses, detailed knowledge about the free volume perturbations is needed to fine-tune application-specific capabilities and understand material limitations. pNIPAAm brushes, in which the polymer chains are tethered to a substrate, creating a so called smart surface, are especially important for many applications. A complete picture of the variations in free volume is critically important, for example, in the loading and release of drug molecules on pNIPAAm coated chip or microspheres, as well as for the controlled flow of

analyte molecules through a pNIPAAm lined pore. Devices based on these structures would be greatly affected by changes in the distribution or the average of free volume. Although there are some qualitative similarities between the properties of pNIPAAm in solution or gel form and as a surface bound brush, critical differences exist. Therefore, the phase transition of pNIPAAm brushes continues to be an important topic of basic research.

Many techniques have been used to explore the LCST behavior in surface-tethered pNIPAAm – surface plasmon resonance, contact angle, nuclear magnetic resonance, quartz crystal microbalance, neutron reflectometry, sum frequency generation, infrared spectroscopy, microcalorimetry, atomic force microscopy, and surface force apparatus – and these important results are summarized in Section 2.2. The limitation of these techniques, however, is that data is either averaged over the material, providing no information on the nanometer length scale, or scanned point by point, taking minutes or more to collect. An *in situ* technique that probes individual locations simultaneously within the polymer would be extremely useful in expanding the breadth of knowledge about spatial and temporal heterogeneities. This type of analytical tool would leverage information about the differences in microenvironments within a given sample and the changes that take place over the course of the temperature transition.

Single molecule tracking, SMT, satisfies all these requirements and could be used to further characterize the temperature responses of pNIPAAm. SMT, developed within the last 15 years,⁸⁹⁻⁹⁵ uses fluorescence microscopy to follow the translational motion of diffuse populations of single probe molecules by assigning a spatial position to the average location of a molecule during a brief (10-100 ms typical) exposure to excitation radiation.⁹⁶ It has been applied to investigate a large range of physical and biological phenomena, including the translocation of molecular motors,^{97,98} molecular transport in thin silica sol-gel films,⁹⁹ membrane dynamics,¹⁰⁰

generating mechanisms in microvilli,¹⁰¹ and pore dynamics within polyacrylamide gels.¹⁰² Due to the adaptability of this method, SMT can be used to carry out simultaneous sampling of a large number of individual environments *in situ*. These attributes, in addition to sub-micron resolution, place SMT in a unique position to obtain dynamic measurements in LCST responsive polymers.

In addition using small molecules to explore the free volume in pNIPAAm is directly transferrable to many of the applications mentioned above, such as diffusion of drug molecules and analyte passing through pores, as these experiments investigate the chemical and physical interactions between the polymer chains and the probe molecules. Therefore, in this project, spatial and temporal heterogeneities in expanded and collapsed surface bound pNIPAAm films are studied by SMT.

The subsequent chapters in this thesis relate pertinent background information, experimental details, results, and conclusions. Chapter 2 includes background regarding total internal reflection fluorescence, the microscopy technique used in these experiments, and a literature review of the LCST response in pNIPAAm brushes. Chapter 3 describes the synthesis and characterization of the surface-tethered polymer brush samples, along with experimental considerations for single molecule tracking samples. Chapter 4 contains practical information regarding single molecule microscopy, including instrument design and construction and software-based tracking algorithms. Chapter 5 details four techniques for analyzing single molecule tracking data - confinement level analysis, time series analysis and statistical analysis of lateral diffusion, multistate kinetics, and a newly developed method, radius of gyration evolution analysis – and comparing them using a set of sample fluorophore trajectories. Chapter 6 explores the application of these techniques in the analysis of temperature dependent SMT

movies in pNIPAAm and the quantification of probe behavior that reflects nanometer scale information about the state of the polymer brush at $T > T_{LCST}$ and $T < T_{LCST}$. Finally, Chapter 7 contains suggestions about future projects and implications of this work.

1.5 References

- (1) Hoffman, A. S. *Adv. Drug Delivery. Rev.* **2002**, *54*, 3-12.
- (2) Ganji, F.; Vasheghani-Farahani, E. *Iran. Polym. J.* **2009**, *18*, 63-88.
- (3) Chaterji, S.; Kwon, I. K.; Park, K. *Prog. Polym. Sci.* **2007**, *32*, 1083-1122.
- (4) Fernandez-Barbero, A.; Suarez, I. J.; Sierra-Martin, B.; Fernandez-Nieves, A.; de las Nieves, F. J.; Marquez, M.; Rubio-Retama, J.; Lopez-Cabarcos, E. *Adv. Colloid Interface Sci.* **2009**, *147-48*, 88-108.
- (5) Gutowska, A.; Bae, Y. H.; Jacobs, H.; Feijen, J.; Kim, S. W. *Macromolecules* **1994**, *27*, 4167-4175.
- (6) Asaka, K.; Oguro, K. *J. Electroanal. Chem.* **2000**, *480*, 186-198.
- (7) Ionov, L.; Sidorenko, A.; Stamm, M.; Minko, S.; Zdyrko, B.; Klep, V.; Luzinov, I. *Macromolecules* **2004**, *37*, 7421-7423.
- (8) Edmondson, S.; Osborne, V. L.; Huck, W. T. S. *Chem. Soc. Rev.* **2004**, *33*, 14-22.
- (9) Yuan, W. F.; Jiang, G. Y.; Wang, J. X.; Wang, G. J.; Song, Y. L.; Jiang, L. *Macromolecules* **2006**, *39*, 1300-1303.
- (10) Xulu, P. M.; Filipcsei, G.; Zrinyi, M. *Macromolecules* **2000**, *33*, 1716-1719.
- (11) Casalbore-Miceli, G.; Chen, Y. S.; Girotto, E. M.; Li, Y.; Rinaldi, A. W.; Yang, M. J.; Zanelli, A. *Sens. Actuators, B* **2006**, *119*, 577-582.
- (12) Feil, H.; Bae, Y. H.; Feijen, J.; Kim, S. W. *Macromolecules* **1992**, *25*, 5528-5530.

- (13) Miyata, T.; Uragami, T.; Nakamae, K. *Adv. Drug Delivery. Rev.* **2002**, *54*, 79-98.
- (14) Jeong, B.; Gutowska, A. *Trends Biotechnol.* **2002**, *20*, 305-311.
- (15) Jeong, B.; Kim, S. W.; Bae, Y. H. *Adv. Drug Delivery. Rev.* **2002**, *54*, 37-51.
- (16) Kumar, A.; Yu, I.; Mattiasson, B. In *Affinity Chromatography: Methods and Protocols*; Zachariou, M., Ed. 1994; Vol. 421, p 37-52.
- (17) Khan, F.; Tare, R. S.; Oreffo, R. O. C.; Bradley, M. *Angew. Chem. Int. Edit.* **2009**, *48*, 978-982.
- (18) Roy, I.; Gupta, M. N. *J. Chromatogr. A* **2003**, *998*, 103-108.
- (19) Peller, L. *J. Phys. Chem.* **1959**, *63*, 1194-1199.
- (20) Lifson, S. *J. Chem. Phys.* **1961**, *34*, 1963-1974.
- (21) Flory, P. J.; Miller, W. G. *J. Mol. Biol.* **1966**, *15*, 284-297.
- (22) Liem, R. K. H.; Poland, D.; Scheraga, H. A. *J. Am. Chem. Soc.* **1970**, *92*, 5717-5724.
- (23) Byrne, M. E.; Park, K.; Peppas, N. A. *Adv. Drug Delivery. Rev.* **2002**, *54*, 149-161.
- (24) Chen, S. J.; Hu, J. L.; Liu, Y. Q.; Liem, H. M.; Zhu, Y.; Meng, Q. H. *Polym. Int.* **2007**, *56*, 1128-1134.
- (25) De Rossi, D.; Della Santa, A.; Mazzoldi, A. *Mater. Sci. Eng., C* **1999**, *7*, 31-35.
- (26) Lendlein, A.; Langer, R. *Science* **2002**, *296*, 1673-1676.
- (27) Metcalfe, A.; Desfaits, A. C.; Salazkin, I.; Yahia, L.; Sokolowski, W. M.; Raymond, J. *Biomaterials* **2003**, *24*, 491-497.
- (28) Sun, S.; Mak, A. F. T. *J. Polym. Sci., Part B: Polym. Phys.* **2001**, *39*, 236-246.
- (29) Avino, C.; Panero, S.; Scrosati, B. *J. Mater. Chem.* **1993**, *3*, 1259-1261.
- (30) Shahinpoor, M.; Bar-Cohen, Y.; Simpson, J. O.; Smith, J. *Smart Mater. Struct.* **1998**, *7*, R15-R30.

- (31) Calvert, P.; Rieke, P. *Chem. Mat.* **1996**, 8, 1715-1727.
- (32) Li, X. R.; Xie, J. W.; Yuan, X. Y.; Xia, Y. N. *Langmuir* **2008**, 24, 14145-14150.
- (33) Fukada, E.; Stephens, R. W. B.; Charlesby, A. *J. Phys. Chem. Solids* **1960**, 16, 53-59.
- (34) Gall, K.; Dunn, M. L.; Liu, Y. P.; Finch, D.; Lake, M.; Munshi, N. A. *Acta Mater.* **2002**, 50, 5115-5126.
- (35) Smela, E.; Inganas, O.; Lundstrom, I. *Science* **1995**, 268, 1735-1738.
- (36) Bar-Cohen, Y.; Zhang, Q. M. *MRS Bull.* **2008**, 33, 173-181.
- (37) Leng, J. S.; Lan, X.; Liu, Y. J.; Du, S. Y.; Huang, W. M.; Liu, N.; Phee, S. J.; Yuan, Q. *Appl Phys Lett* **2008**, 92, 3.
- (38) Liu, B. H.; Hu, J. L.; Meng, Q. H. *J. Biomed. Mater. Res. Part B* **2009**, 89B, 1-8.
- (39) Lin, C. C.; Metters, A. T. *Adv. Drug Delivery. Rev.* **2006**, 58, 1379-1408.
- (40) Yoshida, M.; Yang, J. S.; Kumakura, M.; Hagiwara, M.; Katakai, R. *Eur. Polym. J.* **1991**, 27, 997-1005.
- (41) Gutowska, A.; Bae, Y. H.; Feijen, J.; Kim, S. W. *J. Control. Release* **1992**, 22, 95-104.
- (42) Gutowska, A.; Bark, J. S.; Kwon, I. C.; Bae, Y. H.; Cha, Y.; Kim, S. W. *J. Control. Release* **1997**, 48, 141-148.
- (43) Coughlan, D. C.; Quilty, F. P.; Corrigan, O. I. *J. Control. Release* **2004**, 98, 97-114.
- (44) Guven, O.; Sen, M.; Karadag, E.; Saraydin, D. *Radiat. Phys. Chem.* **1999**, 56, 381-386.
- (45) Hoffman, A. S. *Clin. Chem.* **2000**, 46, 1478-1486.
- (46) Hoffman, A. S.; Stayton, P. S.; Bulmus, V.; Chen, G. H.; Chen, J. P.; Cheung, C.; Chilkoti, A.; Ding, Z. L.; Dong, L. C.; Fong, R.; Lackey, C. A.; Long, C. J.; Miura, M.; Morris, J. E.; Murthy, N.; Nabeshima, Y.; Park, T. G.; Press, O. W.; Shimoboji, T.;

- Shoemaker, S.; Yang, H. J.; Monji, N.; Nowinski, R. C.; Cole, C. A.; Priest, J. H.; Harris, J. M.; Nakamae, K.; Nishino, T.; Miyata, T. *J. Biomed. Mater. Res.* **2000**, *52*, 577-586.
- (47) Tanii, H.; Hashimoto, K. *Toxicol. Lett.* **1991**, *58*, 209-213.
- (48) Schild, H. G. *Prog. Polym. Sci.* **1992**, *17*, 163-249.
- (49) Lokuge, I.; Wang, X.; Bohn, P. W. *Langmuir* **2007**, *23*, 305-311.
- (50) Bohn, P. W. *Annu. Rev. Anal. Chem.* **2009**, *2*, 279-296.
- (51) Roy, I.; Gupta, M. N. *Chem. Biol.* **2003**, *10*, 1161-1171.
- (52) Meng, T.; Xie, R.; Chen, Y. C.; Cheng, C. J.; Li, P. F.; Ju, X. J.; Chu, L. Y. *J. Membr. Sci.* **2010**, *349*, 258-267.
- (53) Vernon, B.; Gutowska, A.; Kim, S. W.; Bae, Y. H. *Macromol. Symp.* **1996**, *109*, 155-167.
- (54) Okano, T.; Yamada, N.; Okuhara, M.; Sakai, H.; Sakurai, Y. *Biomaterials* **1995**, *16*, 297-303.
- (55) Ebara, M.; Yamato, M.; Aoyagi, T.; Kikuchi, A.; Sakai, K.; Okano, T. *Biomacromolecules* **2004**, *5*, 505-510.
- (56) Kawaguchi, H.; Fujimoto, K.; Mizuhara, Y. *Colloid Polym. Sci.* **1992**, *270*, 53-57.
- (57) Snowden, M. J.; Thomas, D.; Vincent, B. *Analyst* **1993**, *118*, 1367-1369.
- (58) Wichterle, O.; Lim, D. *Nature* **1960**, *185*, 117-118.
- (59) Lim, D.; Wichterle, O. *J. Polym. Sci.* **1958**, *29*, 579-584.
- (60) Sprecht, E. H.; Neuman, A.; Neher, H. T. *U.S. Pat. 2,773,063* **1956**.
- (61) CIBA Ltd. *Br. Pat. 746,747* **1956**.
- (62) Sprecht, E. H.; Neuman, A.; Neher, H. T. *U.S. Pat. 772,196* **1956**.
- (63) Scarpa, J. S.; Mueller, D. D.; Klotz, I. M. *J. Am. Chem. Soc.* **1967**, *89*, 6024-6030.
- (64) Heskins, M.; Guillet, J. E. *J. Macromol. Sci., Chem.* **1968**, *2*, 1441-1455.

- (65) Malcolm, G. N.; Rowlinson, J. S. *Trans. Faraday Soc.* **1957**, *53*, 921-931.
- (66) Dieu, D. A. *J. Polym. Sci.* **1954**, *12*, 417-438.
- (67) Uda, K.; Meyerhoff, G. *Makromol. Chem.* **1961**, *47*, 168-184.
- (68) *Polymer Data Handbook*; Mark, J. E., Ed.; Oxford University Press, Inc, 1999.
- (69) Tanaka, T.; Ishiwata, S.; Ishimoto, C. *Phys. Rev. Lett.* **1977**, *38*, 771-774.
- (70) Tanaka, T. *Phys. Rev. Lett.* **1978**, *40*, 820-823.
- (71) Tanaka, T. *Physical Review A* **1978**, *17*, 763-766.
- (72) Dagani, R. *Chem. Eng. News* **1997**, *75*, 26-37.
- (73) Hirokawa, Y.; Tanaka, T. *J. Chem. Phys.* **1984**, *81*, 6379-6380.
- (74) Amiya, T.; Hirokawa, Y.; Hirose, Y.; Li, Y.; Tanaka, T. *J. Chem. Phys.* **1987**, *86*, 2375-2379.
- (75) Pelton, R. H.; Chibante, P. *Coll. Surf.* **1986**, *20*, 247-256.
- (76) de Gennes, P.-G. *Nobel Lectures, Physics 1991-1995*; World Scientific Publishing Co.: Singapore, 1997.
- (77) Park, T. G.; Hoffman, A. S. *Biotechnol. Progr.* **1994**, *10*, 82-86.
- (78) Benec, L. S.; Snowden, M. J.; Chowdhry, B. Z. *Langmuir* **2002**, *18*, 6025-6030.
- (79) Cheng, X. H.; Canavan, H. E.; Stein, M. J.; Hull, J. R.; Kveskin, S. J.; Wagner, M. S.; Somorjai, G. A.; Castner, D. G.; Ratner, B. D. *Langmuir* **2005**, *21*, 7833-7841.
- (80) Miyamae, T.; Akiyama, H.; Yoshida, M.; Tamaoki, N. *Macromolecules* **2007**, *40*, 4601-4606.
- (81) Schmaljohann, D. *Adv. Drug Delivery. Rev.* **2006**, *58*, 1655-1670.
- (82) Spafford, M.; Polozova, A.; Winnik, F. M. *Macromolecules* **1998**, *31*, 7099-7102.

- (83) Principi, T.; Goh, C. C. E.; Liu, R. C. W.; Winnik, F. M. *Macromolecules* **2000**, *33*, 2958-2966.
- (84) Kujawa, P.; Goh, C. C. E.; Calvet, D.; Winnik, F. M. *Macromolecules* **2001**, *34*, 6387-6395.
- (85) Kujawa, P.; Liu, R. C. W.; Winnik, F. M. *J. Phys. Chem. B* **2002**, *106*, 5578-5585.
- (86) Hirotsu, S. *Adv. Polym. Sci.* **1993**, *110*, 1-26.
- (87) Irie, M. *Adv. Polym. Sci.* **1993**, *110*, 49-65.
- (88) Pennadam, S.; Firman, K.; Alexander, C.; Gorecki, D. *Journal of Nanobiotechnology* **2004**, *2*, 8.
- (89) Kusumi, A.; Sako, Y.; Yamamoto, M. *Biophys. J.* **1993**, *65*, 2021-2040.
- (90) Ishihara, A.; Jacobson, K. *Biophys. J.* **1993**, *65*, 1754-1755.
- (91) Ghosh, R. N.; Webb, W. W. *Biophys. J.* **1994**, *66*, 1301-1318.
- (92) Kubitscheck, U.; Wedekind, P.; Peters, R. *Biophys. J.* **1994**, *67*, 948-956.
- (93) Saxton, M. J. *Biophys. J.* **1995**, *69*, 389-398.
- (94) Cherry, R. J.; Wilson, K. M.; Triantafilou, K.; O'Toole, P.; Morrison, I. E. G.; Smith, P. R.; Fernandez, N. *J. Cell Biol.* **1998**, *140*, 71-79.
- (95) Simson, R.; Sheets, E. D.; Jacobson, K. *Biophys. J.* **1995**, *69*, 989-993.
- (96) Crocker, J. C.; Grier, D. G. *J. Colloid Interface Sci.* **1996**, *179*, 298-310.
- (97) Yildiz, A.; Forkey, J. N.; McKinney, S. A.; Ha, T.; Goldman, Y. E.; Selvin, P. R. *Science* **2003**, *300*, 2061-2065.
- (98) Yildiz, A.; Selvin, P. R. *Acc. Chem. Res.* **2005**, *38*, 574-582.
- (99) McCain, K. S.; Hanley, D. C.; Harris, J. M. *Anal. Chem.* **2003**, *75*, 4351-4359.
- (100) Saxton, M. J.; Jacobson, K. *Annu. Rev. Biophys. Biomolec. Struct.* **1997**, *26*, 373-399.

- (101) Coscoy, S.; Huguet, E.; Amblard, F. *Bull. Math. Biol.* **2007**, *69*, 2467-2492.
- (102) Dickson, R. M.; Norris, D. J.; Tzeng, Y. L.; Moerner, W. E. *Science* **1996**, *274*, 966-969.

CHAPTER 2

THEORETICAL BACKGROUND FOR TIRF AND INVESTIGATIONS OF PNIPAAm LCST RESPONSE

This chapter introduces salient points of fluorescence and total internal reflection fluorescence and summarizes literature concerning temperature induced transitions in surface tethered pNIPAAm brushes. It is intended to serve as background for the main topics covered in this thesis. For more comprehensive sources the cited references should be consulted.

The first two topics included in this chapter pertain to the microscopy technique used in collecting later SMT data. First the basic aspects of fluorescence are reviewed, followed by theoretical and practical details regarding total internal reflection fluorescence.

2.1 Theoretical background for total internal reflection fluorescence

2.1.1 Fluorescence. Fluorescence is a process in which a molecule, called a fluorophore, is excited from the electronic ground state to an excited state by absorbing photons of a specific energy. From the excited state there are several pathways for releasing the excess energy, one of which is the emission of photons of lower energy from the excitation light, as illustrated in Figure 2.1. A major application of this phenomenon is to use the characteristic excitation and emission maxima of a specific fluorophore to identify parts of a sample that exhibit native fluorescence or that harbor inserted synthetic fluorophores.

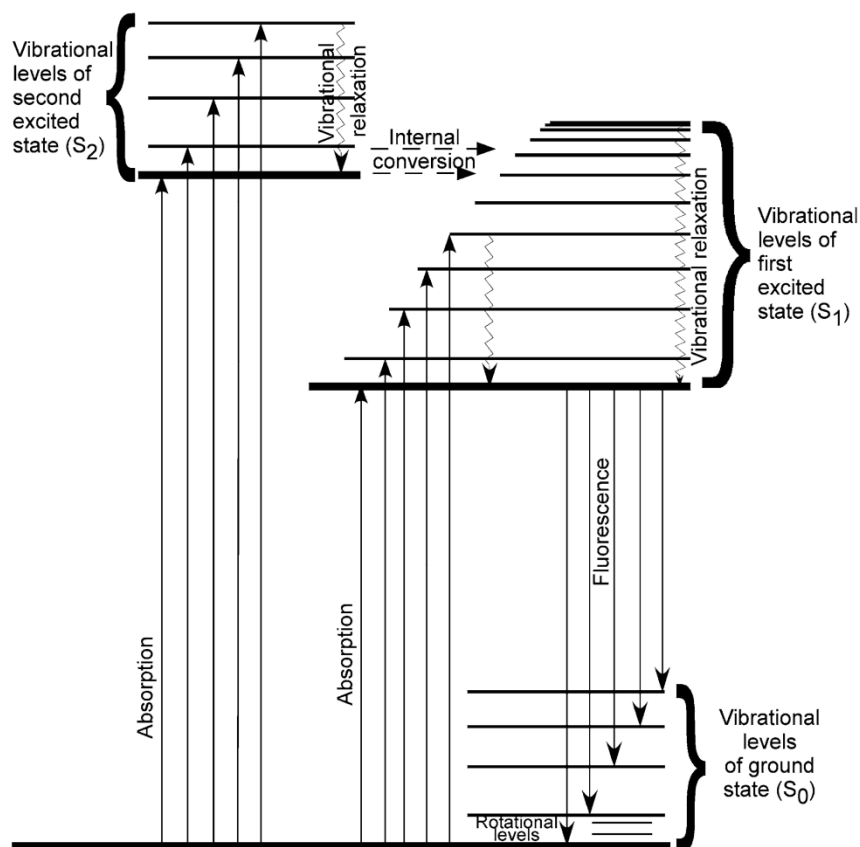


Figure 2.1: Jablonski diagram illustrating the energy level diagram for absorption and fluorescence emission.¹ Reproduced with kind permission from Springer Science+Business Media.

2.1.2 Total internal reflection fluorescence.^{2,3} Total internal reflection fluorescence, TIRF, is a technique that takes advantage of the refraction of propagating light when passing between materials of different refractive indices. Total internal reflection is observed when a collimated beam is directed toward an interface from higher to lower refractive index at an angle equal or greater than a well-defined critical angle. This angle is determined by the ratio of the two refractive indices and can be calculated by setting the angle of diffraction, θ_2 , to 90° in the Snell equation:

$$n_1 \sin \theta_1 = n_2 \sin \theta_2 \rightarrow \theta_c = \sin^{-1} \left(\frac{n_2}{n_1} \right) \quad (2.1)$$

where θ_c is the critical angle and n_1 and n_2 are the refractive indices of the two media, illustrated in Figure 2.2. At angles exceeding θ_c , the collimated light no longer passes through the interface; instead an evanescent electromagnetic wave of the same wavelength propagates into the lower index material, the intensity decaying exponentially with distance from the interface.

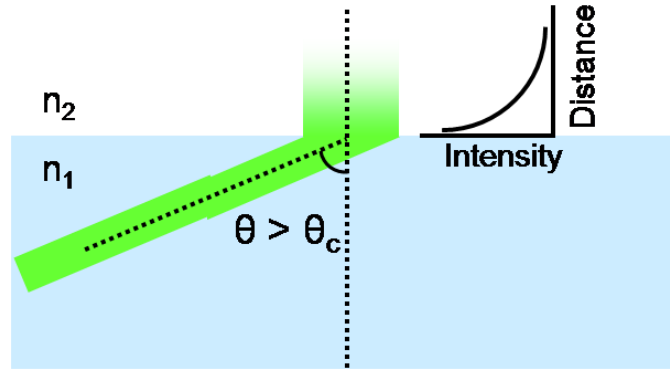


Figure 2.2: Illustration of total internal reflection fluorescence when the incoming radiation is directed to the interface between the medium with higher refractive index n_1 and lower refractive index n_2 at greater than the critical angle θ_c .

The evanescent wave can be extremely useful as a spatially limited excitation source in fluorescence experiments involving samples with objects of interest near the interface.⁴ Background levels, always a concern in fluorescence experiments, are greatly reduced in a TIRF setup as opposed to a widefield configuration in which the sample is flooded with excitation light. The intensity as a function of distance from the interface, y , for the TIRF excitation wave is determined by:

$$I(y) = I_o e^{-y/d} \quad (2.2)$$

where

$$d = \frac{\lambda(0)}{4\pi\sqrt{n_1^2 \sin^2 \theta - n_2^2}} \quad (2.3)$$

and I_o is the excitation wavelength intensity at the interface, y is distance from the interface, λ is the wavelength of the excitation light, n_1 and n_2 are the refractive indices of the two media, and θ is the angle of incidence for the excitation beam. The depth of penetration, d , is given approximately by $I(y)/I_o \sim 1/3$ and defines the extent of the excitation volume.

Irradiating the interface at an angle that exceeds the critical angle is not necessarily a trivial matter, and can be done in several geometries,⁵ so comparing the excitation angle needed to achieve TIR in a given sample and the largest angle possible with the microscope setup is a good idea. For example, the critical angle for hydrated polymer on glass samples is 69° using $n_1 = 1.5$ for glass, $n_2 = 1.4$ for water/polymer. The maximum excitation angle in total internal reflection is determined by the numerical aperture of the objective, NA, by:

$$NA = n \sin(\alpha) \quad (2.4)$$

As detailed in Section 4.1, single molecule tracking experiments were carried out on an objective based TIRF microscope with a 1.45 numerical aperture objective, which is capable of a maximum 72° from Equation 2.4 and therefore is able to achieve TIRF with this refractive index ratio. Graphical illustrations of the exponential decay and the depth of penetration relationships for this example are displayed in Figure 2.3. The blue trace is 488 nm and the green trace is 526 nm, two excitation wavelengths that were used in SMT experiments during the course of this project.

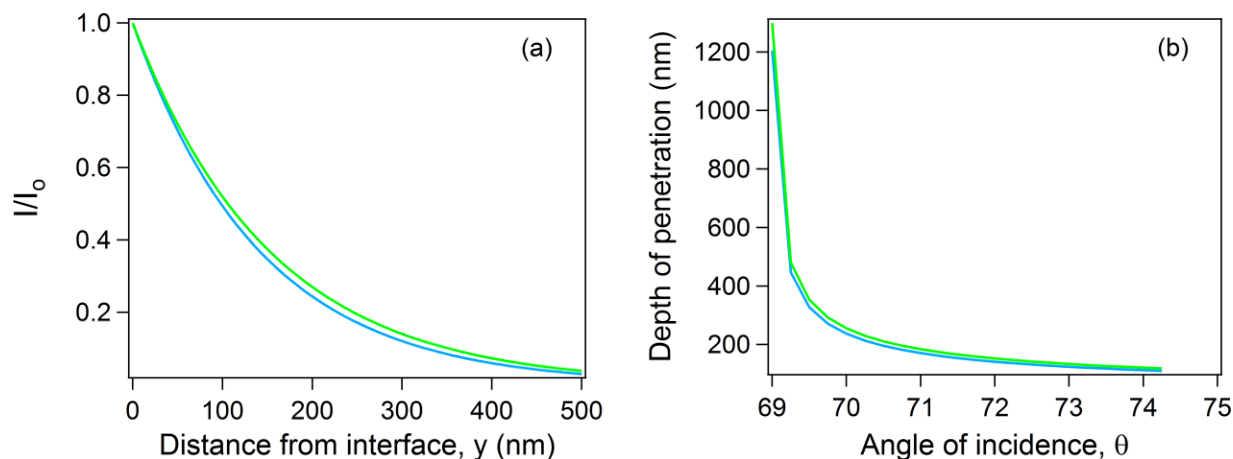


Figure 2.3: (a) The theoretical exponential decay curve for angle of incidence $\theta = 72^\circ$ for $n_1 = 1.5$ and $n_2 = 1.4$. (b) The depth of penetration versus angle of incidence of incidence. The blue trace is 488 nm and the green is 526 nm.

As described in Equations 2.2 and 2.3, the rate of the exponential decay becomes slower with increasing wavelength. Practically speaking, this means that the depth of penetration is slightly larger for 526 nm than for 488 nm. In addition, the depth of penetration decreases drastically with increasing the angle of incidence. This is referred to as a tighter evanescent wave in which the excitation is limited to a smaller volume near the interface.

2.2 Phase transition in surface tethered pNIPAAm brushes

This literature review is intended to provide a context for how the results and conclusions in Chapter 6 fit into the existing knowledge base about the LCST collapse pNIPAAm. The focus here is on reports that offer interesting insights regarding surface and bulk changes and includes discussion of the physical and chemical implications of experiments that employ synthetic methods or have sample composition similar to those used in this thesis, and show data over the

whole range of the phase transition, rather than just endpoints. More details about samples and experiments are included in the summaries when they are particularly pertinent or interesting.

As indicated by Schild, most of the early research on pNIPAAm was carried out on gels and solutions.⁶ For example, the discontinuous phase transition of pNIPAAm was first observed by Tanaka in free standing gels.⁷ The corresponding size and weight changes of millimeter scale gel plugs were measured with calipers or balances. The analytical tools applied to measuring free volume changes later became more sophisticated as dictated by the dimensions and physical form of samples.

The LCST behavior of a specific pNIPAAm sample is influenced by method of synthesis and preparation in addition to previously mentioned factors such as salt concentration, solvent, salt, surfactants, applied DC field, pH, copolymers, substrate geometry, molecular weight, and grafting density.^{8,9} Variation of polymer brush composition and degree of polymerization are used to modify surface properties, nanopattern, and design SRPs.¹⁰⁻¹⁵ Biocompatibility, corrosion resistance, and wettability can also be tailored by adjusting these factors.¹⁶⁻²¹ In the later literature there is abundant characterization of pNIPAAm in aqueous solution phase, as a gel or microgel, and adsorbed at air-water interfaces.²²⁻³⁰ More recently, the evolution from 2-dimensional to 3-dimensional structures has been intensively studied in the context of pNIPAAm on nanoparticles.^{9,31-37} However, this literature review will focus on pNIPAAm in polymer brush form, tethered covalently to substrates in densely packed conformation that causes the chains to stretch away from the surface.

Surface modification with pNIPAAm is a well researched topic with many options in terms of synthetic scheme.^{17,38} For an excellent review on the characterization of surface initiated polymer brushes, see Barbey *et al.*³⁹ Much of the existing knowledge about structure

and dynamics of pNIPAAm in this configuration has been gleaned from surface characterization techniques that allow *in situ* measurements including scanning probe microscopies, ellipsometry, electrochemistry, surface plasmon resonance, quartz crystal microbalance with dissipation monitoring, and near edge x-ray fine structure analysis.

The LCST response of pNIPAAm in solution is a sharp transition at 32°C. The corresponding response of pNIPAAm brushes (densely packed polymer covalently bound to a substrate) is broader, starts at a lower temperature, and occurs over a wider temperature range.³⁹ Raula *et al.* measured changes in the localized surface plasmon resonance of gold nanoparticles covalently coated with pNIPAAm through a controlled radical polymerization.⁴⁰ They found that the transition took place between 28°C and 38°C and was evident in the shift in the surface plasmon λ_{max} toward smaller wavelengths and a decrease in absorbance intensity at 650 nm, measured by UV-vis absorption spectroscopy, at higher temperatures, shown in Figure 2.4. These results can be explained by less hydrophilic surroundings near the surface of the Au and less shielding as the pNIPAAm collapses, respectively.

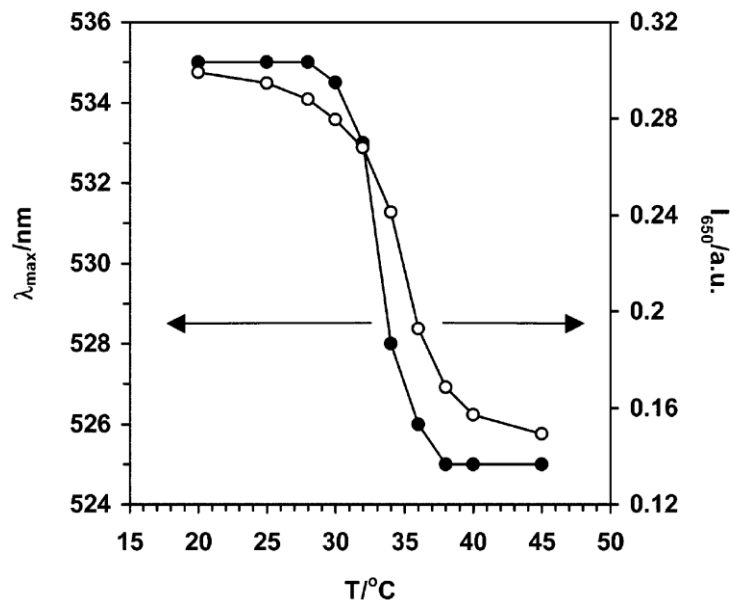


Figure 2.4: Measurements of the surface plasmon peak wavelength, λ_{\max} , and UV-vis absorbance intensity, I_{abs} , at 650 nm of the LCST behavior of aqueous pNIPAAm on Au nanoparticles.⁴⁰ Reproduced with permission of the American Chemical Society.

He *et al.* used contact angle results and atomic force microscopy (AFM) to characterize the thermosensitivity of surface initiated pNIPAAm brushes on planar gold.⁴¹ At room temperature the dry brush height was measured at 76 nm, which increased to 140 nm when hydrated at room temperature and decreased to 60 nm when the brush had collapsed at 40°C. Contact angle measurements- $62.5 \pm 2.4^\circ$ at room temperature and $\sim 90^\circ$ at 40°C- demonstrated that the surface of the pNIPAAm brush becomes less hydrophilic above the LCST, shown in Figure 2.5.

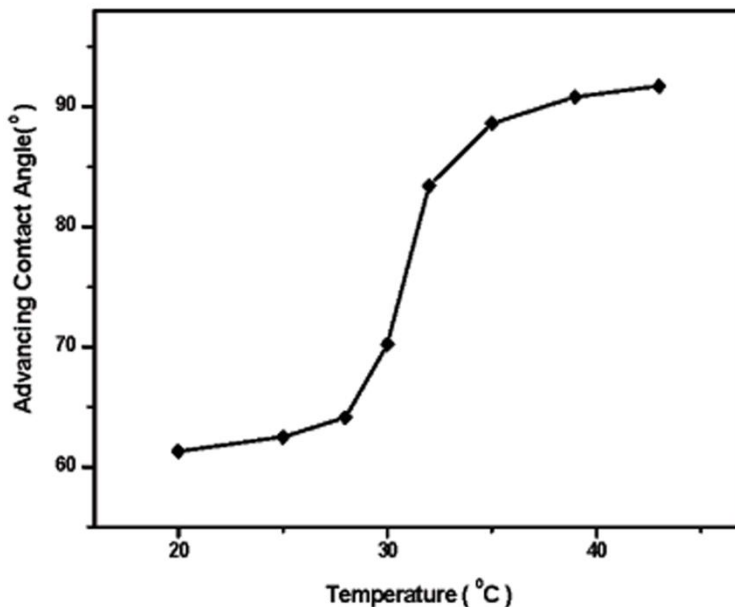


Figure 2.5: Water contact angle showing LCST behavior of surface initiated pNIPAAm on flat Au ranging between $\sim 27^{\circ}\text{C}$ to $\sim 35^{\circ}\text{C}$.⁴¹ Reproduced with permission of the American Chemical Society.

Wei *et al.* used proton nuclear magnetic resonance (NMR) and quasi-elastic light scattering (QELS) to observe the LCST behavior of pNIPAAm on gold nanorods.⁴² The authors found that the hydrogen NMR signals from pNIPAAm were strong at 20°C , weaker at 33°C , and almost gone at 40°C , see Figure 2.6. They attribute these observations to the hydrophobic shift of the pNIPAAm above the LCST, followed by the aggregation and precipitation of the brush covered Au nanorods at the highest temperature. QELS was used to verify that the nanorods were aggregating between $\sim 31^{\circ}\text{C}$ and $\sim 38^{\circ}\text{C}$, with an uncoated control sample for comparison.

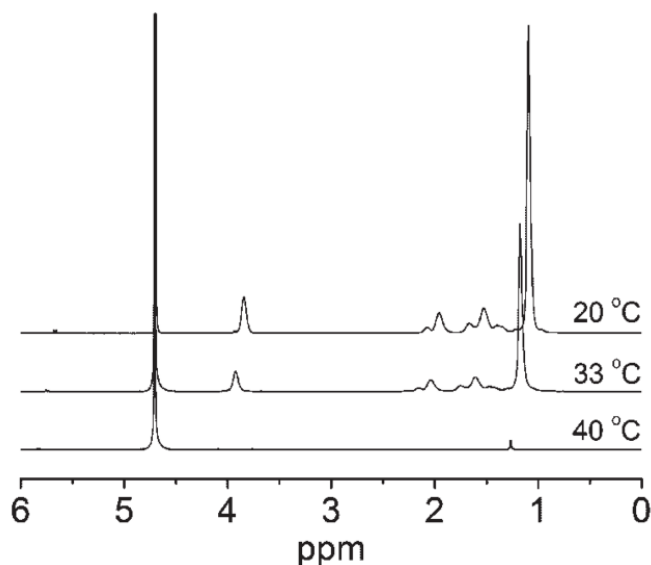


Figure 2.6: ^1H NMR spectra of pNIPAAm on Au nanorods in D_2O at 20, 33, and 40 °C.⁴²

Copyright Wiley-VCH Verlag GmbH & Co. KGaA. Reproduced with permission.

Sun *et al.* used contact angle measurements to probe the LCST behavior of surface initiated pNIPAAm grown on silicon using a controlled radical polymerization.⁴³ The authors found that between 25 °C and 40 °C, the water contact angle of a droplet on the polymer surface increased from $63.5 \pm 2.6^\circ$ to $93.2 \pm 2^\circ$, as shown in images displayed in Figure 2.7.

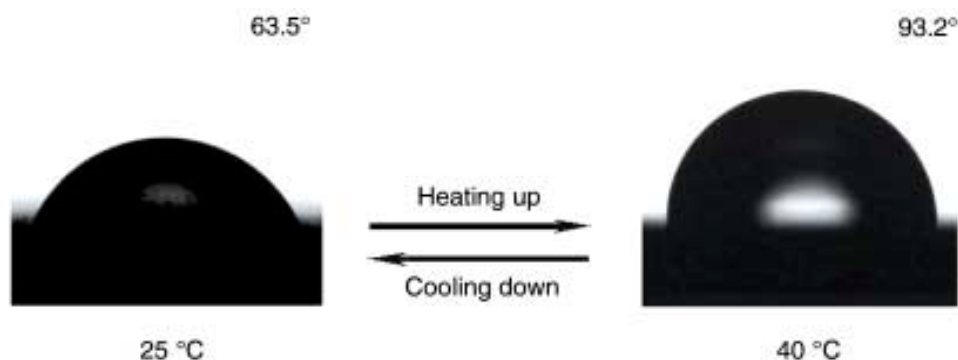


Figure 2.7: Water contact angle images for measurements on silicon tethered pNIPAAm at 25 °C and 40 °C.⁴³ Copyright Wiley-VCH Verlag GmbH & Co. KGaA. Reproduced with permission.

Laloyaux *et al.* published a well developed model for the LCST collapse of a neutral water-soluble polymer brush with support from quartz crystal microbalance measurements with dissipation monitoring (QCM-D) and equilibrium water contact angles (CA).⁴⁴ The authors found a two step transition with vertical phase separation in the collapse of surface tethered poly(di(ethyleneglycol) methyl ether methacrylate), PMEO₂MA, which shows similar LCST dependence on concentration in solution to pNIPAAm. The two phase transition in the polymer brush occurs first in the bulk over a wide temperature range, monitored by QCM-D, and then at the surface in a sharp first-order transition at the upper end of the temperature range, measured by CA. These observations are consistent with results from mean-field theory of responsive polymer brushes, showing that the collapse of a planar brush is a cooperative conformational transition, not a thermodynamic phase transition.⁴⁵ The physical significance of this statement is that the transition should be gradual regardless of the heating or cooling rate. Mean-field theory of polymer brushes predicts that the monomer unit density in a swollen brush decreases moving away from the substrate. Since the volume transition in responsive polymers is dependent on concentration, the collapse starts first in the densest region near the substrate and propagates away from the substrate as temperature is increased.

Yim *et al.* found evidence supporting this theory and advanced understanding of polymer brush conformation changes using neutron reflectometry, NR, in a series of comprehensive experiments on pNIPAAm brushes.⁴⁶⁻⁴⁸ Neutron reflectometry measures the scattering length density profile normal to the surface, which is determined by density and atomic composition. In polymer brush samples with sufficient contrast between constituents, concentration profiles of the monomer units can be obtained, contrast which was obtained in these the measurements by conducting the experiments in D₂O.

In the first paper in 2004, Yim *et al.* investigated the temperature dependent changes of a pNIPAAm brush with 21 nm dry thickness and 0.25 chains/nm² grafting density synthesized by atom transfer radical polymerization, ATRP, on gold coated silicon.⁴⁶ Reflectivity measurements were taken at 20 and 41°C, then 34, 31, 28, and 26°C, from which the volume fraction of pNIPAAm as a function of distance from the substrate and the first moment of segment volume fraction vs. temperature were calculated. The volume fraction profiles showed a discontinuous change through the transition, and the first moment of segment also showed a discontinuous change through the LCST. These results illustrate that most of collapse within the polymer brush occurred between 27 and 33°C. Along with data from a previous report,⁴⁹ these results support a concentration-dependent effective value of the Flory χ parameter for pNIPAAm in water.

Yim *et al.* also published direct evidence for a non-monotonic change in polymer conformation with temperature, a first-order vertical phase separation behavior that had been predicted by two state models.⁴⁷ As with the 2004 paper, the authors used ATRP used to synthesize pNIPAAm in a ‘grafting from’ method and carried out NR between 20°C and 41°C in D₂O. Two samples were investigated extensively, 71G exhibiting 36 nm dry thickness pNIPAAm on Au with molecular weight 71 kg/mol and surface density 0.54 chains/nm², and 209S with 57 nm dry thickness on Si with molecular weight 209 kg/mol and 0.21 chains/nm². In both samples the segment concentration profile showed a transition from single layer to bilayer back to single layer. The bilayer was observed in a narrow range in the middle of the phase transition, near the LCST. The effect was more pronounced in 209S, and was accompanied by an increase in the first moment of the profile.

These authors found that their results were consistent with predictions by Baulin and Halperin⁵⁰⁻⁵² of a critical surface density for vertical phase separation, except the increase in first moment with increasing temperature, which was not explained. They also discussed results from data not shown in this paper from three more samples of varying grafting density and molecular weight. For pNIPAAm with 44 kg/mol and 0.54 chains/nm² on Au, smaller, but still measurable, changes in profile shape and first moment through transition were observed. There was no change to a bilayer in profile shape or discontinuous change in first moment of segment volume fraction for pNIPAAm with 13 kg/mol and 0.54 chains/nm² on gold. Finally, a non-monotonic change in profile shape was not observed for pNIPAAm with 152 kg/mol and 0.063 chains/nm² on gold (a relatively high molecular weight but low grafting density). On the whole, these results point to a dependence of conformational changes on molecular weight and grafting density, which led the authors to investigate these differences more comprehensively.

Another Yim *et al.* paper, published in 2006,⁴⁸ compared samples on gold and silicon substrates with molecular weight, M , from 1 to 250 kg/mol and surface density, σ , from 0.01 to 1 chains/nm². Yim *et al.* found that polymer brushes with high molecular weight, ~150-250 kg/mol, and intermediate surface density, ~0.3 chains/nm², give the largest conformational change with temperature. They state that these results agree with recently presented numerical self-consistent theory calculation by Mendez *et al.*⁵³ However, the authors also note that the model developed by Mendez does not predict a vertical phase separation, and some qualitative differences were observed between the experimental results and the calculations.

The molecular weight and intermediate surface density ranges are explained by considering the Flory parameter $\chi(\phi)$ and chain stretching effect for densely grafted brushes in good solvent (studied in polymers with an upper critical solution temperature, which show

collapse at lower temperatures). For the highest grafting density, σ , samples, the dependence of χ on temperature is relatively low; however as σ decreases, ϕ within the brush decreases, the solvent quality at 20°C increases, and the difference in χ at 20 and 40°C increases. This results in large changes in conformation at high M . The chain stretching effect is determined by $\Sigma = \sigma\pi R_g^2$, where σ is the surface grafting density and R_g is the radius of gyration. Following the expression, Σ increases with increasing σ . Therefore, the large volume change at intermediate σ is due to the competition between the chain stretching effect and the weak effect of χ for high σ . For low σ , the polymer chains exhibit high segmental adsorption (e.g. exhibit a collapsed state closer to mushroom than brush configuration), and the volume shift with temperature for these samples is low or non-existent.

Jones *et al.* performed AFM experiments at temperatures above and below the LCST, showing changes in topography, morphology, stiffness, and adhesion.⁵⁴ Montagne *et al.* used dynamic AFM techniques that go much further than simply determining thickness and roughness of the polymer layer. The authors synthesized samples using ‘grafting under melt’ of amine-terminated pNIPAAm chains onto a gold surface with a reactive thiol self assembled monolayer, SAM, and showed that the LCST response of the resulting brush was preserved using a dynamic amplitude modulation mode AFM technique.⁵⁵ This is significant because the method used, which controls grafting density, molecule weight, and microstructure, has been shown to influence the properties of the brush. The authors demonstrated gradual conformation change from brush to mushroom at the macromolecular level. The samples were prepared by spincoating followed by annealing under conditions at $T > T_g$, resulting in a sample with 25 nm theoretical swollen thickness, $M = 41$ kg/mol and $\sigma = 0.18$ chains/nm². Impressively, the surface

densities obtained from a ‘grafting to’ method are comparable to those obtained by Yim *et al.*⁴⁸ using a ‘grafting from’ synthetic scheme.

Preliminary *in situ* tapping mode AFM images show decreased domain sizes at $T > T_{LCST}$ (0.1-0.5 μm at $T = 24.7^\circ\text{C}$ and 0.01-0.05 μm at $T = 40.4^\circ\text{C}$). Montagne *et al.* then used several dynamic AFM measurements, also *in situ*, to characterize the pNIPAAm conformation change. First, amplitude and phase approach curves were recorded as a function of probe indentation at $T = 23.2^\circ\text{C}$ and $T = 40.4^\circ\text{C}$. Three regimes were identified in these curves: domain I is a zone a non-interaction between the probe and the surface, domain II is a zone a gradual decrease in the amplitude and increase of repulsive interaction in the phase, and domain III is a zone of abrupt decrease in amplitude and strong repulsion in phase. The largest differences between low and high temperature can be observed in domain II. Interestingly, the onset of domain II at $T = 23.2^\circ\text{C}$ is at ~ 80 nm while for $T = 40.4^\circ\text{C}$ the transition into domain II is ~ 7 nm, near the dry brush thickness as determined by ellipsometry. These findings are similar to those of previous reports by Ishida⁵⁶ and Kidoaki,^{57,58} both of which found a repulsive thickness much greater than the swollen thickness of pNIPAAm.

The authors carried out a second dynamic AFM measurement by investigating the dependence of the damping factor of oscillation on the probe indentation. Similarly to the first indentation curves, these traces showed domains I, II, and III with no interaction, a smooth increase, and a sharp increase, respectively. The authors attributed an increase in the damping factor to a response to local variation in viscosity. They interpreted the smooth increase in domain II as dissipation processes to the motion of segment chains smaller than the entanglement length. Finally, Montagne *et al.* asserted that the abrupt increase in domain III is due to displacement of segment chains with sizes smaller than the dimension of the probe tip (> 10 nm).

These results show a gradual transition from brush to mushroom configuration with increasing temperature between 23 and 35°C.

Kurz *et al.* employed *in situ* broadband sum-frequency generation spectroscopy to characterize the temperature response in spin-coated pNIPAAm films immobilized on gold films.⁵⁹ By tracking the intensity of the characteristic CH₃ vibrations, the authors found a gradual reorientation of the isopropyl groups leading up to the LCST followed by an instantaneous reorientation of the methyl groups nearest to the polymer-water interface at 32°C.

Plunkett *et al.* carried out water contact angle measurements, surface plasmon, and surface forces experiments to characterize atom transfer radical polymerization (ATRP) surface initiated pNIPAAm.⁶⁰ The authors found the largest decrease in film thickness above the LCST with surface densities and molecular weights similar to those found by Yim *et al.*⁴⁸

Like Montagne *et al.*,⁵⁵ Popa *et al.*⁶¹ used a grafting-to in melt polymerization with carboxyl terminated pNIPAAm to obtain samples. The authors utilized *in situ* AFM and IR to probe the physical and molecular temperature response. They observed morphology changes and switches in the hydrogen bonding. Shan *et al.*⁶² observed a two phase transition in pNIPAAm on Au nanoparticles using microcalorimetric measurements and proposed a two stage collapse consisting first of the dense inner layer and then loosely packed outer layer like that found by Yim *et al.* Turan *et al.*⁶³ also saw a two phase transition when they used *in situ* infrared spectroscopy, AFM, and ellipsometry to characterize pNIPAAm on Si prepared by ATRP. Wu *et al.*³⁶ grew pNIPAAm brushes in silica nanoparticles through ATRP and probed the LCST response by measuring the hydrodynamic radius and radius of gyration of the particles with laser light scattering and found a two phase transition. Wang *et al.*⁶⁴ observed molecular probes in pNIPAAm grown on silica through ATRP with fluorescence correlation spectroscopy. They

interpreted their results in terms of probes diffusing at the pNIPAAm-water interface, not within the polymer, and find that as the polymer passes through the LCST, the friction coefficient at the surface increases and diffusion of the molecular probes slows down.

In summary, the results discussed here form the basis for the body of knowledge pertaining to the temperature response of surface tethered pNIPAAm. Surface plasmon resonance and UV-vis absorption spectroscopy illustrated the gradual transition for densely packed pNIPAAm brushes over a broad temperature range, $\sim 27\text{-}36^\circ\text{C}$. This characteristic transition was confirmed with contact angle, CA, measurements and AFM thickness data, which also showed $\sim 2\times$ decrease thickness in the collapsed compared to expanded state. Temperature variable ^1H NMR spectroscopy revealed a decrease in signal from the amide and isopropyl groups in pNIPAAm, most drastic at $T > 33^\circ$, due to the hydrophobic shift in the polymer. Neutron reflectometry experiments, coupled with theoretical predictions of the LCST collapse in neutral water soluble polymers, showed that collapse of most of the brush occurs between 27 and 33°C , followed by collapse of the untethered polymer ends. Additional NR experiments found that this two-phase collapse was dependent on grafting density and molecular weight and that the largest conformational changes were observed in polymer brushes with high MW and intermediate surface density, which was later confirmed by microcalorimetry; IR, AFM, and ellipsometry; hydrodynamic radius and radius of gyration measurements; and by CA, SPR, and SFA experiments. Dynamic AFM measurements re-illustrated the collapse of the brush over a broad temperature range and discovered that the repulsive thickness much greater than the swollen thickness of the brush. SFG showed a gradual reorientation of the isopropyl groups within the polymer region, followed by an instantaneous switch at the polymer-water interface, which is in agreement with previous results showing a gradual collapse of the bulk and

subsequent collapse at the outermost region. Initial results from FCS showed evidence of decreasing rates in diffusion of molecular probes when the polymer passes through the LCST.

Taking into account the breadth of knowledge gained from studies focused on surface tethered pNIPAAm, several conclusions can be drawn. The two phase collapse in pNIPAAm and the broad, gradual overall transition have been well established by the large amount of evidence from a wide range of disparate techniques. In addition, the effects of molecular weight and surface density on this collapse have been determined. A shift in domain sizes by a 10X decrease from the expanded state to the collapsed state has been introduced. It is our intention that results from SMT experiments will elucidate domain changes further by detailing the shift in molecular probe exploration of free volume within pNIPAAm brushes. These new insights will come in the form of amount of space explored in zones of relative confinement and time spent in confined states, with sub-micron and millisecond resolution, respectively. In the future, SMT analysis may be used further to create dynamic maps of confinement areas and to calculate energy barriers to diffusion.

2.3 References

- (1) Noomnarm, U.; Clegg, R. M. *Photosynth. Res.* **2009**, *101*, 181-194.
- (2) Ross, S. T.; Schwartz, S.; Fellers, T. J.; Davidson, M. W. "Nikon Microscopy U, TIRF tutorial." *Nikon*. Nov. 28, 2010. Web. 2000-2010.
- (3) Paige, M. F.; Bjerneld, E. J.; Moerner, W. E. *Single Mol.* **2001**, *2*, 191-201.
- (4) Axelrod, D. *Traffic* **2001**, *2*, 764-774.
- (5) Conibear, P. B.; Bagshaw, C. R. *J Microsc-Oxford* **2000**, *200*, 218-229.
- (6) Schild, H. G. *Prog. Polym. Sci.* **1992**, *17*, 163-249.

- (7) Hirokawa, Y.; Tanaka, T. *J. Chem. Phys.* **1984**, *81*, 6379-6380.
- (8) Jhon, Y. K.; Bhat, R. R.; Jeong, C.; Rojas, O. J.; Szleifer, I.; Genzer, J. *Macromol. Rapid Commun.* **2006**, *27*, 697-701.
- (9) Stuart, M. A. C.; Huck, W. T. S.; Genzer, J.; Muller, M.; Ober, C.; Stamm, M.; Sukhorukov, G. B.; Szleifer, I.; Tsukruk, V. V.; Urban, M.; Winnik, F.; Zauscher, S.; Luzinov, I.; Minko, S. *Nat. Mater.* **2010**, *9*, 101-113.
- (10) Husseman, M.; Malmstrom, E. E.; McNamara, M.; Mate, M.; Mecerreyes, D.; Benoit, D. G.; Hedrick, J. L.; Mansky, P.; Huang, E.; Russell, T. P.; Hawker, C. J. *Macromolecules* **1999**, *32*, 1424-1431.
- (11) Matyjaszewski, K.; Miller, P. J.; Pyun, J.; Kickelbick, G.; Diamanti, S. *Macromolecules* **1999**, *32*, 6526-6535.
- (12) Zhao, B.; Brittain, W. J.; Zhou, W. S.; Cheng, S. Z. D. *J. Am. Chem. Soc.* **2000**, *122*, 2407-2408.
- (13) Zhao, B. *Polymer* **2003**, *44*, 4079-4083.
- (14) von Werne, T. A.; Germack, D. S.; Hagberg, E. C.; Sheares, V. V.; Hawker, C. J.; Carter, K. R. *J. Am. Chem. Soc.* **2003**, *125*, 3831-3838.
- (15) Kong, X. X.; Kawai, T.; Abe, J.; Iyoda, T. *Macromolecules* **2001**, *34*, 1837-1844.
- (16) Edmondson, S.; Osborne, V. L.; Huck, W. T. S. *Chem. Soc. Rev.* **2004**, *33*, 14-22.
- (17) *Polymer brushes: synthesis, characterization, and applications*; Advincula, R. C.; Brittain, W. J.; Caster, K. C.; Ruhe, J., Eds., 2004.
- (18) Matyjaszewski, K.; Miller, P. J.; Shukla, N.; Immaraporn, B.; Gelman, A.; Luokala, B. B.; Siclovan, T. M.; Kickelbick, G.; Vallant, T.; Hoffmann, H.; Pakula, T. *Macromolecules* **1999**, *32*, 8716-8724.

- (19) Zhao, B.; Brittain, W. J. *Prog. Polym. Sci.* **2000**, *25*, 677-710.
- (20) Zhulina, E. B.; Singh, C.; Balazs, A. C. *Macromolecules* **1996**, *29*, 6338-6348.
- (21) Wu, T.; Efimenko, K.; Vlcek, P.; Subr, V.; Genzer, J. *Macromolecules* **2003**, *36*, 2448-2453.
- (22) Lee, L. T.; Jean, B.; Menelle, A. *Langmuir* **1999**, *15*, 3267-3272.
- (23) Jean, B.; Lee, L. T.; Cabane, B. *Langmuir* **1999**, *15*, 7585-7590.
- (24) Richardson, R. M.; Pelton, R.; Cosgrove, T.; Zhang, J. *Macromolecules* **2000**, *33*, 6269-6274.
- (25) Huang, Q. R.; Wang, C. H. *Langmuir* **1999**, *15*, 634-637.
- (26) Zhang, J.; Pelton, R. *Langmuir* **1999**, *15*, 5662-5669.
- (27) Zhang, J.; Pelton, R. *Langmuir* **1996**, *12*, 2611-2612.
- (28) Noskov, B. A.; Akentiev, A. V.; Bilibin, A. Y.; Grigoriev, D. O.; Loglio, G.; Zorin, I. M.; Miller, R. *Langmuir* **2004**, *20*, 9669-9676.
- (29) Della Volpe, C.; Cassinelli, C.; Morra, M. *Langmuir* **1998**, *14*, 4650-4656.
- (30) Kawaguchi, M.; Hirose, Y.; Kato, T. *Langmuir* **1996**, *12*, 3523-3526.
- (31) Radhakrishnan, B.; Constable, A. N.; Brittain, W. J. *Macromol. Rapid Commun.* **2008**, *29*, 1828-1833.
- (32) Boue, F.; Cousin, F.; Gummel, J.; Oberdisse, J.; Carrot, G.; El Harrak, A. *C. R. Physique* **2007**, *8*, 821-844.
- (33) Carrot, G.; Gal, F.; Cremona, C.; Vinas, J.; Perez, H. *Langmuir* **2009**, *25*, 471-478.
- (34) El Harrak, A.; Carrot, G.; Oberdisse, J.; Jestin, J.; Boue, F. *Polymer* **2005**, *46*, 1095-1104.
- (35) Oberdisse, J. *Curr. Opin. Colloid Interface Sci.* **2007**, *12*, 3-8.
- (36) Wu, T.; Zhang, Y. F.; Wang, X. F.; Liu, S. Y. *Chem. Mat.* **2008**, *20*, 101-109.

- (37) Zou, H.; Wu, S. S.; Shen, J. *Chem. Rev.* **2008**, *108*, 3893-3957.
- (38) Pyun, J.; Kowalewski, T.; Matyjaszewski, K. *Macromol. Rapid Commun.* **2003**, *24*, 1043-1059.
- (39) Barbey, R.; Lavanant, L.; Paripovic, D.; Schuwer, N.; Sugnaux, C.; Tugulu, S.; Klok, H. A. *Chem. Rev.* **2009**, *109*, 5437-5527.
- (40) Raula, J.; Shan, J.; Nuopponen, M.; Niskanen, A.; Jiang, H.; Kauppinen, E. I.; Tenhu, H. *Langmuir* **2003**, *19*, 3499-3504.
- (41) He, Q.; Kuller, A.; Grunze, M.; Li, J. B. *Langmuir* **2007**, *23*, 3981-3987.
- (42) Wei, Q. S.; Ji, J.; Shen, J. C. *Macromol. Rapid Commun.* **2008**, *29*, 645-650.
- (43) Sun, T. L.; Wang, G. J.; Feng, L.; Liu, B. Q.; Ma, Y. M.; Jiang, L.; Zhu, D. B. *Angew. Chem. Int. Edit.* **2004**, *43*, 357-360.
- (44) Laloyaux, X.; Mathy, B.; Nysten, B.; Jonas, A. M. *Langmuir*, *26*, 838-847.
- (45) Zhulina, E. B.; Borisov, O. V.; Pryamitsyn, V. A.; Birshstein, T. M. *Macromolecules* **1991**, *24*, 140-149.
- (46) Yim, H.; Kent, M. S.; Mendez, S.; Balamurugan, S. S.; Balamurugan, S.; Lopez, G. P.; Satija, S. *Macromolecules* **2004**, *37*, 1994-1997.
- (47) Yim, H.; Kent, M. S.; Satija, S.; Mendez, S.; Balamurugan, S. S.; Balamurugan, S.; Lopez, G. P. *Phys. Rev. E* **2005**, *72*, 051801.
- (48) Yim, H.; Kent, M. S.; Mendez, S.; Lopez, G. P.; Satija, S.; Seo, Y. *Macromolecules* **2006**, *39*, 3420-3426.
- (49) Yim, H.; Kent, M. S.; Huber, D. L.; Satija, S.; Majewski, J.; Smith, G. S. *Macromolecules* **2003**, *36*, 5244-5251.
- (50) Baulin, V. A.; Zhulina, E. B.; Halperin, A. J. *Chem. Phys.* **2003**, *119*, 10977-10988.

- (51) Baulin, V. A.; Halperin, A. *Macromol. Theory Simul.* **2003**, *12*, 549-559.
- (52) Baulin, V. A.; Halperin, A. *Macromolecules* **2002**, *35*, 6432-6438.
- (53) Mendez, S.; Curro, J. G.; McCoy, J. D.; Lopez, G. P. *Macromolecules* **2005**, *38*, 174-181.
- (54) Jones, D. M.; Smith, J. R.; Huck, W. T. S.; Alexander, C. *Adv. Mater.* **2002**, *14*, 1130-1134.
- (55) Montagne, F.; Polesel-Maris, J.; Pugin, R.; Heinzelmann, H. *Langmuir* **2009**, *25*, 983-991.
- (56) Ishida, N.; Biggs, S. *Langmuir* **2007**, *23*, 11083-11088.
- (57) Ohya, S.; Kidoaki, S.; Matsuda, T. *Biomaterials* **2005**, *26*, 3105-3111.
- (58) Kidoaki, S.; Ohya, S.; Nakayama, Y.; Matsuda, T. *Langmuir* **2001**, *17*, 2402-2407.
- (59) Kurz, V.; Grunze, M.; Koelsch, P. *Chemphyschem* **2010**, *11*, 1425-1429.
- (60) Plunkett, K. N.; Zhu, X.; Moore, J. S.; Leckband, D. E. *Langmuir* **2006**, *22*, 4259-4266.
- (61) Popa, A. M.; Angeloni, S.; Burgi, T.; Hubbell, J. A.; Heinzelmann, H.; Pugin, R. *Langmuir* **2010**, *26*, 15356-15365.
- (62) Shan, J.; Chen, J.; Nuopponen, M.; Tenhu, H. *Langmuir* **2004**, *20*, 4671-4676.
- (63) Turan, E.; Demirci, S.; Caykara, T. *Thin Solid Films* **2010**, *518*, 5950-5954.
- (64) Wang, S. Q.; Zhu, Y. X. *Soft Matter* **2010**, *6*, 4661-4665.

CHAPTER 3

SURFACE TETHERED PNIPAAm BRUSHES: PREPARATION AND CHARACTERIZATION

3.1 Sample preparation

3.1.1 Atom transfer radical polymerization. Atom transfer radical polymerization, ATRP, is a ‘living’ reaction that has the advantages of minimal crosslinking between chains, uniform molecular weight, controllable film thickness, and low solution polymerization.¹⁻⁴ Surface initiated ATRP is particularly desirable for generating high density polymer brushes with reproducible structure that are covalently bound to the substrate using a grafting-from surface polymerization strategy.⁵ These characteristics were the impetus for choosing this polymerization method for this project. ATRP involves a copper-ligand catalyst that facilitates addition across the double bond in the monomer to an α -halide terminated initiator or strand. The reaction is carried out in an oxygen free environment using an inert atmosphere box or Schlenk techniques. Compared to other methods, ATRP is a simple reaction with good reproducibility due to the absence of external factors such as UV light, γ -ray, thermal energy, and the deoxygenating requirements are not as strict as for other techniques such as plasma-induced grafting.⁶ Synthesis and characterization of pNIPAAm samples were carried out in this project as follows.

3.1.1 Materials. Unless otherwise noted reagents and solvents were obtained from Sigma Aldrich. 11-trichlorosilylundecyl-2'-bromo-2-isobutyrate (silane initiator) (95+%, ATRP Solutions), hexanes (ACS reagent, 99.9%, Fisher), dichloromethane (DCM, Chromasol Plus),

ethanol (EtOH, denatured for HPLC, Acros), isopropanol (IPA, ACS reagent, >99.5%), cuprous bromide (CuBr, 99.999%), ethanol (EtOH, 99%, Fisher), toluene (ACS spectrophotometric), acetone (Lab reagent, $\geq 99.5\%$), hydrogen peroxide (H_2O_2 , 30%, Certified ACS, Fisher Chemical), and sulfuric acid (H_2SO_4 , 95-98%, c.p., Acros Chemicals) were used as received. N-isopropylacrylamide (NIPAAm, 97%) was purified by running a 1:1 hexanes/DCM saturated solution through a 2.5 cm basic alumina column, removing the solvent by reduced pressure evaporation, recrystallizing the remaining solid in hot hexanes at $< 50^\circ\text{C}$, rinsing with minimal ice cold hexanes, and removing the solvent by reduced pressure evaporation. Methanol (MeOH, ACS reagent, 99.9%, Fisher), pentamethyldiethylenetriamine (PMDETA, 99%), deionized (DI) water ($\rho = 18 \text{ M}\Omega \text{ cm}$, Millipore Corp.) in Schlenk flasks and toluene (anhydrous, 99.8%) and triethylamine (TEA, $\geq 99.5\%$) in SureSeal bottles were degassed by bubbling nitrogen for 5-10 minutes and then were immediately transferred into a controlled atmosphere box. Chemical structures of the initiator and the monomer are displayed in Figure 3.1.

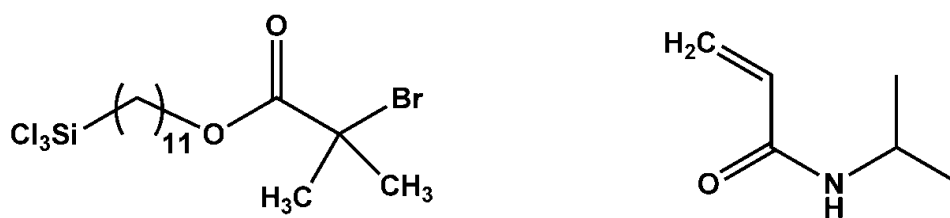


Figure 3.1: Chemical structure of 11-(2-bromo-2-methylpropionyloxyundecenyl)trichlorosilane (left), the ATRP initiator, and N-isopropylacrylamide (right), the monomer.

3.1.2 Synthesis. pNIPAAm brushes 30-100 nm thick dry, ~60-200 nm thick hydrated were prepared by a method described previously^{7,8} and the synthetic scheme is outlined in Figure 3.2. Borosilicate glass coverslips (No. 1.5, Gold Seal, Electron Microscopy Sciences) were prepared

by rinsing with DI water and then IPA, drying with a nitrogen stream, and either (1) exposing to argon plasma for 10 min, to strip away the outer layer and any surface contamination, or (2) cleaning any organic contamination in a 1:3 $\text{H}_2\text{O}_2/\text{H}_2\text{SO}_4$ piranha solution. A silane monolayer of 11-trichlorosilylundecyl-2'-bromo-2-isobutyrate for ATRP initiation was deposited onto a coverslip in a nitrogen glovebox to control the amount of water in the reaction solution.

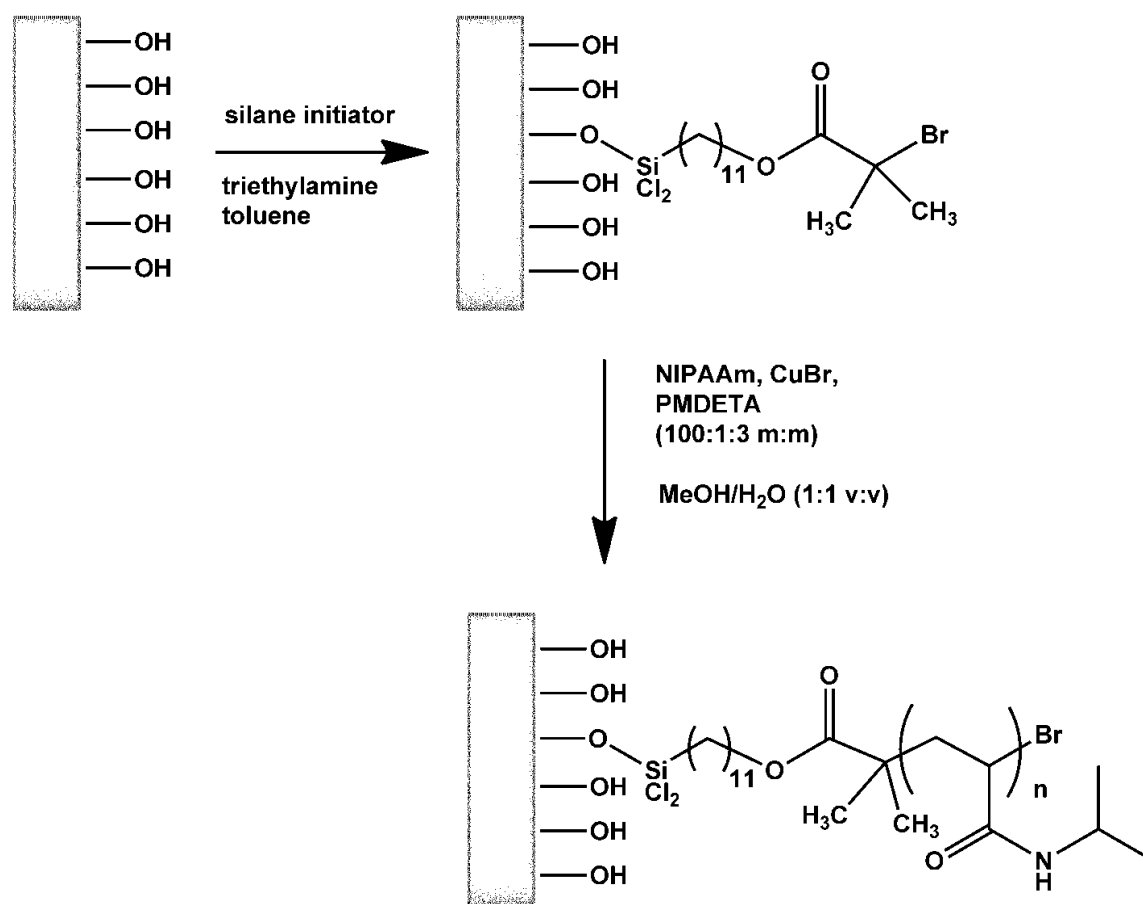


Figure 3.2: Synthetic scheme for unpatterned pNIPAAm on silicon and silica. In the first step, the silane initiator forms an α -bromide terminated monolayer on the hydride terminated substrate. In the second step, pNIPAAm is ‘grafted from’ the substrate as the monomer is added to growing chains across the $\text{C}=\text{C}$ bond in the presence of a Cu(I) -PMDETA complex in a methanol-water solution.

Following published procedures,⁹ the coverslips were immersed in a silanization solution that consisted of 20 mL anhydrous toluene, 150 μ L TEA, and 30 μ L silane for 15 min. In order to obtain samples with silane on a single side, several drops of the toluene-TEA-silane solution was carefully placed on each coverslip so that it just covered the surface. The coverslips were allowed to react in a closed container with excess toluene in order to reduce evaporation of the silane solution. After the reaction period was completed, the coverslips were removed from the controlled atmosphere box, sonicated in fresh non-anhydrous toluene for 5 min, rinsed with acetone and methanol, and dried with a nitrogen stream. A silicon wafer sample was used to check the silane layer thickness for consistency across the sample with ellipsometry and to confirm that 15 minutes was sufficient reaction time. After silanizing each coverslip, the initiated sample was transferred back into the nitrogen controlled atmosphere box for polymerization.

ATRP was subsequently carried out by immersing the initiated sample in the reaction solution at 298K in an oxygen-free atmosphere for 1 hour. The reaction mixture consisted of NIPAAm (3.15 g, 27.5 mmol), CuBr (40.0 mg, 0.278 mmol) and PMDETA (175 μ L, 0.835mmol) in 30 mL of 1:1 v:v MeOH:water. A stock solution of CuBr and PMDETA in MeOH was prepared using an entire 1 g ampoule of CuBr in order to reduce measurement errors due to static and difficulty in massing small amounts of CuBr. In mixing the reactants, a small amount of MeOH and then the PMDETA were added to the CuBr. When an ATRP reaction mixture was needed, the desired volume of CuBr stock solution was measured with a syringe. In a separate container, the remaining MeOH and then the water were added to the NIPAAm. After all solids dissolved, the two mixtures were added to each other, resulting in a pale green solution, into which the initiated samples were then placed. After the desired reaction time, the samples

were removed from the reaction mixture, transferred out of the controlled atmosphere box, rinsed with methanol, and dried with a nitrogen stream. During preliminary experiments atomic force microscopy (Asylum Research MFP-3D), x-ray photoelectron spectroscopy (Kratos Axis ULTRA), single wavelength ellipsometry (Gaertner L116C), and infrared spectroscopy (Nicolet Nexus 670 FT) were used to verify the formation of the initiator and the polymer layers (data not shown). In subsequent preparations, thickness was checked with profilometry (Sloan Dektak³ ST) and/or ellipsometry.

3.2 Sample characterization

3.2.1 Characterization with infrared and x-ray photoelectron spectroscopies. The external reflection infrared spectroscopy, x-ray photoelectron spectroscopy characterization were carried out by Ishika Lokuge during his PhD work in the Bohn group.¹⁰ IR absorption spectra of pNIPAAm were obtained on Au coated porous nanocapillary array membranes and XPS spectra were acquired from pNIPAAm grown on Au coated silicon substrates. IR spectra showed peaks at 1653, 1558, and 1540 cm^{-1} for amide carbonyl absorption, N-H bending, and C-H bending, respectively. Peaks appear at 1387 and 1364 cm^{-1} from the C-(CH₃)₂ isopropyl group and 2900-2800 cm^{-1} for CH₂ asymmetric and symmetric stretching vibrations. XPS spectra show a C_{1s} peak that was fitted to the four distinct types of C atom in pNIPAAm – a peak at 287.5 eV for the sp² hybridized C and at 284.5, 285, and 286 eV for the three types of sp³ hybridized C. A peak appears at 399 eV for the N_{1s} of the amide.

3.2.2 Thickness and homogeneity measurements with atomic force microscopy. Patterned pNIPAAm samples were made for atomic force microscopy, AFM, experiments by using

microcontact printing to apply silane initiator to select areas of the substrate after which polymer would grow only in the initiated spots. This scheme was useful in judging the efficacy of the initiation and polymerization reactions, and in measuring the height difference between polymer brush and substrate. The pattern is evident in the height scan displayed in Figure 3.3 where raised polymer brush is represented by yellow compared to the substrate which is red, with a 63 nm height difference.

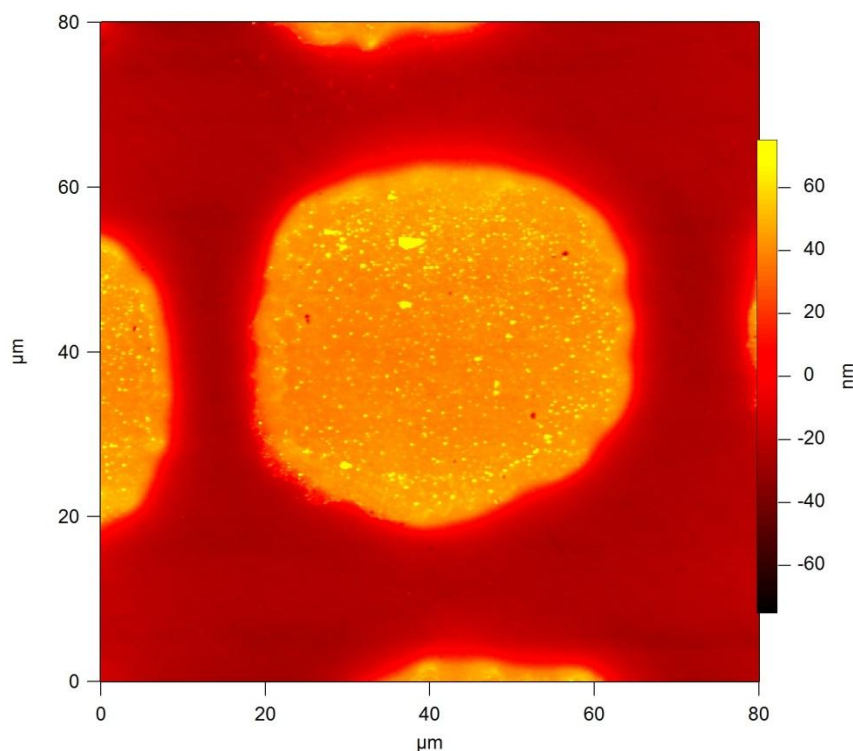


Figure 3.3: Contact mode atomic force microscopy height image of unhydrated patterned pNIPAAm on silica consisting of 40 x 40μm squares. Height of brush was measured at 63 nm, collection parameters were 1.000 V set point, 5.00 V gain, 0.40 Hz.

AFM experiments were also carried on unpatterned pNIPAAm samples on silicon in order to judge the homogeneity of the polymer layer. The polymer layer height image in Figure 3.4 shows no bare spots on a 500 nm scale, and height range of 5-6 nm.

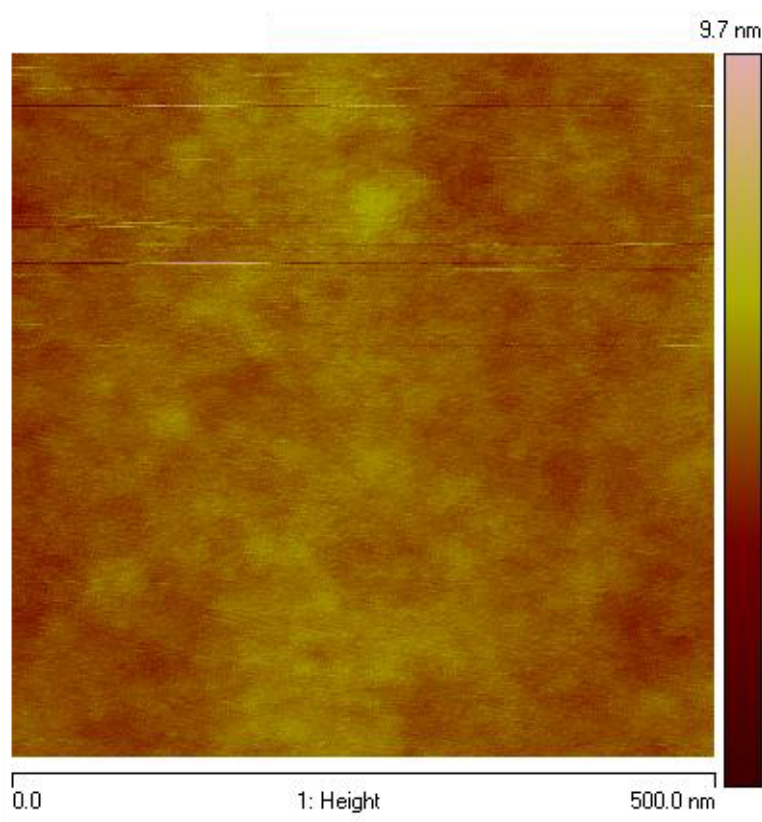


Figure 3.4: Atomic force microscopy height scan of an unpatterned, unhydrated 30 nm thick pNIPAAm sample on silicon, image aspect ratio is 1. Collection parameters were 0.599 Hz, Gain 1.00, measurements taken in collaboration with Susan Fullerton, Univ. of Notre Dame.

3.3 Reaction time calibration

Two sets of trials were carried out in order to verify and calibrate reaction times. First the silanization reaction time was examined with constant polymerization time. After initiation times were established, the thickness as a function of polymerization time was determined.

The silanization trials were carried out because the original reaction from Bao *et al.*⁹ purported to use a 48 hour reaction time, which seemed unnecessary for monolayer formation and unreasonable for our reaction, especially when making single sided samples. Figure 3.5 shows the results from ellipsometry on ten separate samples that were treated with silane initiator for 15 min to 72 hours, followed by a 1 hour ATRP reaction. Each sample was measured in at least 4 spots to arrive at a mean and standard deviation.

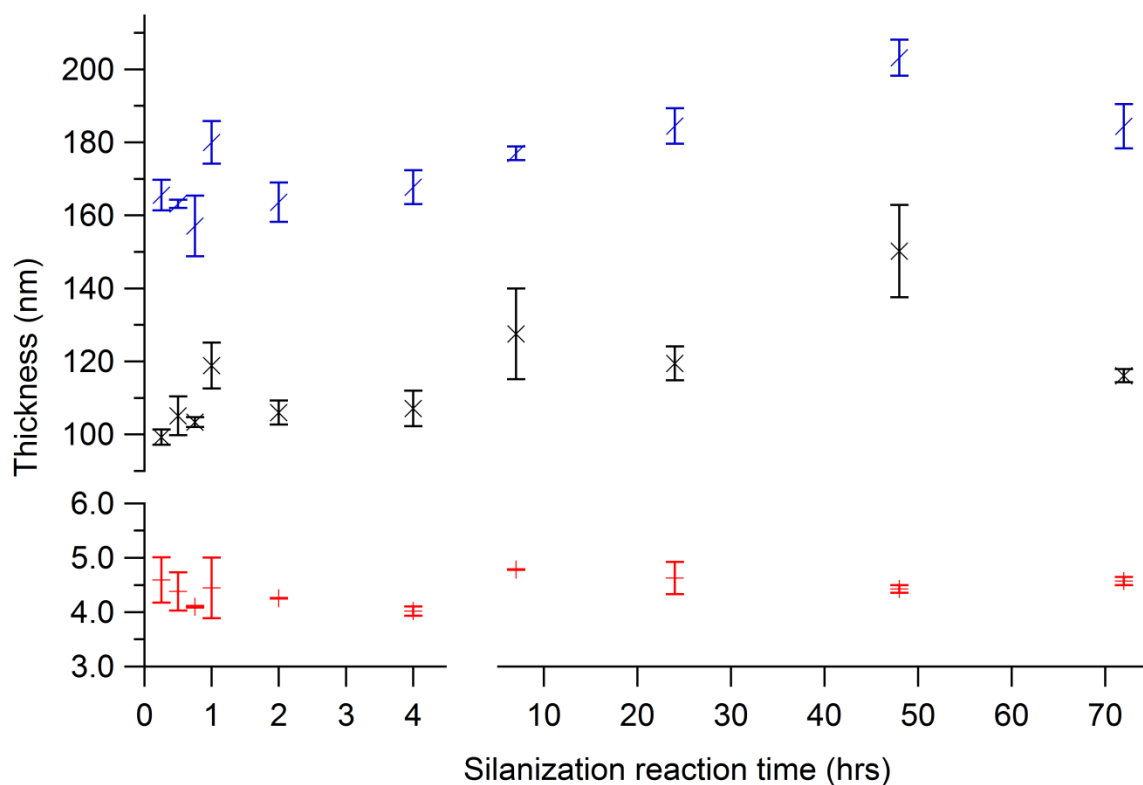


Figure 3.5: Ellipsometry measurements of silane thickness (red +), unhydrated pNIPAAm (black x), and hydrated pNIPAAm (blue /) on silicon from silanization time trials, all with 1 hr ATRP reaction time. Mean and standard deviations are displayed from at least 4 measurements at each reaction time. Note the break in reaction time on the abscissa.

Looking at mean thickness of the silane and polymer layers, there is no apparent trend in silanization time vs. thickness. There is also no correlation between standard deviation of the silane layer (red —) and that of unhydrated (black x) and hydrated (blue /) polymer layer; small silane standard deviation is equally likely to result in relatively large and small standard deviations in pNIPAAm thickness. From this trial, a silanization time of 15 minutes was determined to be sufficient for monolayer formation and longer reaction times were also deemed acceptable, but unnecessary. Also, if the standard deviation of a silane layer is 1 nm or less, the monolayer is of sufficiently high quality to grow a polymer layer that exhibits have a standard deviation ≤ 10 nm.

The second set of trials was carried out on samples with ATRP polymerization times between 1 and 60 minutes. Since synthetic methods were refined through the course of the project, not all characterization is on the same type of sample (silanizations were carried out for different amounts of time, for example). For the purposes of this calibration, especially with the conclusions from the silanization trial, the samples are sufficiently similar to compare. All the results from profilometry measurements on unhydrated pNIPAAm (green +) and ellipsometry measurements on unhydrated (black x) and hydrated (blue /) pNIPAAm are displayed in Figure 3.6. The unhydrated measurements from profilometry and ellipsometry carried out on separate samples are in good agreement. This lends credibility to the measurements since probe based techniques contact the sample and tend to under-measure the thickness of soft materials.

Looking at the mean thickness curve, two different regimes are visible- a fast reaction rate is apparent between 1 and ~10 minutes followed by a much slower rate as evidenced by the thickness plateau after 10 minutes. Standard deviation increases with increasing polymer thickness and the standard deviation of hydrated samples tends to follow the relative standard

deviation of the corresponding unhydrated sample. In later experiments, this curve was used to determine reaction time in order to obtain pNIPAAm samples of the desired thickness.

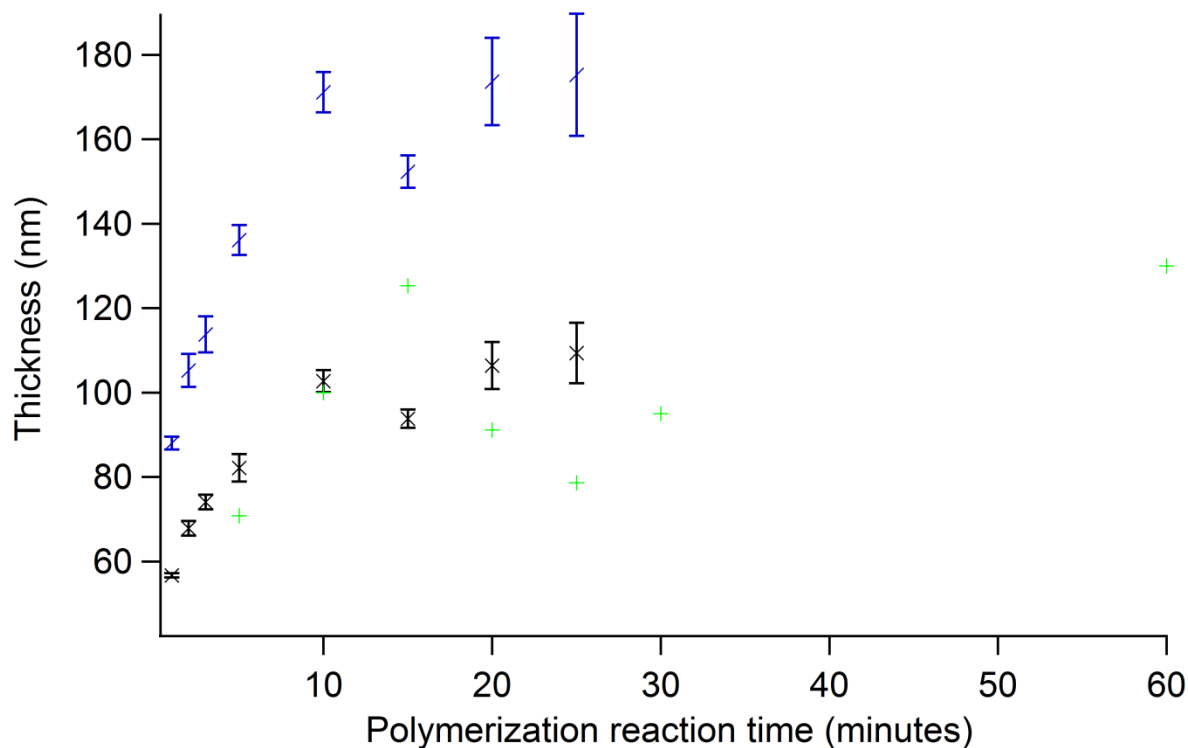


Figure 3.6. Ellipsometry and profilometry measurements of pNIPAAm from polymerization time trials. Unhydrated (black x) and hydrate (blue /) ellipsometry at each reaction time were performed on the same sample, profilometry (green +) was carried out on a different set of unhydrated samples. Silanization reaction time is constant at 1 hr for the ellipsometry samples and varies between 5 min and 48 hrs for the profilometry samples.

3.4 Single molecule tracking quality samples

Scattering from dust particles and emission from point source contamination can be mistaken for the fluorescence from inserted probe molecules and hinder accurate determination of probe movement. Obtaining samples ‘clean’ enough for single molecule tracking experiments

is quite challenging. For one thing, there are many sources of contamination throughout sample preparation – dust and organic molecules in ambient air, solvents, and solutions; contamination in reagents; other fluorophores on instruments and microscopes – and the usual procedures for cleaning SMT samples would destroy the organic polymer brush, if used after synthesis. Therefore, special measures were taken when preparing surface tethered pNIPAAm intended for SMT experiments in order to obtain samples with less than ~10 fluorescent or scattering point source contaminants in the microscope imaging area (up to 60000 μm^2). In total, four adjustments were made: reducing the number of solvents the sample was exposed to, use of low fluorescence methanol in the synthesis as specified in the materials section, removal of remaining Cu complex after polymerization by sonication in an EDTA solution, and photobleaching of the finished samples with an LED lamp and the SMT excitation laser prior to photobleaching. The EDTA treatment and photobleaching procedure are detailed below.

3.4.1 Excess copper removal with EDTA solution. A paper by Sonmez *et al.* outlines a method using an EDTA extraction to remove residual Cu-PMDETA complex from ATRP synthesized pNIPAAm.¹¹ The modified procedure used here consists of sonicating for 1 hr in 0.1 M EDTA aqueous solution followed by rinsing with DI water and MeOH and then drying with nitrogen. This treatment removes larger high intensity spots that do not blink or photobleach, although there is still plenty of ‘single molecule’ fluorescence before the addition of probe fluorophore.

3.4.2 Photobleaching with LEDs and lasers. The remaining single molecule contamination can be removed with a regimen of two photobleaching periods- one of the entire sample and one of the collection area. First, the whole sample is photobleached with a bank of 490 nm LEDs for 2-

5 days. Photobleaching the whole sample removes ~ 90% of the original contamination, so there might be fewer than 100 diffraction limited spots in a 100 μm x 100 μm field of view. Photobleached pNIPAAm samples stay ‘cleaner’ if stored in a covered container in DI water. If a sample is stored in air, even in a closed container, the polymer picks up enough dust in <24 hours to be noticeable under the fluorescence microscope. For this reason, photobleaching with the LED lamp was carried out on samples that were sealed in containers filled with DI water.

In the second step, the sample is exposed to the excitation laser for ~5 minutes on the imaging microscope in widefield configuration in order to photobleach the collection area. This removes most of the residual ‘SM’ contamination so that <10 diffraction limited spots remain in the field of view. Although photobleaching the field of view with the excitation laser is much quicker than exposing the whole sample, the longer first step is crucial to obtaining clean enough samples for SMT. In samples with single spot photobleaching only, contamination from the surrounding areas diffused into the field of view over the course of tens of minutes, which is the same time scale as the data collection period.

3.5 Lower critical solution temperature characterization

3.5.1 Temperature-controlled ellipsometry with hydrated pNIPAAm. A custom built cell with polystyrene windows at 70° angles (normal to the incident and reflected laser light) was used to collect ellipsometry data. The aluminum floor of the cell was glued with silver epoxy to an aluminum disc that was fitted with a temperature collar (Biopetechs) with 0.1°C resolution capable of producing temperatures in the range $\sim 19^\circ\text{C} < T < 43^\circ\text{C}$ depending on ambient room temperature. The polymer on silicon sample was placed inside the cell and immersed in DI water. Ellipsometry data were collected at temperatures $19^\circ\text{C} < T < 37^\circ\text{C}$ at $\sim 1^\circ\text{C}$ intervals at λ

= 632.8 nm, with refractive index and thickness of the polymer layer simultaneously determined. Solution temperatures were measured using two separate thermistors in close proximity to the sample. The refractive index and thickness of the polymer layer were determined from Ψ and Δ using the Gaertner GEMP software following standard single wavelength ellipsometry calculations.^{12,13}

Figure 3.7 shows the temperature response of a hydrated pNIPAAm brush on a silicon wafer, which exhibited 80 nm dry thickness. The ellipsometry results illustrate that the brush is thickest at 21°C and simultaneously reduces its thickness and increases its refractive index continuously until 32°C. Above 32°C, the thickness of the brush begins to increase again, which can be explained by increased thermal motion overcoming entropic forces. The gradual thickness transition between 21 and 32°C observed here is typical for high density pNIPAAm brushes¹⁴ as reported in the literature from surface plasmon resonance,¹⁵ water contact angle,^{16,17} quartz crystal microbalance,¹⁸ neutron reflectometry,¹⁹ sum frequency generation,²⁰ surface forces apparatus,²¹ atomic force microscopy,²¹ proton NMR,²² neutron reflectometry,^{23,24} cyclic voltammetry,²⁵ and ellipsometry.⁸ These reports, however, show no evidence of the increase in polymer thickness above 32°C that is observed here. However, only a few of the sources listed above include thickness data in the region above the LCST. Contact angle¹⁶ and SPR²⁶ results are reported at $T > T_{LCST}$ and do not show a trend toward to $T < T_{LCST}$ values. However this does not preclude an overall thickness increase, as thickness changes are due to both bulk and surface phase transitions, as evidenced by neutron reflectometry results.¹⁹

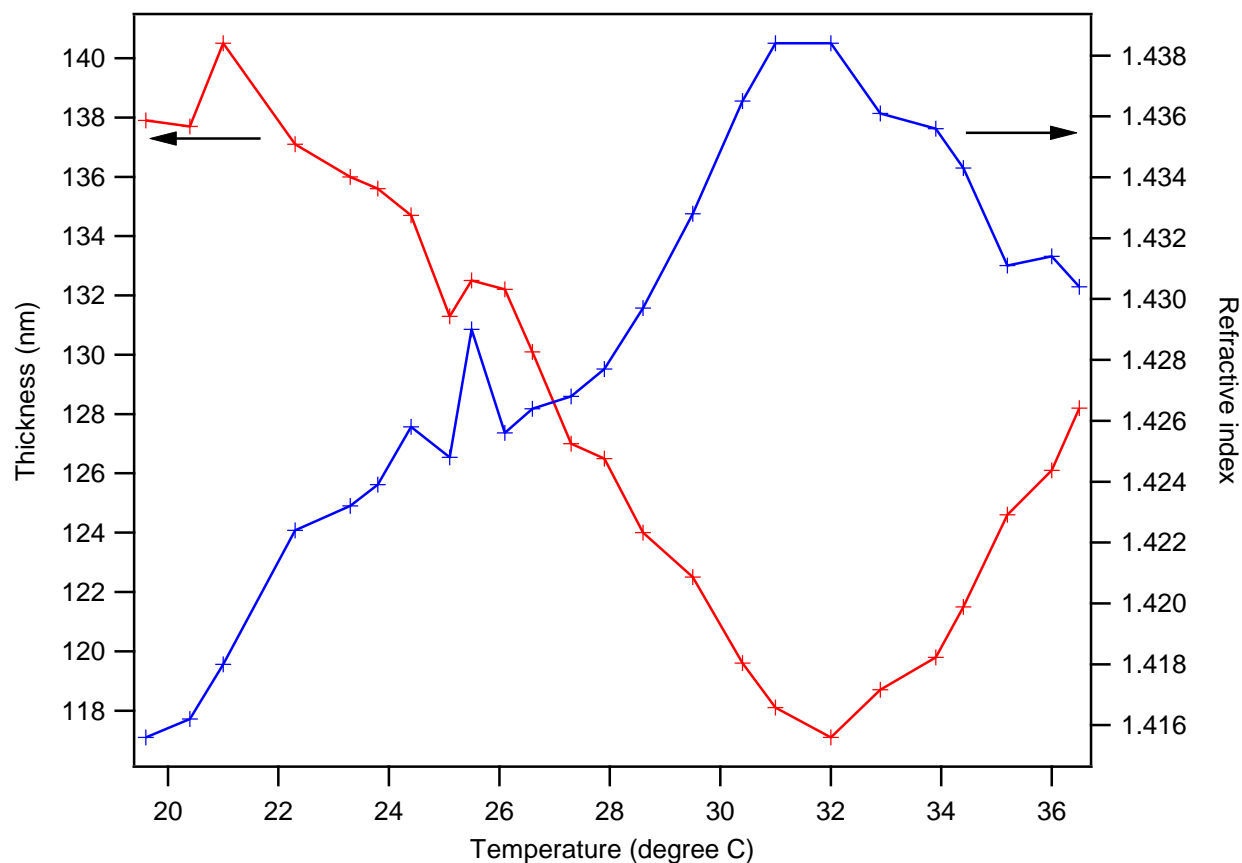


Figure 3.7: Ellipsometric measurements of thickness (red) and refractive index (blue) as a function of temperature for hydrated pNIPAAm synthesized on Si with 5 min reaction time. Film displayed 80 nm dry thickness.

As discussed in the introduction and literature review of the LCST of pNIPAAm, many factors, including grafting density and molecule weight can influence the phase transition of surface tethered brushes. These measurements were used to determine data collection temperatures, 23°C and 32°C, for the SMT experiments, at which maximal differences in transport behavior might be expected.

3.6 References

- (1) Matyjaszewski, K.; Miller, P. J.; Shukla, N.; Immaraporn, B.; Gelman, A.; Luokala, B. B.; Siclovan, T. M.; Kickelbick, G.; Vallant, T.; Hoffmann, H.; Pakula, T. *Macromolecules* **1999**, *32*, 8716-8724.
- (2) Kong, X. X.; Kawai, T.; Abe, J.; Iyoda, T. *Macromolecules* **2001**, *34*, 1837-1844.
- (3) von Werne, T. A.; Germack, D. S.; Hagberg, E. C.; Sheares, V. V.; Hawker, C. J.; Carter, K. R. *J. Am. Chem. Soc.* **2003**, *125*, 3831-3838.
- (4) Edmondson, S.; Osborne, V. L.; Huck, W. T. S. *Chem. Soc. Rev.* **2004**, *33*, 14-22.
- (5) Liu, P.; Guo, J. S. *Colloids Surf., A* **2006**, *282*, 498-503.
- (6) Li, P. F.; Xie, R.; Jiang, J. C.; Meng, T.; Yang, M.; Ju, X. J.; Yang, L. H.; Chu, L. Y. *J. Membr. Sci.* **2009**, *337*, 310-317.
- (7) Wang, X. J.; Tu, H. L.; Braun, P. V.; Bohn, P. W. *Langmuir* **2006**, *22*, 817-823.
- (8) Tu, H.; Heitzman, C. E.; Braun, P. V. *Langmuir* **2004**, *20*, 8313-8320.
- (9) Bao, Z. Y.; Bruening, M. L.; Baker, G. L. *J. Am. Chem. Soc.* **2006**, *128*, 9056-9060.
- (10) Lokuge, I., University of Illinois, U-C, 2006.
- (11) Sonmez, H. B.; Senkal, B. F.; Sherrington, D. C.; Bicak, N. *Reactive & Functional Polymers* **2003**, *55*, 1-8.
- (12) Tompkins, H. G. *A User's Guide to Ellipsometry*; Academic Press, Inc.: San Diego, CA, 1993.
- (13) Tompkins, H. G.; Irene, E. A. *Handbook of Ellipsometry*; William Andrew Publishing: Norwich, NY, 2005.
- (14) Barbey, R.; Lavanant, L.; Paripovic, D.; Schuwer, N.; Sugnaux, C.; Tugulu, S.; Klok, H. *A. Chem. Rev.* **2009**, *109*, 5437-5527.

- (15) Balamurugan, S.; Mendez, S.; Balamurugan, S. S.; O'Brien, M. J.; Lopez, G. P. *Langmuir* **2003**, *19*, 2545-2549.
- (16) He, Q.; Kuller, A.; Grunze, M.; Li, J. B. *Langmuir* **2007**, *23*, 3981-3987.
- (17) Sun, T. L.; Wang, G. J.; Feng, L.; Liu, B. Q.; Ma, Y. M.; Jiang, L.; Zhu, D. B. *Angew. Chem. Int. Edit.* **2004**, *43*, 357-360.
- (18) Annaka, M.; Yahiro, C.; Nagase, K.; Kikuchi, A.; Okano, T. *Polymer* **2007**, *48*, 5713-5720.
- (19) Ishida, N.; Biggs, S. *Langmuir* **2007**, *23*, 11083-11088.
- (20) Kurz, V.; Grunze, M.; Koelsch, P. *ChemPhysChem* **2010**, *11*, 1425-1429.
- (21) Malham, I. B.; Bureau, L. *Langmuir*, *26*, 4762-4768.
- (22) Wei, Q. S.; Ji, J.; Shen, J. C. *Macromol. Rapid Commun.* **2008**, *29*, 645-650.
- (23) Vidyasagar, A.; Majewski, J.; Toomey, R. *Macromolecules* **2008**, *41*, 919-924.
- (24) Yim, H.; Kent, M. S.; Mendez, S.; Lopez, G. P.; Satija, S.; Seo, Y. *Macromolecules* **2006**, *39*, 3420-3426.
- (25) Yin, Z. Z.; Zhang, J. J.; Jiang, L. P.; Zhu, J. J. *J. Phys. Chem. C* **2009**, *113*, 16104-16109.
- (26) Raula, J.; Shan, J.; Nuopponen, M.; Niskanen, A.; Jiang, H.; Kauppinen, E. I.; Tenhu, H. *Langmuir* **2003**, *19*, 3499-3504.

CHAPTER 4

SINGLE MOLECULE FLUORESCENCE MICROSCOPY, OPTICS, AND AUTOMATED TRACKING

This chapter covers the experimental and practical details of single molecule fluorescence microscopy, total internal reflection fluorescence (TIRF), and single molecule tracking (SMT). In addition, basic operation of the microscope and the Matlab tracking program are described.

4.1 Single molecule fluorescence microscopy

The microscope is an objective-based total internal reflection fluorescence (TIRF) instrument built on an Olympus IX71 body, as illustrated in Figure 4.1. The excitation source is a low power sapphire 488 nm laser with 20 mW maximum output (Coherent Inc). Light exits the laser with a total diameter of 7 mm and reflects off a plane mirror after which two lenses- a plano-convex ($f = 6.5$ mm) and an apochromat doublet ($f = 100$ mm)- serve as a $\sim 15X$ Keplerian beam expander (Newport Corp). The expanded beam passes through a 13 mm diameter beam stop in order to reduce stray reflections and non-Gaussian beam shape elements. A converging lens ($f = 200$ mm) focuses the beam onto the back focal plane of the infinity corrected objective. A band pass dichroic beamsplitter (Chroma Technology Corp) reflects light into a 100X 1.45 NA oil immersion objective (Olympus). Fluorescence light is collected by the same objective, passes through the dichroic, and through a band pass emission filter (Chroma Technology Corp). A 1X or 1.6X tube lens creates an image on a back illuminated iXon^{EM}+ EMCCD (Andor Technology). The CCD consists of a 512 x 512 array of $256 \mu\text{m}^2$ pixels and has $>90\%$ QE. The CCD is controlled by Solis software provided by Andor Technology. The microscope has a

calculated 520 nm depth of field in widefield configuration and a 100-200 nm depth of excitation in TIRF mode. In addition, the instrument has a 57 (91) μm field of view and a 100 (160) nm effective pixel size with 160X (100X) magnification.

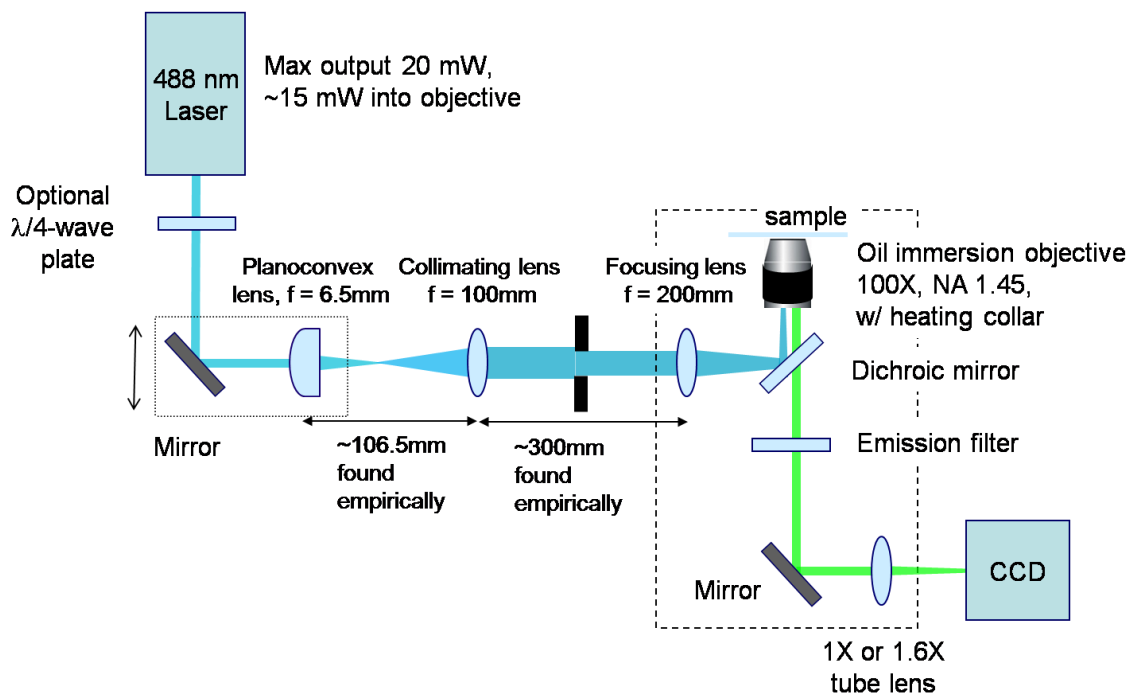


Figure 4.1: Schematic of the objective-based total internal reflection microscope (TIRFM).

Optics positioned within the microscope body are shown inside the dashed rectangle.

The field of view of a microscope is measured by using scattered laser light to image a ruled stage micrometer in the sample plane. Given the known tick spacing of the stage micrometer, the visible area is measured in terms of image space. This verifies the magnification of the microscope, which can depart from the expected value if the axial spacing between optics is not accurate. The magnification and the actual pixel size are used to calculate the effective pixel size, which is important in single molecule tracking experiments.¹ The depth of field and diffraction limited spot size are calculated from the following equations, respectively:²⁻⁴

$$D_{field} = \frac{\lambda \cdot n}{NA^2} + \frac{n}{M \cdot NA} e \quad (4.1)$$

$$Spot\ size = 0.61 \cdot \lambda / NA \quad (4.2)$$

where λ is the wavelength of excitation light, n is the refractive index of the medium (immersion oil in this case), NA is the numerical aperture of the objective, M is the objective magnification, and e is the smallest distance that can be resolved by a detector that is placed in the image plane of the microscope objective. For this setup, $\lambda = 0.488\ \mu\text{m}$, $n = 1.518$, $NA = 1.45$, $M = 100$, and $e \sim 16\ \mu\text{m}$ (calculated from pixel size of $0.16\ \mu\text{m}$ magnified by 100X objective) which results in the $520\ \text{nm}$ depth of field and $205\ \text{nm}$ diffraction limited spot size, illustrated in Figure 4.2.

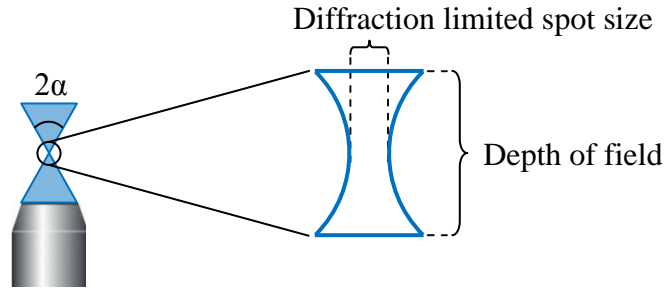


Figure 4.2: Schematic of the diffraction limited spot size and depth of field for the illumination and the angle of collection, α , from a microscope objective, all of which depend on the numerical aperture, NA , of the lens.

4.2 Optics and fluorophores

4.2.1 Choice of circular polarization, filters, lens positions. An optional $\lambda/4$ plate is in position immediately after the laser in order to transform the vertical linearly polarized light to circularly polarized light. This optic is used in order to achieve more homogeneous TIRF illumination for samples in which the fluorophores were not rotating freely. The dichroic beamsplitter and the

emission filter are chosen so that the cutoffs match the excitation source and the fluorophore being used in the experiment. In all cases, the dichroic should reflect the excitation light and transmit the fluorophore emission. In addition, the emission filter should have high transmission for the fluorophore emission and low transmission for the excitation light- this would be true for a band pass and for a high pass filter with the correct cutoffs. A Chroma filter set for a 488 nm excitation is shown in Figure 4.3, the dichroic and emission filters would match fluorophores that emit between 500 and 550 nm and for comparison the absorption and emission spectra for Bodipy FL (more detail in Section 4.2.2) are overlaid. As illustrated, both filters have zero or near-zero transmittance at the 488 nm laser line, which overlaps nicely with the absorption spectra. The dichroic mirror and emission filter both transmit strongly in the range of the Bodipy emission. If noise is a problem in the system, multiple emission filters can be employed at the same time. Emission filter position along the beam path is arbitrary, however lens positions are necessarily very specific. The axial positions for several lenses were found empirically: 1) the $f = 6.5$ mm lens was adjusted until the beam coming out of the $f = 100$ mm lens was collimated and 2) the $f = 200$ mm lens was adjusted until the beam coming out of the objective was collimated.

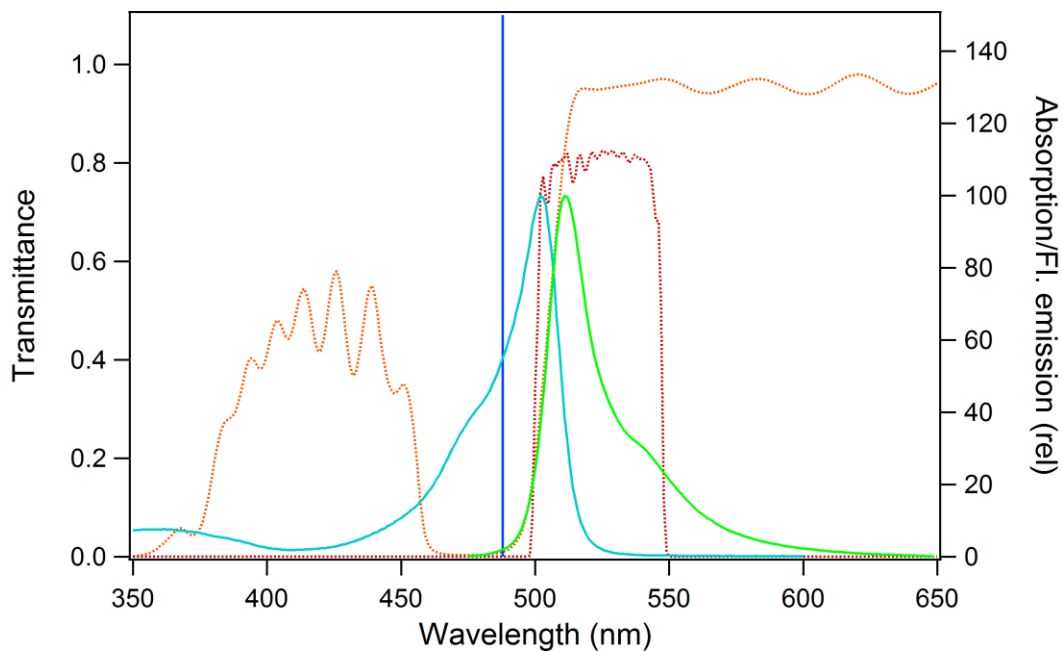


Figure 4.3: Transmittance data for a 488 nm laser filter set from Chroma and spectra for Bodipy FL. The orange trace is the dichroic mirror (Z488RDC, a long pass) and the red trace is the emission filter (HQ525-50, a band pass), with the royal blue laser line at 488 nm. The light blue trace is the absorption spectrum and the green trace is the emission spectrum for Bodipy FL.

This microscope went through several design iterations before culminating in the final configuration with TIRF capabilities on a microscope body. Focusing stability, sample position steadiness, and background noise levels are all much improved using a microscope frame relative to individual components. For example, on component-based instruments the sample or focus could drift over time, sometimes within the span of tens of seconds. Clearly, this is a problem for image acquisition of movies that span several minutes. In addition, large amounts of baffling

were used to block out stray light, yet the background levels were never as low as those achieved with the microscope body.

4.2.2 Fluorophore selection. Several factors should be considered when choosing a probe fluorophore including solubility, interaction with the sample matrix, quantum yield, photostability, and absorption and emission maxima. Three main fluorophores were used in single molecule tracking experiments during the course of this thesis project: 4,4-difluoro-5,7-dimethyl-4-bora-3a,4a-diaza-s-indacene-3-propionic acid (Bodipy FL), 1,1'-dioctadecyl-3,3,3',3'-tetramethylindocarbocyanine perchlorate (DiIC₁₈), [9-(2-ethoxycarbonylphenyl)-6-(ethylamino)-2,7-dimethylxanthen-3-ylidene]-ethylazanium (R6G), chemical structures displayed in Figure 4.4. The quantum yield and photobleaching lifetimes of all three fluorophores are sufficient for use in single molecule experiments and in each case, the fluorophore used had high absorption of the excitation light. Other fluorophores that were tried in SMT experiments with varying degrees of success include FITC labeled Dextrans of various molecular weight, AlexaFluor 488, and DiO. Bodipy FL was picked because it is a neutral, yet water soluble dye, which is an attractive combination for experiments in aqueous solution and with minimal desired interactions between the polymer chains and the probe. DiIC₁₈ was chosen because it is a membrane dye that has higher quantum yield in hydrophobic environment than in aqueous solution, which led to extremely high signal-to-noise ratio, SNR, (see Sections 4.5.5 and 4.7 for more discussion on SNR) and easily identifiable single molecule features. R6G was selected because it is a widely used in SMT experiments.

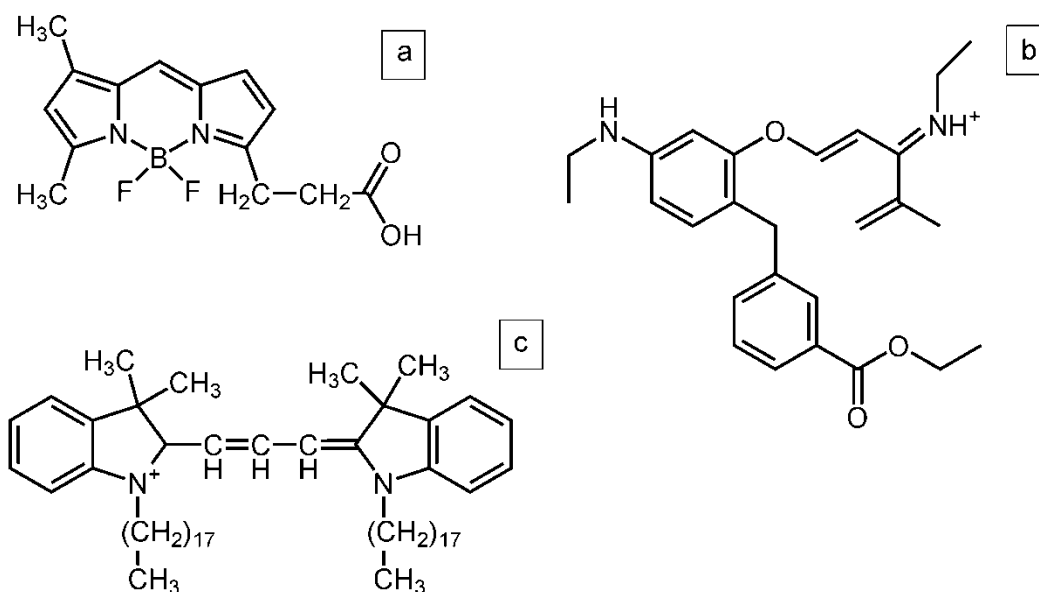


Figure 4.4: Chemical structures of (a) Bodipy FL, (b) R6G, and (c) DiIC₁₈.

4.3 Experimental achievement of total internal reflection

As shown in detail in Figure 4.5, the plane mirror and 6.5mm FL lens on the translation stage are moved laterally in order to bring the system into or out of total internal reflection. Widefield illumination is obtained with the beam aligned with the center of the objective, while total internal reflection (TIR) is achieved when the beam is translated away from the optic center (in either direction). The theory behind TIRF is covered extensively in Section 2.1.2, so only a brief practical description is given here. As the beam is translated, the light transmitted through the objective begins to exit at an angle from the vertical. Eventually the beam is far enough off-center to exceed the critical angle at the sample-water interface, described by Snell's Law. The critical angle, θ_c , depends on the excitation wavelength and the refractive indices of the two media in the sample. The two media are commonly glass and water, but this is certainly not a

strict limitation. TIR can be achieved as long as the difference in refractive indices is large enough for the microscope objective to attain this angle (72° in the case of a 1.45 NA lens).

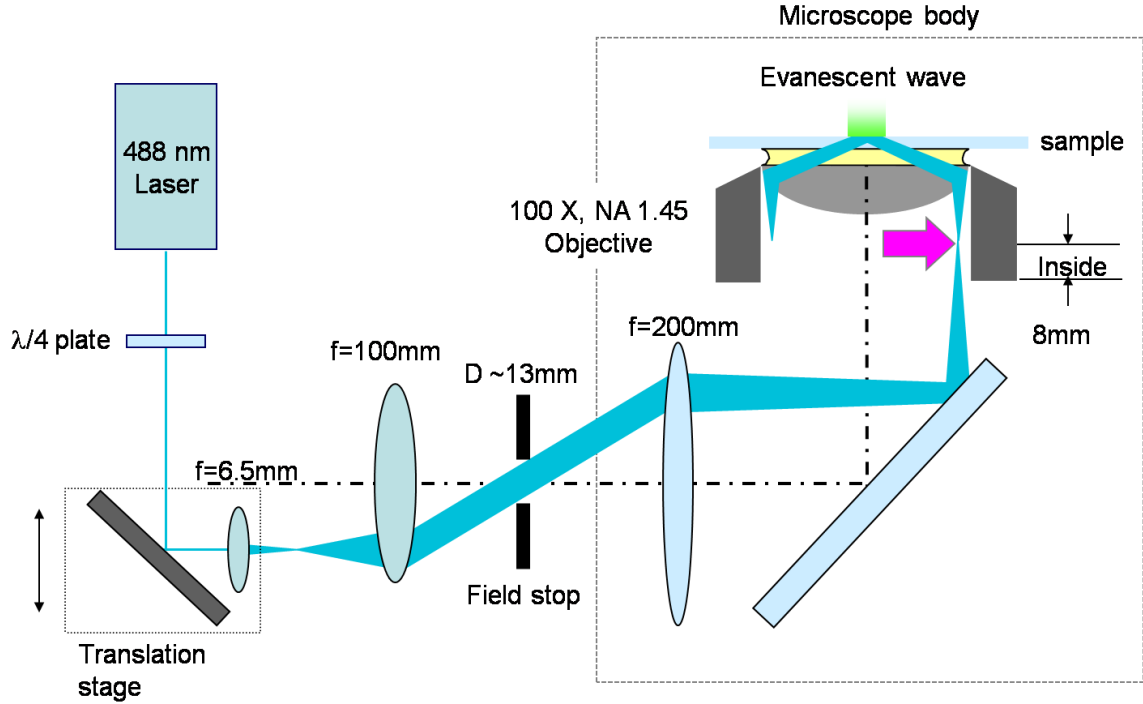


Figure 4.5: Detail of total internal reflection (TIR) mode on the single molecule tracking microscope.

The state of system can be monitored by observing the appearance of the illumination light on the sample and by the appearance of the image obtained on the CCD. At illumination angles below θ_c , the excitation light looks like a spot on the surface of the substrate and propagates away from the surface at an oblique angle. When TIR is achieved the spot on the surface becomes a line several millimeters long and the beam propagating away from the surface disappears. In addition, the edges of the substrate will scatter illumination light. Care should be taken when bringing the microscope into TIR, as the beam sweeps across the room and could

easily be at eye level. The system can also be monitored by watching the image obtained on the CCD as the beam is translated. As soon as TIR is achieved, any point sources of fluorescence on the surface of the sample will become much brighter (signal-to-noise ratio will increase). This method requires that the surface be in focus, of course, which can generally be done when the microscope is in widefield illumination, if there are enough features on the surface.

It is also necessary to adjust the position of the beam so that the TIRF illumination area is aligned with the CCD (it is possible to exceed θ_c by too much). This is also done empirically by watching the image on the CCD while moving the beam. After TIR is achieved for a given sample, the critical angle will be maintained even when the stage is moved to view different parts of the sample. In addition, samples of the same composition can generally be substituted without reestablishing the critical angle.

4.4 Instrument capabilities

4.4.1 Temperature control. The heating system consists of a stage insert sample holder and an objective heater, along with an aluminum foil boat, a plastic thermal insulator between the objective and the microscope nose turret, and two thermistors for manual feedback. Carefully balanced heating output of both the stage insert heater (2-3 W max output) and the objective heater (7-8 W max output) produces a uniform temperature profile along the surface of the coverglass when using a glass bottomed petri dish covered in Al foil. The sample holder alone is not enough to provide constant temperature throughout the sample due to the large heat sinking capacity of the objective. On the other hand, using the objective heater alone results in a hot spot at the point of contact between sample and objective (facilitated by the immersion oil) and rapid cooling away from the center. Also, it is important to cover the glass bottomed petri dish with a

lid in order to reduce evaporation of the hydrating solution. 35 mm glass bottomed petri dishes can be purchased as is (MatTek, No 1.5, 20 mm diameter coverglass) or coverglass (Electron Microscopy Sciences, Bellco 25 mm diameter coverglass, No, 1.5) and polystyrene petri dishes (Fisher Scientific, 20 mm diameter petri dish) can be purchased separately, machined, and attached with a non-fluorescent adhesive or grease to form the final product. Remembering that polystyrene is soluble in various organic solvents and that the glue adhering the coverglass and petri dish is also soluble in solvents other than water and alcohols, the choice between these two options is determined by ease of sample synthesis with the ready-made glass bottomed petri dishes.

4.4.2 Shutter delay. The capability to define a delay time in the acquisition cycle was added to the Andor camera, which allowed the ~15 ms opening time for the mechanical shutter that controls laser illumination to be taken into account. This setup has the capability of taking movies with a short exposure time followed by a long delay time while exposing the sample to excitation only during the data collection windows.

4.5 Microscope characterization

4.5.1 Optical efficiency measurements. A power meter was used to measure the transmission efficiency of all the optics in the apparatus; results are shown in Figure 4.6.

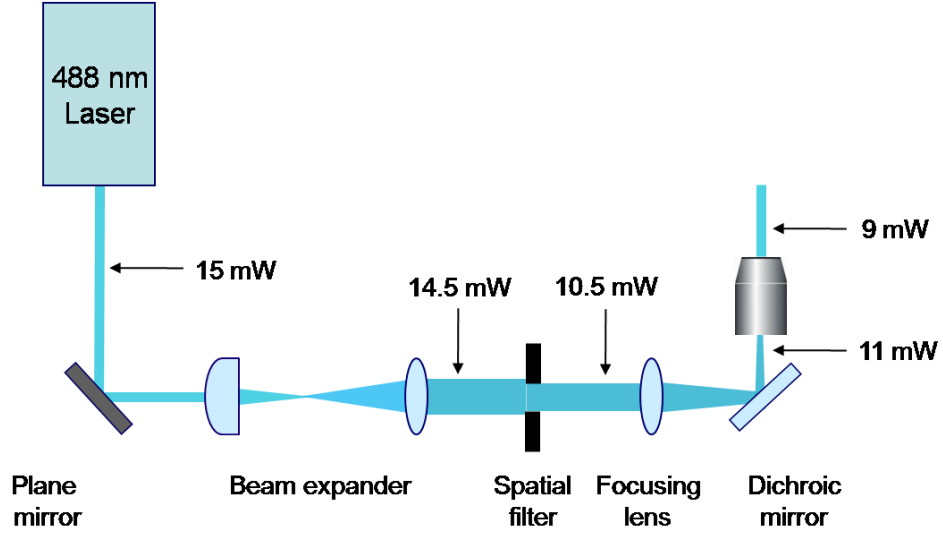


Figure 4.6: Transmission losses of excitation optical path, with final illumination power 9 mW at starting laser output 15 mW, for a total 60% efficiency.

4.5.2 *Charge coupled device characterization.* Pseudo zero exposures (camera shutter closed) were obtained with 10 microsecond exposures, 0 EM gain movie for 100 consecutive frames. These movies were analyzed for background and for noise, defined by:

$$Background_i = Mean(all\ pixels\ in\ frame_i) \quad (4.3)$$

$$Noise_i = Standard\ deviation(all\ pixels\ in\ frame_i) \quad (4.4)$$

As seen in Figure 4.7, the black trace for background between 328 and 330 counts/pixel/10 μ s was observed with a slight rise starting at 328 and leveling off at 329.5 counts around 30 frames. Also shown in Figure 4.7, the red trace for noise is closely centered at 4.07, except for the first frame which starts at 4.2. The higher noise in the first frame is due to the chip cleaning process

used after each exposure, so slightly more electronic noise is present before the 1st cleaning cycle.

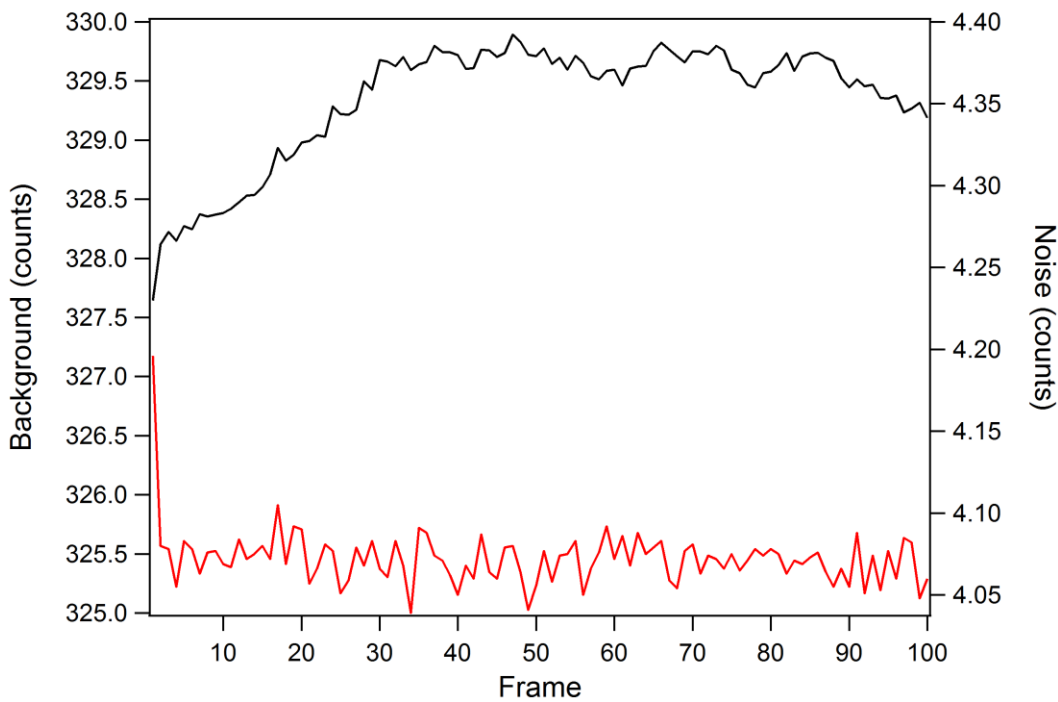


Figure 4.7: ‘Zero exposure’ data for 10 μ s, 0 electron multiplying gain, 4.5 pre-amp gain on the iXon^{EM}+ EMCCD. The black trace is background (mean of all pixels in the exposure) while the red trace is noise (standard deviation of all pixels in the exposure).

4.5.3 Improved background and noise levels. Adding extra baffling improved the background and noise as shown in measurements of the excitation light scattering from a glass slide (no fluorophore present) with 100 ms exposure, 0.2844 mW illumination (~ 0.0145 kW/cm² assuming an illumination spot with 50 μ m diameter), electron multiplying gain = 6.

Photons above dark counts/pixel/100 ms

Starting point: 74 ± 14

After several iterations of baffling: 44 ± 10

4.5.4 *Improved excitation profile.* After initial construction, the Keplerian beam expander and the spatial filter were modified to vignette the beam by about $\frac{1}{3}$ - $\frac{1}{2}$ in order to obtain a flatter excitation profile, (spatial filter in Figure 4.6) resulting in less variation across the illumination area and a lower noise level. As measured in the reflection off a glass slide again, with 100 ms exposure, 9.6 mW illumination power ($\sim 0.49 \text{ kW/cm}^2$ with 50 μm illumination spot diameter), and electron multiplying gain = 6.

Photons above dark counts/pixel/100 ms
With clipped Gaussian: 42 ± 8

*Reasonable values for illumination intensities for SMT taken from Bagh and Paige⁵ are 0.5-6.0 kW/cm^2 .

4.5.5 *Single molecule signal to noise ratio in pNIPAAm.* One frame from a movie of a 100 nm pNIPAAm film exposed to 10^{-10} M Bodipy FL is displayed in Figure 4.8. The 1000 frame movie was collected with 20 ms exposures, 55.59 ms kinetic cycle time, 20 mW laser power, 100X, electron multiplying gain = 200, pre-amp gain = 4.9, and with baseline clamp under TIRF configuration at 29.5°C.

Signal-to-noise ratio (SNR) is calculated by:

$$SNR = \frac{\text{Peak intensity-mean background}}{\text{background noise}} \quad (4.5)$$

For this sample molecule, SNR is 45, which is well above the nominal cutoff of 10 for single molecule tracking. The background is taken as the area surrounding the peak with no visible features, and the noise is the standard deviation of the signal in this section.

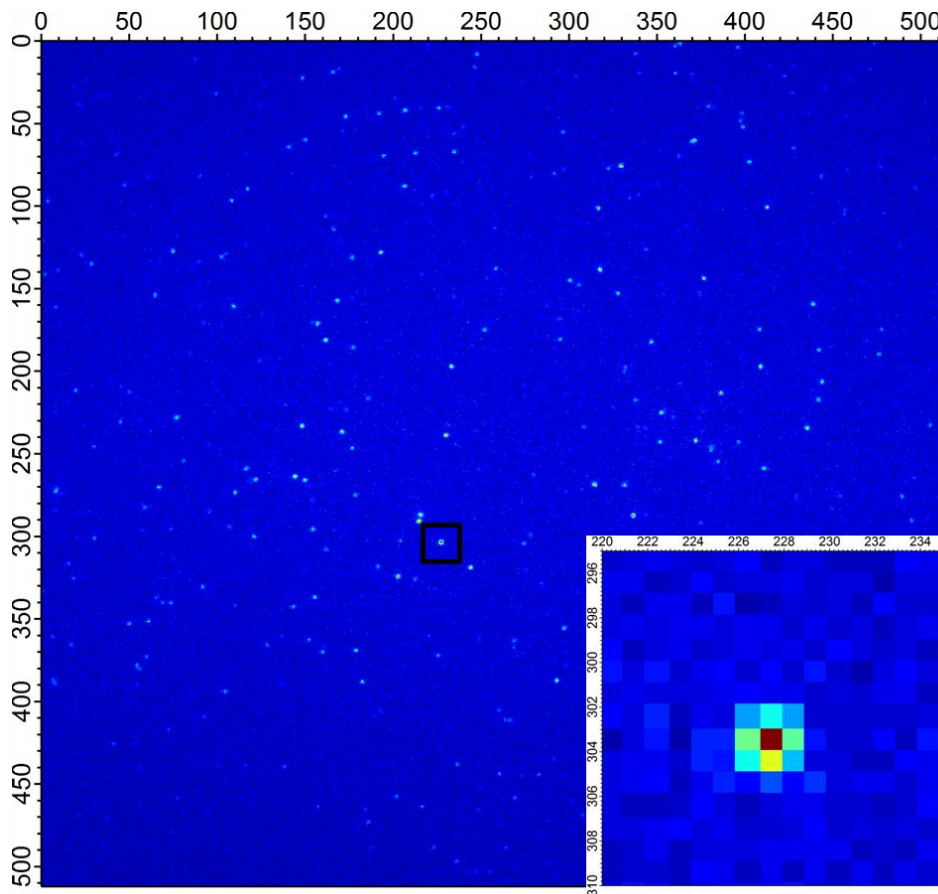


Figure 4.8: Fluorescence image of 10^{-10} M Bodipy FL in pNIPAAm with background 530 ± 125 counts. The inset shows a diffraction limited spot for a single molecule with peak intensity 6138 counts and signal-to-noise ratio of 45. The mean and standard deviation of peak intensities for all single molecule features in this frame is 1434 ± 855 counts (background corrected).

4.6 Single molecule tracking software

Tracking is carried out in a modified Matlab program^{6,7} that was developed for single molecules.^{8,9} Briefly, tracking consists of the linked tasks of (1) single molecule feature identification, (2) localization and (3) trajectory reconstruction. Identification and localization

are realized by fitting the spatial intensity profile of each candidate molecule to a 2-D Gaussian given by,

$$I(x,y)= I_o \exp \left(-\frac{(x-x_0)^2}{2\sigma_x^2} - \frac{(y-y_0)^2}{2\sigma_y^2} \right) \quad (4.6)$$

where the centroid (x_0,y_0) and the peak standard deviations (σ_x,σ_y) are obtained from a weighted linear least squares fit. The ratio of the peak height, I_0 , to the surrounding average noise is used to calculate the SNR and identify the peak as arising from a candidate single molecule, and localization is achieved by identifying the center of the mathematical function (x_0,y_0) . Using this procedure, the centroid can be localized with better precision than the diffraction limit. After every feature is identified in each frame, the frames are stacked in a movie and trajectories are linked together throughout the course of the movie. These trajectories form the basis for detailed statistical treatments described in Chapter 6.

4.6.1 Tracking with blinking capability. Memory, or the capacity to continuously track molecules that are missing for a number of frames within a single trajectory, is important because single fluorescent molecules exhibit intermittent blinking behavior, which is discussed further in Section 4.7. The Matlab tracking program has the option to link features that are separated by a user-defined number of frames. The length of time a feature can be absent and still be counted as the same molecule is a delicate choice with moving molecules, however, and must be selected carefully.

4.6.2 Practical use of single molecule tracking Matlab program. Table 4.1 shows a summary of inputs, used defined parameters, algorithm choices, outputs, plots, and movies.

Table 4.1: Summary of Matlab single molecule tracking program options.

<i>Input</i>	.tif or .sif movie, before or after background subtraction	
<i>Key user defined parameters</i>	Peak minimum, integrated brightness minimum, maximum displacement between frames, molecule diameter, eccentricity, radius of gyration, number of frames a molecule can be absent (for trajectory reconstruction with memory available)	
<i>Feature finding</i>	Local maxima are identified, compared to the peak minimum, and screened against brightness, eccentricity, radius of gyration. Localization based on centroid finding only.	
<i>Localization (choice between two methods)</i>	A rapid matrix method is used to pseudo fit a 2D Gaussian to the data by weighted linear least squares.	
	A non linear least squares optimization is employed to fit a 2D Gaussian to the data. This method can handle elliptical and tilted Gaussians.	
<i>Trajectory reconstruction (choice between two methods)</i>	Features are linked together based on a sparse matrix of maximized probabilities involving weighted integrated brightness and displacement between frames, no memory (temporary absence of the molecule for any number of frames results in a new trajectory).	
	This algorithm also uses a probability matrix to differentiate between all the possible trajectories. It's a direct translation of original IDL track.m (and available on Blair and Dufresne website). Memory is available.	
<i>Outputs</i>	Msqr	Time, Mean squared displacement, Number of trajectories that survived this many frames
	Traj	X centroid, Y centroid, Integrated brightness, Radius of gyration, Eccentricity, Frame number, Molecule ID, Number of frames this molecule has been tracked so far, Y displacement since the last position, X displacement since the last position, Squared displacement of the molecule so far
<i>Plots</i>	Individual mean squared displacement v. time, (w/ and w/o error bars)	
	Ensemble mean squared displacement v. time, (w/ and w/o error bars)	
	Molecule trajectories (x position v. y position)	
	Integrated brightness v. time	
<i>Movies</i>	Reconstructed trajectories overlaid onto original movie.	

4.6.2.1 Comparison of feature finding algorithms. Feature finding without sparse matrix or probability matrix localization, see Table 4.1, is surprisingly accurate considering there is no fitting process. However, for molecules located within certain areas of the pixel at certain SNRs, the center is routinely misidentified by feature finding. While the weighted linear least squares is a pseudo fit as opposed to the actual fit used in non-linear least squares, the position localization and integrated brightness in the weighted method is quite precise and quite accurate based on tests with simulated data that are detailed below. In addition, the weighted fit runs faster and smoother than the non-linear fit.

4.6.2.2 Trajectory reconstruction algorithm comparison. In order to keep computations manageable in both methods, matches are considered only within a limited distance- maximum displacement parameter input by the user. From localization methods in Table 4.1, the sparse matrix of maximized probabilities is desirable over a probability matrix when tracking movies with a high density of molecules, especially when the distance moved per frame is equal to or greater than the distance between molecules. However, if blinking molecules are to be tracked, the probability matrix method has the option of using memory in which that a feature can be missing for a user-defined length of frames and still counted as the same molecule.

4.6.2.3 Feature finding methods comparison. After the final version of the Matlab program was finished, the localization of simulated sample movies was performed for a stationary peak with random noise in each frame. The mean and standard deviation of the position and integrated brightness were compared at SNR = 5, 7.5, 15, 30, 40, and ∞ for feature finding with weighted

linear least squares and non-linear least squares fittings. The conclusions of this set of simulation analyses are as follows:

- 1) The weighted linear LS method is slightly more accurate and more precise in calculating integrated brightness at various SNRs than the non-linear LS method.
- 2) For both feature finding methods, it is better to overestimate diffraction-limited apparent molecular diameter than to underestimate it, in terms of integrated brightness.
- 3) Non-linear LS fitting is very slightly more accurate and more precise in calculating x and y position than weighted linear LS fitting.
- 4) Even at low SNR (5 and 7.5), both methods are capable of identifying the centroid and integrated brightness of a molecule.

4.6.2.4 Localization accuracy testing. Several sets of data with sample Gaussians were simulated at varying noise levels, with signal-to-noise ratios ranging between 5 and infinity (no noise). Figure 4.9 shows images of the simulated peaks and the localization error found in each case. The localization error is the distance from the defined center of the peak. It is interesting to note that in all cases above $\text{SNR} = 10$, the error is less than 0.1 pixels. For an effective pixel size of 100 nm, the corresponding spatial error would be 10 nm. This is well within the desired spatial resolution, and as seen in later experiments, mathematical localization is not the limiting factor in accurate determination of molecular position.

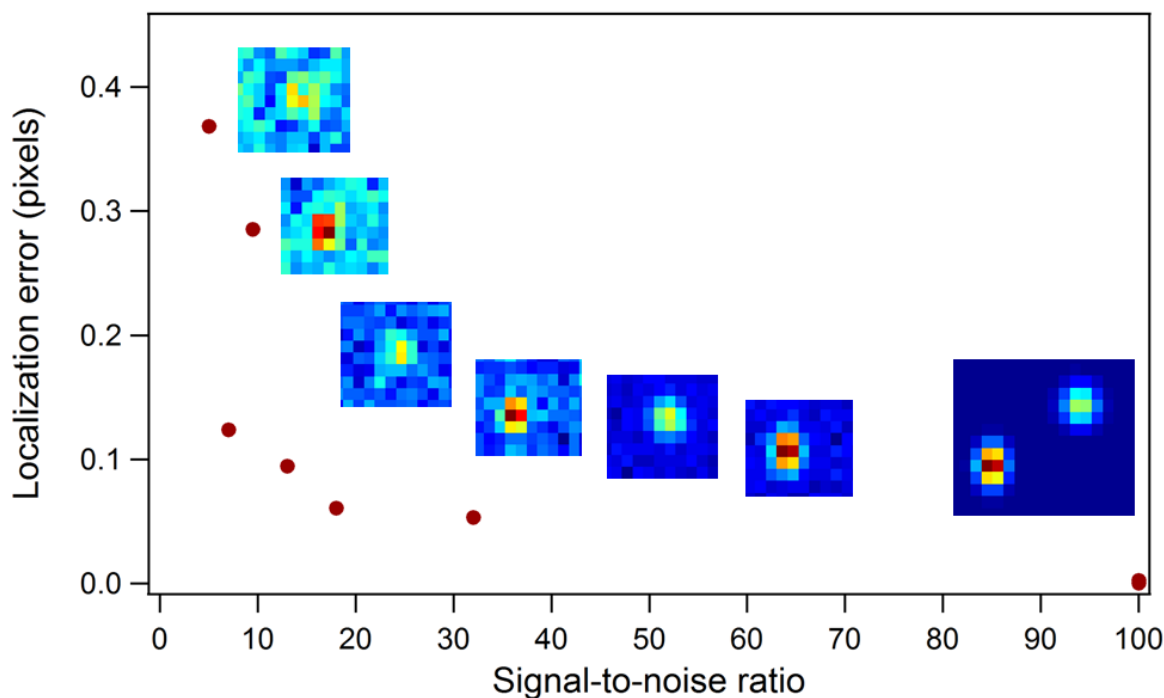


Figure 4.9: Simulated sample Gaussian peaks with SNR = 5, 7, 9.5, 13, 18, 32 and no noise (plotted at SNR = 100) and the localization error found with 2D Gaussian fitting with the weighted least squares feature finding in the Matlab tracking program.

4.7 Single molecule tracking considerations

Tracking the location of probe species with single molecule fluorescence imaging is affected by two important factors – length of the trajectory and signal-to-noise ratio (SNR).¹⁰ Trajectories can be interrupted or terminated by two well known characteristics of fluorescent molecules – blinking and photobleaching.¹¹⁻¹³ Blinking is a temporary condition in which the molecule enters a transient dark state, where it is incapable of fluorescent emission. Photobleaching is an inherent property of all molecular fluorophores, and results from the oxidative photochemistry of excited molecules in the presence of singlet oxygen.² This process is observed as a decrease in the number of emitting molecules in the field of view during the

illumination period at single molecule concentrations. Oxygen scavengers can be employed to decrease photobleaching rates, but excitation under anoxic conditions results in lower emission rates,¹⁴ which is undesirable due to its negative impact on SNR. Increasing SNR is a specific challenge for single molecule fluorescence experiments due to relatively low emission outputs compared to background noise.

While the observation window available for any given probe molecule depends on environmental factors, a reasonable value for the lifetime of a fluorophore lies in the range 10 s - 100 s. A second critical factor determining the amount of information gained from a trajectory is the frame rate of the tracking movie. As the frame rate increases, the number of individual points per trajectory also increases. However, the maximum frame rate is limited by the excitation intensity, the intrinsic photophysics of the probe and the need to collect sufficient emission photons in order to distinguish the single molecule signal from the background. The amount and quality of information that can be gained about the system of interest is, therefore, directly impacted by the photophysical limitations of molecule fluorophores.

4.8 References

- (1) Enderlein, J.; Toprak, E.; Selvin, P. R. *Opt. Express* **2006**, *14*, 8111-8120.
- (2) Qu, X. H.; Wu, D.; Mets, L.; Scherer, N. F. *Proc. Natl. Acad. Sci. U. S. A.* **2004**, *101*, 11298-11303.
- (3) Spring, K. R.; Davidson, M. W. "Nikon Microscopy U, Microscopy Basics- Depth of field and depth of focus." *Nikon*. Dec. 10, 2010. Web. 2000-2010.
- (4) Davidson, M. W. "Nikon Microscopy U, Microscopy Basics- Resolution." *Nikon*. Dec. 10, 2010. Web. 2000-2010.

- (5) Bagh, S.; Paige, M. F. *Can. J. Chem.* **2005**, 83, 435-442.
- (6) Anthony, S.; Zhang, L. F.; Granick, S. *Langmuir* **2006**, 22, 5266-5272.
- (7) Anthony, S. M.; Granick, S. *Langmuir* **2009**, 25, 8152-8160.
- (8) Weeks, E. R.; Crocker, J. C.; Levitt, A. C.; Schofield, A.; Weitz, D. A. *Science* **2000**, 287, 627-631.
- (9) Crocker, J. C.; Grier, D. G. *J. Colloid Interface Sci.* **1996**, 179, 298-310.
- (10) Kubitscheck, U.; Kuckmann, O.; Kues, T.; Peters, R. *Biophys. J.* **2000**, 78, 2170-2179.
- (11) Deschenes, L. A.; Bout, D. A. V. *Chem. Phys. Lett.* **2002**, 365, 387-395.
- (12) Schuster, J.; Brabandt, J.; von Borczyskowski, C. *J. Lumines.* **2007**, 127, 224-229.
- (13) van Dijk, M. A.; Kapitein, L. C.; van Mameren, J.; Schmidt, C. F.; Peterman, E. J. G. *J. Phys. Chem. B* **2004**, 108, 6479-6484.
- (14) Schuster, J.; Cichos, F.; von Borczyskowski, C. *Opt. Spectrosc.* **2005**, 98, 712-717.

CHAPTER 5

SINGLE MOLECULE TRACKING TRAJECTORY ANALYSIS*

5.1 *Single molecule trajectory analysis*

Experimental single molecule tracking datasets consist of mixed simple and intermittent diffusion populations with many different states. Due to the high levels of complexity, robust quantitative techniques are needed to elucidate the motional characteristics of various subpopulations of molecules. This chapter will introduce and characterize the four analysis methods that are applied to single molecule tracking, SMT, trajectories from the temperature based experiments of molecular probes in pNIPAAm that are detailed in Chapter 6.

Of particular interest in our laboratories is the use of SMT to understand the molecular-scale behavior of stimulus-responsive materials.¹ One of the major strengths of SMT is that it can be used to explore the physical or chemical heterogeneities that the probe molecules encounter as they move within their matrix. Instead of a single metric averaged over a population of probes, each trajectory is analyzed separately, and the distribution of molecular behavior is extracted from the ensemble of trajectories. For example, subpopulations of speed or type of movement can easily be detected and categorized.

Traditionally, the ensemble-averaged movement of particles (molecules) is characterized by the diffusion coefficient, D ,² which for simple Brownian motion is proportional to the slope of the linear mean squared displacement, MSD or $\langle x^2 \rangle$, versus time delay, τ , plot. Departures from simple Brownian behavior, resulting, for example, from confined (sub-linear) motion or from diffusion in the presence of flow (super-linear) are evident when examining $\langle x^2 \rangle$ vs. τ . For

*Partial content from Elliott, L.C.C.; Barhoum, M.; Harris, J.M.; Bohn, P.W. Phys. Chem. Chem. Phys., 2011, DOI: 10.1039/c0cp01805h. Reproduced by permission of The PCCP Owner Societies.

example, Kusumi *et al.* used this method to show how the diffusion of various membrane receptors differs from a simple random walk.^{3,4} However, the MSD alone cannot detect all deviations from Brownian motion. Intermittent confinement, a commonly encountered type of non-Brownian motion in which the probe alternates between low- and high-mobility states, is often averaged out in the MSD. Also, molecular trajectories are frequently too brief to observe long term deviations from Brownian motion. Nevertheless, the ability to identify and characterize confined states of motion is essential to developing a detailed understanding of motional dynamics in advanced materials at the molecular scale. Compounding the problem is the difficulty of obtaining quantitative data from individual trajectories, especially with single molecule probes. As discussed in Section 4.7, the amount of information gained from single molecules trajectories is ultimately limited by intrinsic properties of the probes such as blinking, photobleaching, and limited quantum yield. These constraints have to be addressed explicitly when developing tools for SMT trajectory analysis. With advances in fluorophore photobleaching lifetimes and microscopy technology, new single molecule tracking experiments are possible that have been used to illuminate cytoskeleton regulation of B-cell receptor diffusion and signaling in resting B cells,⁵ stepwise translocation of the nucleic acid motors NS3 helicase, ribosome, RIG-I, and $\phi 29$,⁶ inhomogeneities in thin film poly(2-hydroxyethyl acrylate),⁷ dynein and kinesin driven active transport,⁸ and substrate structure and breakdown due to enzymolysis by aPLA1.⁹ In each of these cases, the connection between probe position data and the underlying biophysical phenomena, e.g. switching mechanisms, residence times, and reaction kinetics would be strengthened through comprehensive, qualitative analysis method(s).

Sophisticated tools for analyzing motion have been developed to scrutinize migration of animals,¹⁰⁻¹³ movement of cells and microorganisms¹⁴ and people.¹⁵ Frequently, the

experimentally observed probability distribution function (PDF) or cumulative distribution function (CDF) of displacement is fit to a model such as a power law, an exponential model, or a combination of the two^{14,16-18}. The best fit function allows confinement or flow within a trajectory to be detected by comparing the frequency of long and short steps to that expected from simple Brownian motion. Recently, techniques based on these ideas have been developed in order to distinguish between various types of motion. Typically these methods have been demonstrated on single particles, *e.g.* quantum dots, or simulated datasets, so their applicability to single molecule trajectories needs to be assessed. In this chapter, the range of published methods for single particle motion analysis is evaluated with single molecule-like simulated data and experimental SMT data. The results highlight three methods as most applicable to SMT data: (1) confinement level calculations,¹⁹ (2) time series analysis,²⁰ and (3) statistical analysis of lateral diffusion and multistate kinetics.²¹ A fourth technique, radius of gyration evolution, developed in our laboratories, provides complementary information that is particularly useful in comparing individual and ensemble behavior and is also useful in the analysis of single molecule trajectories.

These four techniques are compared by using them to quantify the movement of a sample of five probe molecules, representative of a larger population within a surface tethered brush phase of poly(N-isopropylacrylamide), pNIPAAm, prepared by grafting-from atom transfer radical polymerization. The goal is to develop a robust set of metrics to characterize individual diffusing probe molecules in order to address the commonly encountered problem where trajectories are relatively short and of different lengths and to address the particular kind of sub-diffusive motion resulting from episodic confinement. In the context of stimulus-responsive materials the resulting SMT trajectory distributions may, thus, be mapped back to distributions

of chemical and physical environments and, in particular, to the dynamic properties of these environments that modulate the translocation properties of the probes.

5.2 Analysis software

All methods have Matlab code available online or freely shared by the authors. Confinement level and time series analysis functions were modified to accept trajectory data from our existing tracking program and experimental apparatus. The statistical analysis of lateral diffusion and multistate kinetics function was modified to accept real trajectories of varying lengths since the software was originally written for simulated data of constant length. Radius of gyration analysis code was written in Matlab.

5.3 Single molecule diffusion simulations

Simulations were carried out in a modified Matlab program based on code originally developed by Coscoy *et al.*¹⁸ The program generates n_walks (number of particles) random walks with trajectories n_steps in length on a Cartesian coordinate system. A Gaussian distribution of step sizes is simulated with mean 0 and variance 0.8, as well as an equal number of random angles. Steps in x - and y -directions for each trajectory are determined from the step size and angle arrays from which positions are calculated based on the user-defined diffusion process and parameters. Gaussian noise with the user-assigned relative amplitude is added after steps are determined. Diffusion coefficients are established by the user, along with exposure time and magnification. The diffusion process can be modified to include noise, convection, zones of confinement, or intermittent regions (phases of slow and fast diffusion).

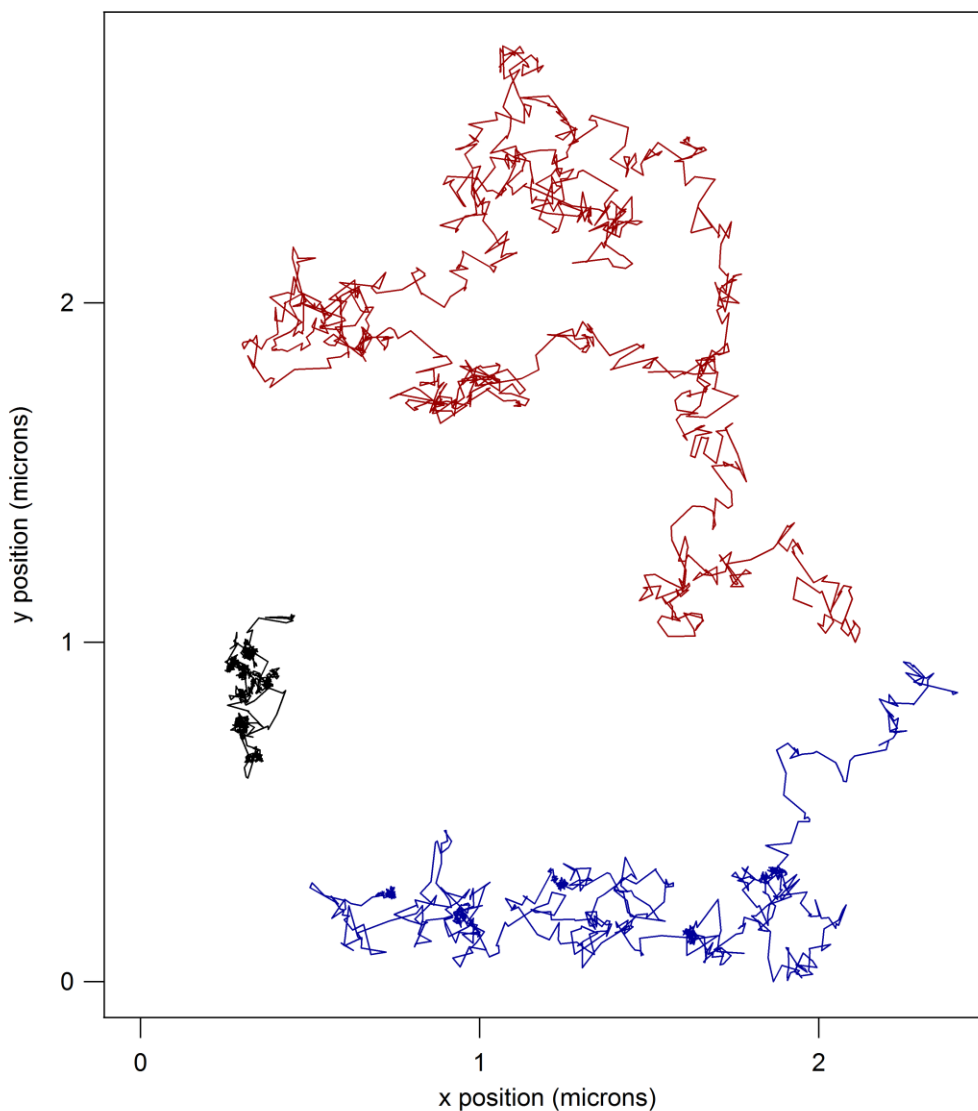


Figure 5.1: Position plots of three single molecule trajectories simulated in *brown_walks.m*.

The red trace is simple diffusion at $D = 1 \mu\text{m}^2/\text{sec}$, the blue trace is intermittent diffusion with 100 fast-100 slow frames alternating at $D_{\text{fast}} = 1 \mu\text{m}^2/\text{sec}$, $D_{\text{slow}} = 0.01 \mu\text{m}^2/\text{sec}$, and the black trace is intermittent diffusion with 10 fast-100 slow frames alternating at $D_{\text{fast}} = 1 \mu\text{m}^2/\text{sec}$, $D_{\text{slow}} = 0.01 \mu\text{m}^2/\text{sec}$. All trajectories are 1000 frames long with 100X magnification, 30 ms exposure, and 0.05 Gaussian noise. Periods of slow diffusion are outlined in orange for the blue trace.

Sample simulated trajectories for simple and intermittent diffusing molecules are shown in Figure 5.1. All trajectories are 1000 frames long with 30 ms exposure, 100X magnification and 0.05 Gaussian noise. Two optical-specific parameters are included in simulations-magnification, used in converting step size from pixels to microns for the tracking software, and exposure, used in the simulation to determine for the step sizes from which position data is calculated. When comparing simple diffusion at $D = 1 \mu\text{m}^2/\text{sec}$ (red) to intermittent diffusion at $D_{\text{fast}} = 1 \mu\text{m}^2/\text{sec}$, $D_{\text{slow}} = 0.01 \mu\text{m}^2/\text{sec}$ (100 fast-100 slow frames (blue); 10 fast-100 slow frames (black)) it is clear that the relative amount of fast diffusion decreases. Relative areas of confinement occur during periods of slower diffusion, as illustrated by the orange circles outlining the five slow periods in the intermittent trajectory. As the fraction of time spent in confinement increases from the red to the blue to the black trajectory, the overall area that the molecule explores decreases.

5.3.1. Intermittent simulations for analysis technique characterization. Four datasets were simulated using *brown_walks.m* for use with the SMT trajectory analysis techniques discussed below. The parameters used - length and number of trajectory, diffusion coefficients, length of confined and free events - were chosen to approximate the properties of the data obtained from single molecule tracking experiments described later in this chapter and in Chapter 6.

#1, 25_25_x100:	25 slow, 25 fast frames at $D_{\text{slow}} = 0.01 \mu\text{m}^2/\text{sec}$, $D_{\text{fast}} = 1 \mu\text{m}^2/\text{sec}$
#2, 25_25_x10:	25 slow, 25 fast frames at $D_{\text{slow}} = 0.1 \mu\text{m}^2/\text{sec}$, $D_{\text{fast}} = 1 \mu\text{m}^2/\text{sec}$
#3, 25_25_x5:	25 slow, 25 fast frames at $D_{\text{slow}} = 0.2 \mu\text{m}^2/\text{sec}$, $D_{\text{fast}} = 1 \mu\text{m}^2/\text{sec}$
#4, 20_5_x10:	20 slow, 5 fast frames at $D_{\text{slow}} = 0.1 \mu\text{m}^2/\text{sec}$, $D_{\text{fast}} = 1 \mu\text{m}^2/\text{sec}$

All movies have 100 trajectories in 100 frames, 30 ms exposures, 100X magnification and 0.05 Gaussian noise. Simulation datasets 1-3 were used to test the limits of the analysis techniques in identifying periods of fast and slow diffusion when the difference between diffusion coefficients is decreased and to test the limits of estimating small diffusion coefficients. Datasets #2 and #4 were used to test the accuracy of the analysis techniques when the period of fast diffusion is decreased. These simulated tracking data were examined using each of the four trajectory analysis methods in succession.

5.4 Trajectory analysis of intermittent simulations

*5.4.1 Radius of gyration evolution and intermittent simulations.*²² The equations here are the same as those used in calculating the radius of gyration of a polymer chain, with the position of the molecule in time substituted for the position of each segment along the chain. Instead of amount of space occupied by a polymer chain, however, the radius of gyration, R_g , of a trajectory describes the amount of space that the molecule explores during its movement, calculated as the root mean square distance from the trajectory's initial center of mass,

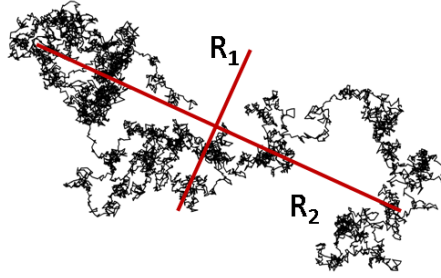
$$R_g = \sqrt{R_1^2 + R_2^2} \quad (5.1)$$

where R_1 and R_2 , illustrated in (5.3), are the major and minor eigenvalues of the radius of gyration tensor, T .

The tensor \mathbf{T} is calculated from the x and y positions of the particle throughout its trajectory,

$$\hat{T} = \begin{pmatrix} \frac{1}{N} \sum_{j=1}^N (x_j - \langle x \rangle)^2 & \frac{1}{N} \sum_{j=1}^N (x_j - \langle x \rangle)(y_j - \langle y \rangle) \\ \frac{1}{N} \sum_{j=1}^N (x_j - \langle x \rangle)(y_j - \langle y \rangle) & \frac{1}{N} \sum_{j=1}^N (y_j - \langle y \rangle)^2 \end{pmatrix} \quad (5.2)$$

where N is the number of steps in the trajectory. Thus, R_g represents the area that a given molecule explores.



However, instead of determining R_g only for the entire trajectory, here R_g is obtained after each step in the track to illustrate how it evolves over time for each molecule. Radius of gyration evolution can then be used to identify intermittent diffusion of molecules and to distinguish this behavior from either consistently immobile or consistently mobile motion, which show very little increase in R_g over time and continuous increase in R_g over time, respectively. The results of R_g evolution for the four simulated intermittent diffusion sets are displayed in Figure 5.2.

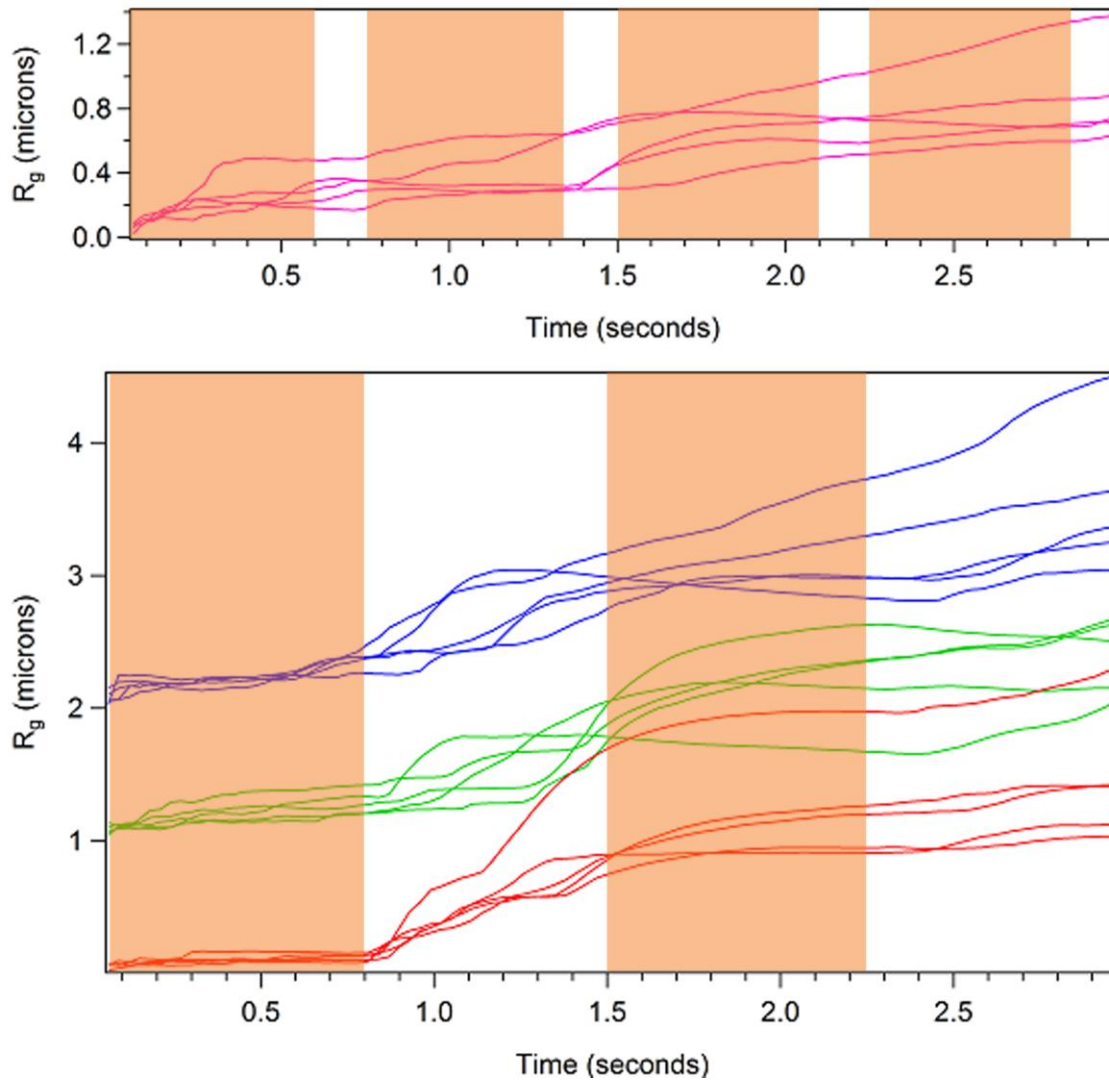


Figure 5.2: Radius of gyration evolution for the first five trajectories each of intermittent simulated diffusion with periods of:

Red	#1: 25 slow, 25 fast frames at $D_{\text{slow}} = 0.01 \mu\text{m}^2/\text{sec}$, $D_{\text{fast}} = 1 \mu\text{m}^2/\text{sec}$
Green	#2: 25 slow, 25 fast frames at $D_{\text{slow}} = 0.1 \mu\text{m}^2/\text{sec}$, $D_{\text{fast}} = 1 \mu\text{m}^2/\text{sec}$
Blue	#3: 25 slow, 25 fast frames at $D_{\text{slow}} = 0.2 \mu\text{m}^2/\text{sec}$, $D_{\text{fast}} = 1 \mu\text{m}^2/\text{sec}$
Fuchsia	#4: 20 slow, 5 fast frames at $D_{\text{slow}} = 0.1 \mu\text{m}^2/\text{sec}$, $D_{\text{fast}} = 1 \mu\text{m}^2/\text{sec}$

All movies have 100 trajectories in 100 frames, 30 ms exposures, and 0.05 Gaussian noise.

Slow periods are highlighted orange for intermittent - 25 slow frames- 25 fast frames (#1-3) and 20 slow frames-5 fast frames (#4).

For intermittent diffusion during periods of relative confinement the slope is close to zero (highlighted orange), while periods of more rapid movement are characterized by greatly increased slopes. In addition, small negative slopes can also be observed when a molecule is confined to a relatively small region after a period of movement, resulting in a decrease in R_g . These differences are most apparent in the 25_25_x100 trace (red), are still visible with the 25_25_x10 trace (green) and decrease to the point of being difficult to detect with the 25_25_x5 trace (blue). The slow periods in the 20_5_x10 trace are equally difficult to detect even though the ratio between diffusion coefficients is 10, which is sufficient for fast-slow differentiation in the 25_25_x10 dataset. These results show that the R_g evolution method can easily detect changes in rate of diffusion if the difference is 100X and can also handle 10X difference when the periods of fast and slow diffusion are long enough. Evolution of R_g can be further quantified by obtaining the 1st and 2nd derivative over time, and by compiling all R_g values or just final R_g values into probability distribution functions.

5.4.2 Confinement level and intermittent simulations.^{19,23} High density multiple particle tracking data yield trajectories that can subsequently be analyzed to detect and quantify the degree of confinement. Serge *et al.*¹⁹ applied this method to 1200 trajectories, averaging ~230 frames, obtained from quantum dot labeled epidermal growth factor receptor in live cells. On an individual particle basis, relative confinement, quantified by L_{conf} , was determined using a method introduced by Meilhac *et al.*²⁴ developed from a previous probability level method.^{25,26} Meilhac *et al.* introduce a delocalized measure of diffusion, which makes the calculation less dependent on random fluctuations and allows comparisons between trajectories:

$$L_{conf} = \frac{D_{\max} w_{conf}}{\text{var}(r)} \quad (5.4)$$

where D_{max} is the unconstrained diffusion coefficient, w_{conf} is the sliding temporal window for calculation, and $\text{var}(r)$ is the variance of displacements from the middle of that window. When $\text{var}(r)$ is larger, L_{conf} is smaller and less relative confinement is measured. A period of confinement is detected only if L stays above the threshold L_{min} for the minimum confined duration t_{min} or longer, with optimized parameters w_{conf} , L_{min} , and t_{min} . As each time point is analyzed for level of confinement, the trajectory is parsed into ‘free’ and ‘confined’ subsections. Segments in these two categories from all trajectories are then grouped together and can be further analyzed for diffusion coefficient, segment duration, area explored per segment, and frequency of confinement. In addition each molecule is labeled with α , the fraction of steps in confinement.

Serge *et al.* found that 4 frames for w_{conf} was sufficiently long to ensure reliable detection yet short enough to detect transient confinement. They also performed an analysis of receiver operating characteristics to determine the ideal lengths for L_{min} and t_{min} that minimize false detections (low PFA_{conf}) and simultaneously maximize identification of true confinement (high PD_{conf}). The global score $\text{PD}_{conf} * (1 - \text{PFA}_{conf})$ was maximized at $L_{min} = 5$ and $t_{min} = 3$ frames which gives 0.78 for PD_{conf} and 0.025 for PFA_{conf} .

The authors tested this algorithm against four model datasets: intermittent slow/fast, permeable domains of confinement, anomalous diffusion with $\langle r^2 \rangle = 4Dt^{0.8}$, and free diffusion. The confined fraction, α_{conf} , showed that the algorithm detects slowdowns and domains better than it detects anomalous diffusion, which exhibits α_{conf} similar to that of free diffusion. They also tested the dependence of the results on exposure time with biological tracking data. When varying exposure times between 36, 20, 10, and 5 milliseconds, the authors found that the diffusion coefficients and radius of confined portions increased slightly, while those of free

portions were unchanged. Duration of confined events, duration of free events, and fraction of confined steps within a trajectory were all independent of exposure time.

When applied to the four intermittent datasets being studied here, the confinement level results definitely show a limit in detecting confinement. Graphs of the confinement index L for the first three trajectories in each dataset are displayed in Figure 5.3 and results for α , D_{free} , and D_{conf} from all confined and free segments are compared to the expected values t_{slow}/t_{total} , D_{fast} , and D_{slow} in Table 5.1. The 25_25_x100 confinement areas are correctly detected, as illustrated by the highlighted orange areas in which L is consistently above $L_{min} = 5$ (horizontal orange line) and by the values of α_{conf} which are near 0.5 as expected, $\alpha_{conf} = 0.55 \pm 0.07$ for all 100 trajectories. Confined regions for 25_25_x10 are detected slightly less accurately, with missing sections within the 25 frame slow periods, although α_{conf} is reasonably close to 0.5, $\alpha_{conf} = 0.42 \pm 0.07$. The accuracy of confinement detection is even lower for 25_25_x5 with many missing sections and $\alpha_{conf} = 0.28 \pm 0.11$. Lastly, the 20_5_x10 trace has some gaps in expected confined areas and $\alpha_{conf} = 0.63 \pm 0.08$ that deviates significantly from the expected 0.8. In terms of diffusion coefficient calculation, most of the datasets shows a slight overestimation in D_{conf} and D_{free} , however all are within a factor of 1.5 of the actual value. The D_{free} found for 20_5_x10 is lower than expected, which is consistent with the misidentified confined steps being grouped with the ‘free’ portions.

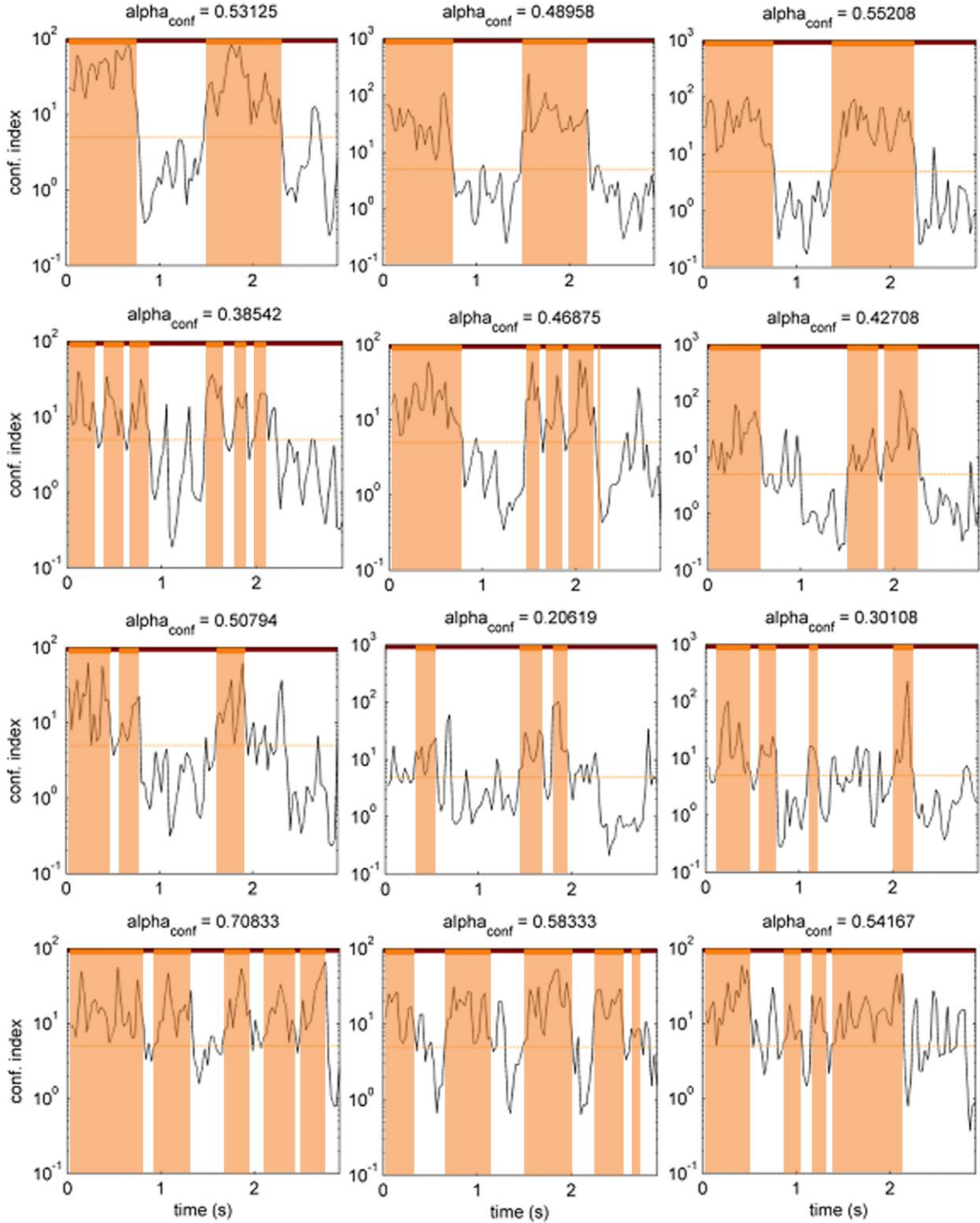


Figure 5.3: Confinement level results for the first three trajectories from simulations #1-4: 25_25_x100 (top row), 25_25_x10 (second row), 25_25_x5 (third row), 5_20_x10 (fourth row). Confinement areas detected in each trajectory are highlighted in orange, the L_{\min} threshold is displayed on each graph at confinement index = 5. The fraction of confined steps, α , is listed above each graph.

Table 5.1: Confinement level results D_{conf} , D_{free} , and α .

Simulation	D_{slow}	D_{fast}	$t_{\text{slow}}/t_{\text{total}}$	D_{conf}	D_{free}	α (mean \pm std)
25_25_x100	0.01	1	0.5	0.03	1.5	0.55 ± 0.07
25_25_x10	0.1	1	0.5	0.13	1.4	0.42 ± 0.07
25_25_x5	0.2	1	0.5	0.2	1.2	0.28 ± 0.11
20_5_x10	0.1	1	0.8	0.15	0.62	0.63 ± 0.08

All calculations were carried out with $D_{\text{global}} = 1000 \cdot \text{timelag}$. Diffusion coefficients, D , are in units of $\mu\text{m}^2/\text{sec}$.

Taken together the results of these confinement level simulations show that the capabilities of intermittent fast-slow detection for confinement level analysis are similar to those of R_g evolution. Differences between fast and slow diffusion below x10 are too small to be detected by confinement level analysis. The fraction of confined steps for x10 datasets is close to the value expected, however the confined events were broken up by missing detections. This would result in shortened duration of confinement and smaller radius of confined zones, which could be important for experiments involving single molecule tracking in a soft material.

*5.4.3 Time series analysis and intermittent simulations.*²⁰ In time series analysis, Ying *et al.* employ two methods on a particle-by-particle basis in order to ascertain what type of diffusion is being exhibited. The first method involves least squares fitting various models of the step size probability distribution function in order to determine if the distribution has excess or fewer long or short steps than a simple Weibull model (which describes Brownian diffusion) would predict. The second analysis method consists of fitting the first ten steps of the MSD vs. τ plot with two linear and two power law models to determine an instantaneous diffusion coefficient. The authors' original paper applied this technique to Class I major histocompatibility complex molecules labeled with 40 nm gold particles imaged at video rate (1/30 sec) to produce tracking

data consisting of 34 gold particle paths with between 623-2,117 steps. They also used simulated trajectories of 10,000 step random walks to test the algorithms.

Time series analysis requires that the data are ergodic- with the statistics of a large number of paths at one time equal to one path evaluated over a long period- and stationary- with mean and standard deviation of a large number of series independent of time. These conditions are not always true, especially for biological experiments with adsorption sites and inhibited diffusion in membranes. An easy way to use this technique on data sets that do not meet these requirements, however, is to parse the data into different types of diffusion and run the subsets separately.

The two models used to fit the step size distributions are labeled general Weibull (GW) and Chi. Least squares fitting of the two models is used to determine if there are more or fewer long or short jumps in the data than expected for unconstrained diffusion (simple Weibull). In general excess short jumps can be seen in a fat head in the distribution and excess long jumps can be seen in a fat tail. To explore the distribution quantitatively, the fit parameters of the model functions can be analyzed:

$$\text{General Weibull:} \quad w(r, k) = kr^{k-1}e^{-r^k} \quad (5.5)$$

$$\text{Chi:} \quad c(r, d) = \frac{2}{2^{d/2}\Gamma(d/2)} r^{d-1} e^{-\frac{r^2}{2}} \quad (5.6)$$

The use of these fit parameters is illustrated by the time series analysis results for the four intermittent simulations, which are displayed in Figure 5.4. The dimensionality, k , from the GW model, reveals if there are an excessive number of short jumps, which is indicated by values in

the range $1 < k < 2$, and can be interpreted as a fractal dimension. When $k = 2$, the GW distribution is a simple Weibull (unconstrained Brownian motion) and when $k = 1$ it is an exponential distribution. All of the intermittent simulations show distributions for k that fall between 1 and 2 (Figure 5.4a). The 25_25_x10 and 25_25_x5 show similar distributions for k , while the distribution for 25_25_x100 is slightly shifted toward 1, which is consistent with the higher degree of confinement from a smaller D_{slow} . Interestingly, the distribution for 20_5_x10 is shifted more strongly toward 2, indicating less constrained motion. This is counterintuitive, given that the fraction of steps in the slower diffusion state is the largest for dataset #4. However, in this case the step size distribution will be dominated by small jumps with a few larger jumps since 80% of the steps are in the slower diffusion state. Therefore, this manifests as an excess number of long jumps in the distribution instead of a paucity of short jumps. However, the GW model only analyzes the leading edge of the function, so it has nothing to say about long jumps.

The chi model offers an interesting insight into the dimensionality of the data. As with k from the GW model, $1 < d < 2$ for excess short jumps. In this case d represents the relative number of nanometer scale obstructions met by a diffusing molecule ($d = 1$ for a line, $d = 2$ for a plane) and therefore the degree of confinement. The results from the Chi model (Figure 5.4b) are consistent with those of k from the general Weibull. Both models of the time series analysis are insensitive to the degree of confinement change between the x10 and x5 data, giving similar limits of detection as the R_g evolution and confinement level analyses.

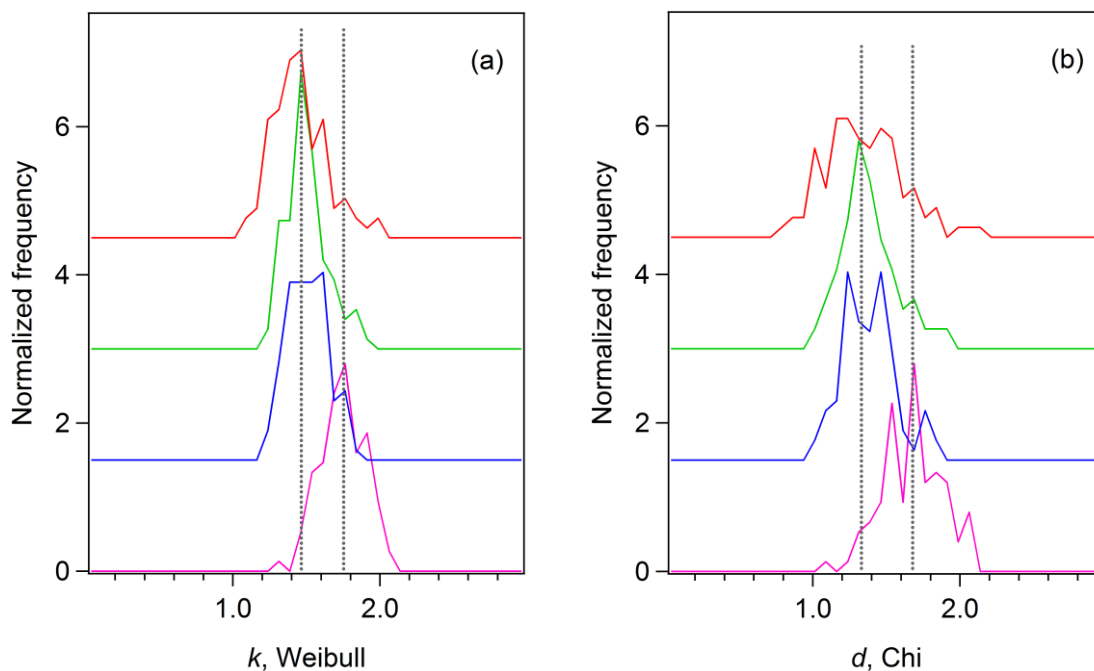


Figure 5.4: Time series analysis results, histograms of the parameters k from general Weibull (panel a) and d from Chi (panel b) for model fitting of step size probability distribution functions of 25_25_x100 (red traces), 25_25_x10 (green traces), 25_25_x5 (blue traces), and 20_5_x10 (fuchsia traces). All model fitting was carried out for step size PDFs compiled with 50 nm bin size. Traces are offset with gray guidelines for clarity.

*5.4.4 Statistical analysis of lateral diffusion and multistate kinetics and intermittent simulations.*²¹ This method was developed by Matsuoka *et al.* for the specific purpose of distinguishing between three distinct types of diffusion. Case 1: molecules exhibiting simple diffusion with a single diffusion coefficient, Case 2: two populations of molecules showing simple diffusion with D_1 and D_2 , respectively, and Case 3: intermittent diffusion in a single population of molecules that switches between D_1 and D_2 with k_{12} and k_{21} . To distinguish among the three cases, functions for diffusion with 1, 2, 3, and 4 states are modeled on the

probability distribution function (PDF) of displacement using maximum likelihood estimation. Since models with more parameters naturally fit the data better, the Akaike information criterion (AIC) is used to determine whether this increase in number of states is legitimate. The AIC value for each function is calculated by:

$$AIC_i = -2l_i(D) + 2k_i, \quad (5.7)$$

where $l_i(D)$ is the log likelihood, a measure of the goodness of fit to the data, and k_i indicates the number of parameters used. The log likelihood increases when differences between the data set and the model decrease. In general, the first term in Equation 5.7 decreases when the number of states in the model increases and the second term acts as a penalty for using more parameters. The model with the most likely number of diffusion coefficients has the lowest AIC value.

Lastly, the autocorrelation function of squared displacement is fit to an exponential function with decay constant K and amplitude a : $y = a * e^{-Kx}$ and used to distinguish Case 2 from Case 3. If the data are derived from molecules that exhibit state transitions between D_1 and D_2 , the autocorrelation function shows an exponential decay. On the other hand, if the data results from molecules that exist in distinct sub-populations with D_1 and D_2 , the autocorrelation function is shaped like a δ -function (a discontinuous decrease).

Despite this very simplified depiction of possible states of diffusion compared to real data, it is still useful to explore how differentiated Cases 1, 2, and 3 can be. Specifically, the limits for the length of trajectories, the number of steps per trajectories, diffusion coefficients, ratio of diffusion coefficients, exposure times, and fractions of populations can be determined. Simulations carried out by Matsuoka *et al.*²¹ to establish cutoffs for the amount and type of data

needed in various cases are summarized here to illustrate the general principles and how they are reflected in the analysis of specific molecular behavior.

For Case 1, simple diffusion in 100 molecules with 300 time points was simulated at $D = 2 \mu\text{m}^2/\text{sec}$. From the accuracy of D_{est} , the authors deemed this number of trajectories and time points sufficient to estimate the diffusion coefficient correctly, although as few as 10 trajectories yield an extremely good estimate- $D_{est} = 1.95\text{-}2.05 \mu\text{m}^2/\text{sec}$. Using this length of trajectory at 30 ms exposures, a movie of 300 time points corresponds to 10 seconds of illumination time, which is easily achievable with many fluorophores.²⁷⁻³⁰

For Case 2, simulations were run with 300 time points and $D_1 = 0.01 \mu\text{m}^2/\text{sec}$, $D_2 = 0.05 \mu\text{m}^2/\text{sec}$, $p = 0.75$ (fraction of the population at D_1), and exposure = 33 ms. Datasets with 10-1000 trajectories were used to test the dependence of diffusion coefficient and fraction of population on the number of trajectories. The authors found that the fraction of the population estimation is much more sensitive to the number of trajectories in the dataset, with ~100 trajectories needed to estimate diffusion coefficients and 200 trajectories needed to estimate fraction of the population accurately.

Simulation of Case 3 with $D_1 = 0.05 \mu\text{m}^2/\text{sec}$, $D_2 = 0.3 \mu\text{m}^2/\text{sec}$, $k_{12} = 20$, and $k_{21} = 5$ for 100 trajectories with 300 time points was used to establish guidelines and limits for data analysis. First, three displacement PDFs were calculated with $\Delta t = 0.5, 0.05$, and 0.005 . From this comparison, Matsuoka *et al.* found that at high temporal resolution ($\Delta t = 0.005$) the PDF shows two distinct peaks for steps at D_1 and steps at D_2 , while at low temporal resolution ($\Delta t = 0.5$) the PDF exhibits time averaged behavior and approaches the same profile as model 1 with D_{eff} equal to a linear combination of D_1 and D_2 . Second, the authors found that in order to use the autocorrelation function to distinguish Case 3 from Case 2 the time interval for measurements

must be longer than the characteristic time of the state transition by a sufficient amount. On the other hand, to distinguish Case 3 from Case 1 the temporal resolution of the autocorrelation function must be shorter than the characteristic time of the state transition. For this simulated data set, the optimal Δt was between 10^{-2} and 10^{-4} sec. Higher resolution is needed when the difference between D_1 and D_2 decreases, with the limit $D_2 \sim 5D_1$, beyond which resolution could not be achieved.

Another Case 3 simulation was run with trajectories containing 300 time points, $D_1 = 0.01 \mu\text{m}^2/\text{sec}$, $D_2 = 0.05 \mu\text{m}^2/\text{sec}$, $k_{12} = 1 \text{ Hz}$, $k_{21} = 3 \text{ Hz}$, and exposure = 33 ms. Datasets with 100-1000 trajectories were used to test the dependence of D_1 , D_2 , k_{12} , and k_{21} on the number of trajectories. As with Case 2, the diffusion coefficients were less sensitive than the transition rate constants and 100 trajectories were sufficient to estimate diffusion coefficients, while ~500 trajectories were necessary to accurately approximate transition rates.

In summary, to identify the number of states and quantify diffusion coefficients and fractions of subpopulations correctly, the data should satisfy three criteria: (1) $D_{fast} \geq 5D_{slow}$, (2) the time interval for measurements must be longer than the characteristic time of the state transition in order to differentiate between the Case 2 and Case 3, and (3) 100-200 trajectories with 300 time points are necessary to have accuracy within 10%. However, fewer data points can be used (as few as 40 trajectories with 300 time points or roughly 10000 total steps) to estimate diffusion coefficients and population fractions if accuracy within 50% is acceptable.

With these guidelines in mind, this statistical analysis method was applied to the same four simulated intermittent datasets that were used previously, details in Section 5.3.1. Displayed in Figure 5.5, step size PDF fitting with 1, 2, 3, and 4 states (column (a)) and AIC calculations (column (b)) determined that two states were needed for all four datasets, as

expected. The autocorrelation function of squared displacement (column (c)) was determined and showed a significant correlation at certain lag times as expected from the regular spacing of fast and slow periods. However, the fitting of this function failed in all cases and illustrated neither a δ -function nor an exponential decrease. This is probably because of the regular spacing of intermittent periods and the small number of switches over the course of a trajectory, which was not encountered with experimental data discussed in later in this chapter and in Chapter 6.

Estimates for diffusion coefficient and fraction of population from the PDF fitting of 1, 2, 3, and 4 states are reported in Tables 5.2-5.5. Focusing on the 2-state solutions, the diffusion coefficients are consistently overestimated, by at least 2X, with the slowest states up to 10X too high. However the fraction of population estimates are still close to the expected values (0.5 for 25_25 and 0.8 for 20_5). The fractions for 20_5_x10 are especially good, much better than the estimate from confinement level analysis. It is also interesting to note that as the ratio between D_{fast} and D_{slow} decreases, the estimates actually get closer to the expected values. Considering that the experimental data to be analyzed later in this chapter and in Chapter 6 have D_{fast} and D_{slow} close to those in simulation #1, some overestimation of the slower diffusion coefficient can be expected, but this analysis method permits the two states to be readily distinguished, if the noise in position is similar to that used in these simulations.

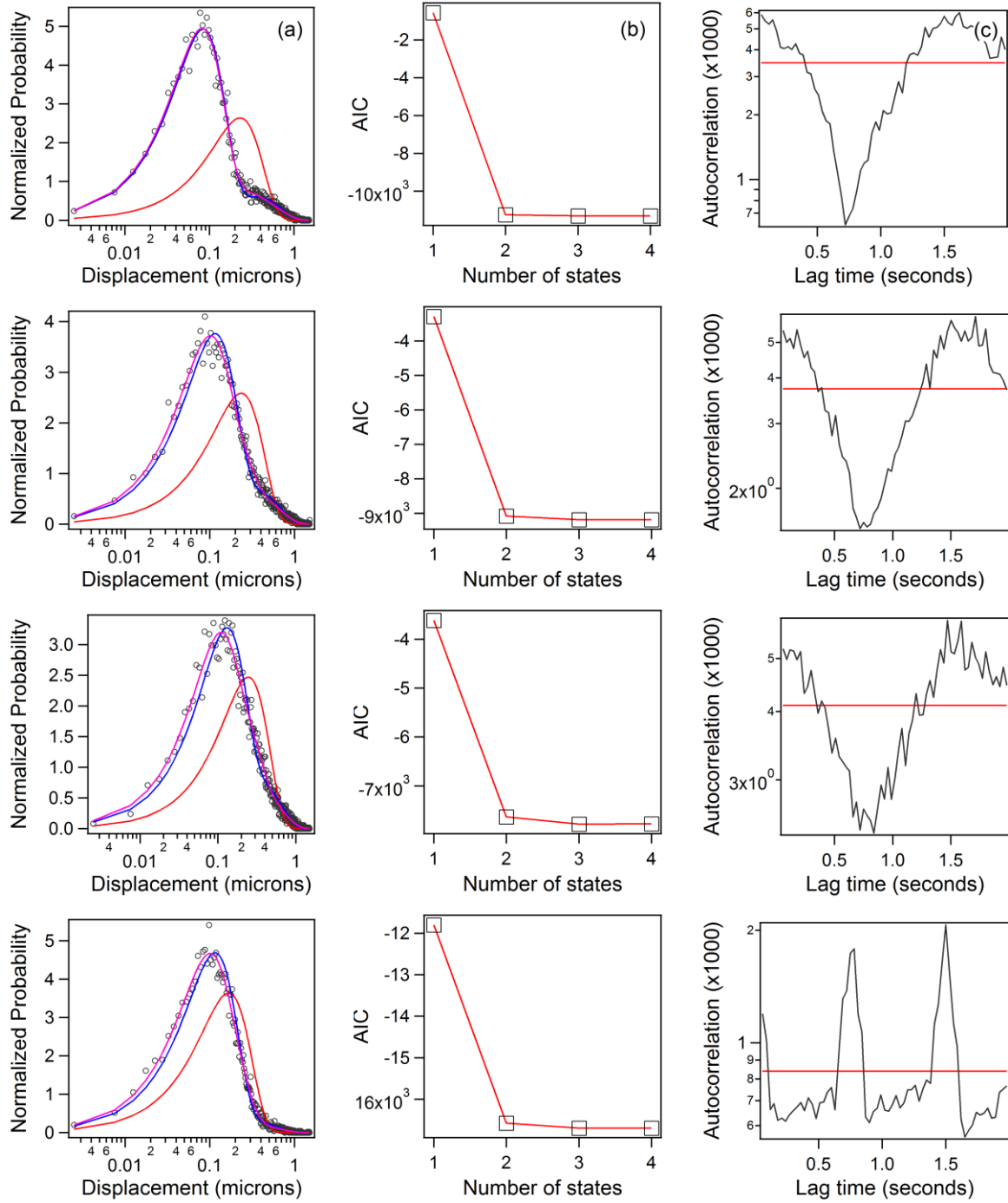


Figure 5.5: Statistical analysis of lateral diffusion and multistate kinetics results showing displacement PDFs (black circles) with least squares fits for 1 state (red), 2 states (blue), 3 states (fuchsia), and 4 states (not shown) in column (a), the Akaike information criterion results (black squares with red guide line) in column (b), and the squared displacement autocorrelation functions (black line) and fits (red line) in column (c). Four simulations are included: #1: 25_25_x100 (top row), #2: 25_25_x10 (second row), #3: 25_25_x5 (third row), and #4: 5_20_x10 (fourth row).

Table 5.2: #1: 25_25_x100 ($D_{slow} = 0.01$, $D_{fast} = 1$, $x_{slow} = 0.5$)

	1 state	2 states	3 states	4 states
D ₁	0.90	0.11 (0.64)	0.71 (0.13)	2.63 (0.28)
D ₂	---	2.24 (0.36)	0.10 (0.60)	18.84 (0)
D ₃	---	---	2.63 (0.28)	0.10 (0.60)
D ₄	---	---	---	0.71 (0.13)

Table 5.3: #2: 25_25_x10 ($D_{slow} = 0.1$, $D_{fast} = 1$, $x_{slow} = 0.5$)

	1 state	2 states	3 states	4 states
D ₁	0.90	0.17 (0.63)	0.40 (0.35)	0.04 (0.14)
D ₂	---	2.10 (0.39)	0.09 (0.36)	2.60 (0.25)
D ₃	---	---	2.43 (0.29)	0.19 (0.43)
D ₄	---	---	---	0.77 (0.19)

Table 5.4: #4: 25_25_x5 ($D_{slow} = 0.5$, $D_{fast} = 1$, $x_{slow} = 0.5$)

	1 state	2 states	3 states	4 states
D ₁	0.97	0.22 (0.59)	2.50 (0.29)	0.10 (0.28)
D ₂	---	2.04 (0.41)	0.10 (0.28)	15.13 (0)
D ₃	---	---	0.52 (0.43)	0.52 (0.43)
D ₄	---	---	---	2.50 (0.29)

Table 5.5: #4: 5_20_x10 ($D_{slow} = 0.1$, $D_{fast} = 1$, $x_{slow} = 0.8$)

	1 state	2 states	3 states	4 states
D ₁	0.36	0.12 (0.85)	0.02 (0.37)	0 (0.25)
D ₂	---	1.79 (0.15)	0.24 (0.53)	2.47 (0.08)
D ₃	---	---	2.26 (0.10)	0.17 (0.58)
D ₄	---	---	---	0.66 (0.09)

Tables 5.2-5.5: Statistical analysis of lateral diffusion and multistate kinetics diffusion coefficients and fractions results for the four intermittent motion simulations. Diffusion coefficients, D , are in units of $\mu\text{m}^2/\text{sec}$ and the fraction of population at each D is listed next to it in parentheses.

5.5 *Experimental single molecule tracking data*

Trajectories of five representative molecules of the carbocyanine dye 1,1'-dioctadecyl-3,3,3',3'-tetramethylindocarbocyanine, DiIC₁₈, were sampled from a larger set acquired at 300K in poly(N-isopropylacrylamide), pNIPAAm. The polymer brush was synthesized and prepared for single molecule tracking experiments as described in Section 3.1.2. The data was acquired in collaboration with Moussa Barhoum and Prof. Joel Harris, researchers at the University of Utah, on a 532 nm excitation TIRF microscope,²² analogous to the one described in Section 4.1. These trajectories, which form the basis for the comparative analysis carried out here, are 42, 275, 150, 156, and 80 frames long, respectively, and show periods of obvious confinement, *viz.* Figure 5.6. Molecules 1 and 5 have no gaps or repeats, 2 and 3 have sections where trajectories were spliced together after splitting, and molecule 4 has a gap from blinking.

5.5.1 Data acquisition. Single fluorescent DiIC₁₈ molecules in pNIPAAm were used as the fluorescent probe and target media, and each frame was acquired with a 30 ms exposure using frame transfer so that there was no delay time between frames. Optimum laser power was determined by matching the turn-over rate, when saturation of the fluorophore is reached and SNR is maximized.³¹ Single molecule fluorescence collection parameters - exposure time, detector pre-amp and electron multiplication gain - were optimized in order to achieve a SNR of at least 10, which is especially important in single molecule tracking experiments to achieve accurate localization.³² Data were acquired from videos consisting of 1000 frames with 60X magnification, *i.e.* 267 nm² effective pixel size, which were obtained at 25°C with water as the solvent.

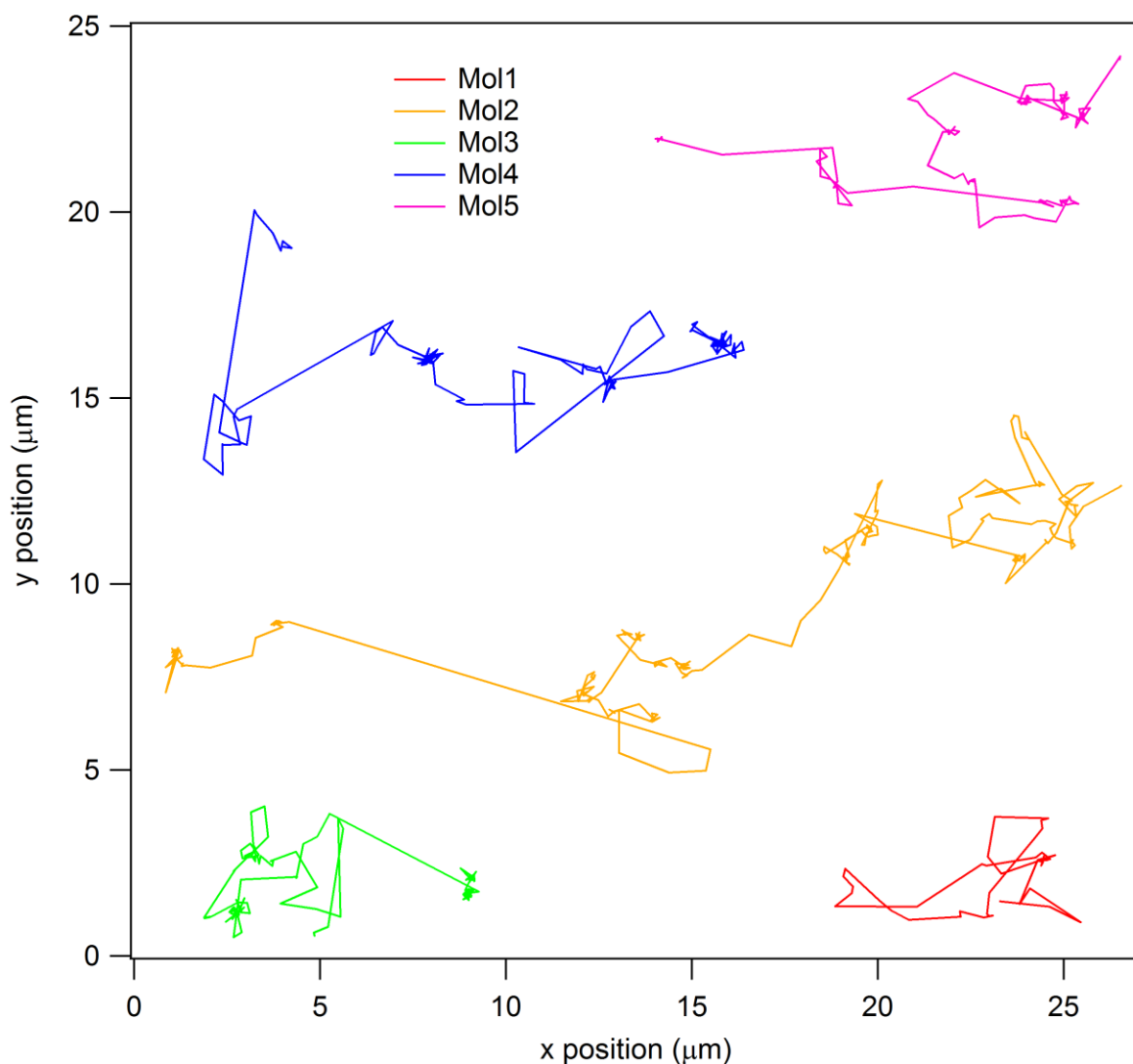


Figure 5.6: Experimental single molecule trajectories from Molecules 1-5

5.5.2 Tracking method. Single molecule tracking was carried out by first identifying a single fluorescent spot on a given frame. The spatial intensity of the spot was fit to a 2D-Gaussian profile, and the center (x_0, y_0) of the fit used to track the trajectory on succeeding frames. The localization uncertainty was determined by imaging a sample of dry (immobile) DiIC₁₈ molecules on a coverslip, with the uncertainty given by the standard deviation of the (x_0, y_0)

positions, which were ≤ 50 nm in all cases, position plot of an adsorbed DiIC₁₈ molecule displayed in Figure 6.3.

5.6 Trajectory analysis of experimental data.

The full analysis of these five sample trajectories was carried out in a step-by-step process that includes preliminary determination of the ensemble and individual mean squared displacement. After the order of magnitude of step sizes was found, these values were used to apply of the radius of gyration evolution, confinement level, time series analysis, and statistical analysis of lateral diffusion and multistate kinetics methods to the data.

5.6.1 Ensemble MSD- τ with experimental SMT data. The most straightforward analysis that can be performed on SMT data compares the ensemble-average MSD to time delay, as shown in Figure 5.7. To estimate the microdiffusion coefficient, the first fifteen points of the MSD vs. τ plot from all five trajectories were used, and weighted linear least squares was used to find the best fit to the equation for 2-dimensional diffusion,

$$\langle x^2 \rangle = 4D\tau + 4\sigma^2 \quad (5.8)$$

which for the particular data of Figure 5.7 gives $D_{ensemble} = 0.386 \pm 0.013 \mu\text{m}^2 \text{ s}^{-1}$. Although crude, this initial ensemble-average D value provides a valuable estimate of the magnitudes to be expected in the rest of the analyses, thereby allowing thresholds, initial inputs, and parameters for the methods detailed herein to be adjusted with some *a priori* knowledge.

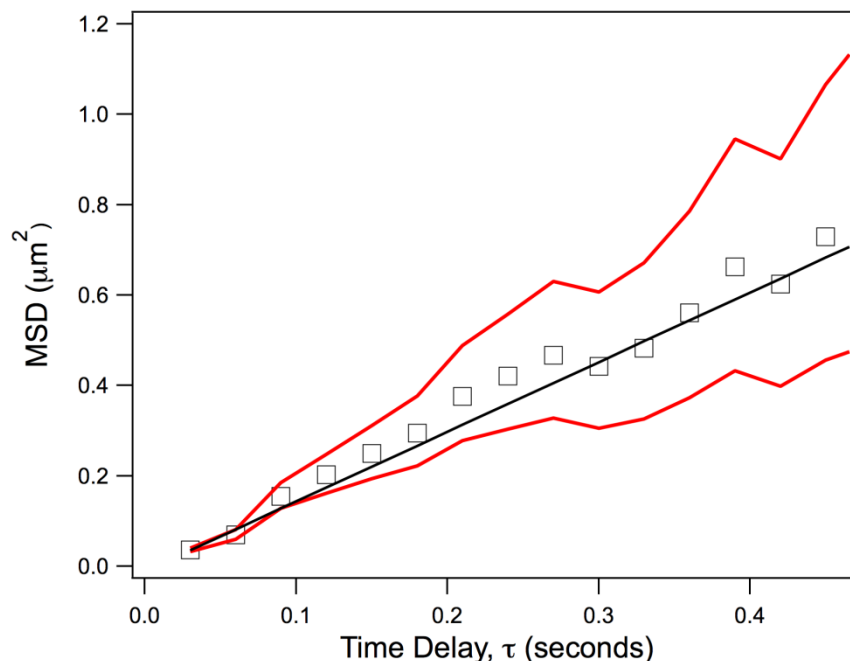


Figure 5.7: Determination of ensemble-averaged microdiffusion coefficient with Molecules 1-5. Black squares are experimental data and solid black line is linear fit, the slope of which is used to calculate $D_{ensemble}$ using equation (8). Solid red lines denote 95% confidence

5.6.2 Individual MSD- τ with experimental SMT data. The same analysis can be applied to individual molecule trajectories, and the results of individual microdiffusion coefficients for Molecules 1-5 are shown in Table 5.6. The MSD- τ slopes, and therefore the trajectory averaged diffusion coefficients, D_{ind} , found by applying this method to the first 15 points in the relevant trajectories have relatively small spread, with D_{ind} varying ~ 5 -fold among the individual molecules. These individual diffusion coefficients, ranging from 0.181 to 0.655 $\mu\text{m}^2 \text{s}^{-1}$, illustrate the magnitude of the variation within the data, and the error shows that the diffusion coefficients can be determined to $<10\%$ RSD in all cases, so the internal consistency of the approach is quite good. However, because both ensemble and individual D values average over trajectories, they necessarily miss internal structure. Thus, methods are needed that are capable

of analyzing changes that occur within trajectories, such as the intermittent fast-slow diffusion that is apparent in the position plots in Figure 5.6.

Table 5.6: Individual diffusion coefficients.

Molecules	Steps	D ($\mu\text{m}^2 \text{s}^{-1}$)
1	41	0.440 ± 0.039
2	273	0.385 ± 0.033
3	149	0.181 ± 0.003
4	154	0.305 ± 0.005
5	79	0.655 ± 0.017

5.6.3 Radius of gyration evolution with experimental SMT data. The most striking feature of the R_g evolution plots, Figure 5.8, is the variation over time within and among trajectories. For example, Molecules 3 and 5 both explore $\sim 0.8 \mu\text{m}$ but go about it in very different ways. Over a total of 4.5 s, Molecule 3 shows confined behavior for periods of ~ 1.5 and 3 s which are separated by a quick burst of movement, while Molecule 5 undergoes four transitions between fast and slow behavior in a total of 2.5 s. Trajectories of simulated simple diffusion with $D = 0.01 \mu\text{m}^2\text{s}^{-1}$ are included in the plot, which is the order of magnitude found for confined portions of the experimental trajectories in the confinement level calculations below. Comparison of simulated and experimental data clearly demonstrates the intermittent diffusive nature of Molecules 1-5 and shows what simple diffusion looks like in the R_g evolution analysis.

In addition to illustrating the intermittent nature of the motion, both qualitative and quantitative information can be gleaned from the R_g evolution. First, it is apparent from the traces that more time is spent in confined states than in mobile states and that nearly all of the increase in R_g occurs during the relatively brief mobile periods. The change in R_g over confined segments can be as small as $0.05 \mu\text{m}$. Highlighting this discrepancy, Molecules 3 has a

trajectory that lasts ~ 4 s, but nearly all of its expansion in R_g occurs over a brief period of 0.5 s between 1.6 and 2.1 s. In contrast over a maximum trajectory length of 8 s Molecule 2 covers over $2 \mu\text{m}$ in a much more homogeneous fashion, exploring on average $\sim 0.25 \mu\text{m s}^{-1}$.

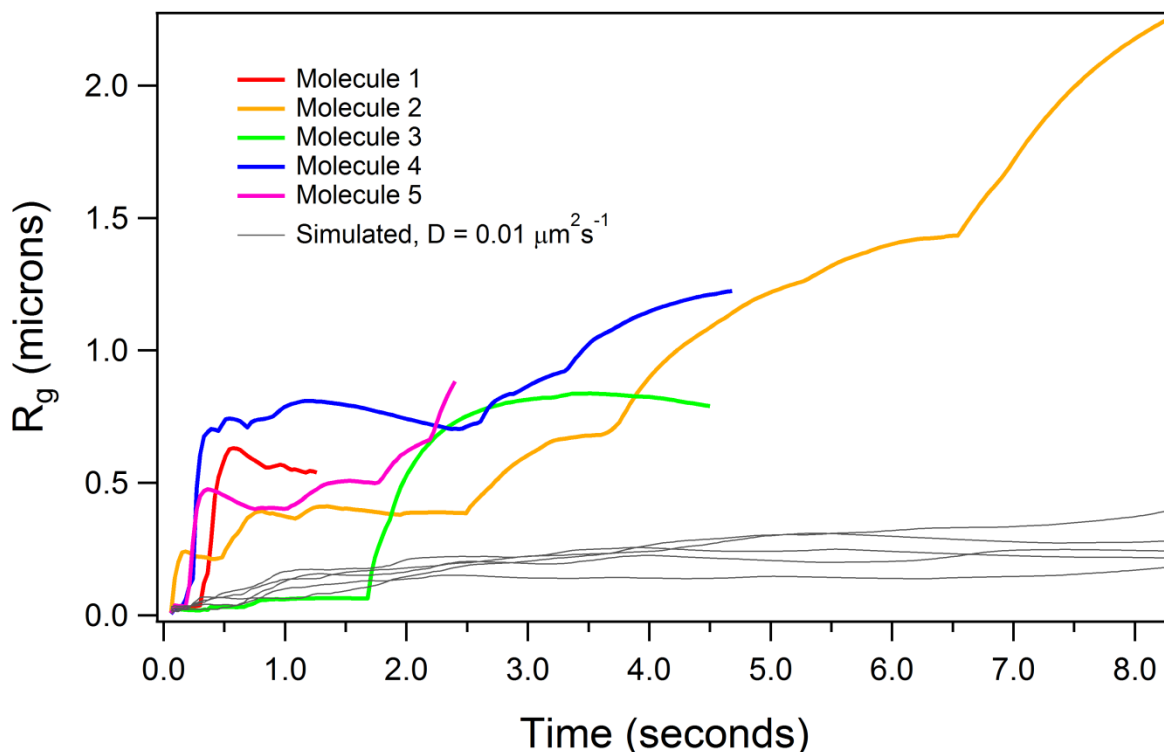


Figure 5.8: Radius of gyration evolution for Molecules 1-5 and five simulated trajectories at $D = 0.01 \mu\text{m}^2 \text{s}^{-1}$ (gray), the order of magnitude found for slow diffusion in the experimental trajectories.

5.6.4 Confinement level analysis with experimental SMT data. Confinement level calculations were carried out for each of the five sample trajectories, with the results for Molecule 4 shown in Figure 5.9 and the results for the remaining molecules shown in Figs. A1.1-A1.4. Figure 5.9a shows the log of confinement index, L , as a function of time. Figure 5.9b shows the log of instantaneous diffusion coefficient, D_{inst} , which is calculated by linear regression of MSD v. τ over each calculation window. As expected $\log(D_{inst})$ drops in periods (highlighted orange)

when the trajectory is confined. Table 5.7 lists the fraction of confinement, α_{conf} , for all molecules. Consistent with the variations in the R_g evolution in Figure 5.8, it is apparent that the fraction of time each molecule spends being confined varies widely from molecule to molecule.

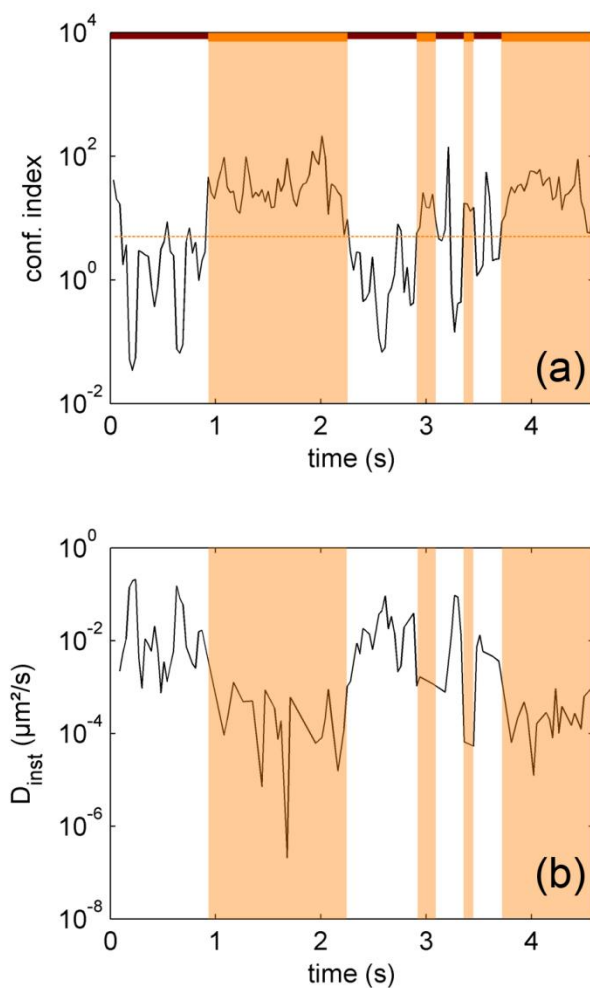


Figure 5.9: Confinement level results for Molecule 4. (a) The confinement level, L , throughout the trajectory. ‘Confined’ periods, when L exceeds the indicated minimum confinement level L_{min} , are shaded orange. (b) Plot of the log instantaneous diffusion coefficient as a function of time.

Table 5.7: Fraction of confinement.

Molecule	α_{conf}
1	0.16
2	0.56
3	0.80
4	0.67
5	0.58

One interesting and useful feature of this protocol is that the confined and free portions found by the confinement calculation can be grouped together and the resulting MSDs plotted separately, as in Figure 5.10. The microdiffusion coefficients obtained from the slopes of the best fit line for the first 10 points of the resulting plots are $D_{\text{conf}} = 0.0124 \mu\text{m}^2/\text{sec}$ and $D_{\text{free}} = 0.81 \mu\text{m}^2/\text{sec}$. A simple calculation finds that 61% of the steps over all five molecules are in the ‘confined’ state and the remaining 39% are in the ‘free’ state. The magnitude of D_{conf} and D_{free} are in the range (100X with $D_{\text{slow}} = 0.01 \mu\text{m}^2/\text{sec}$, $D_{\text{fast}} = 1 \mu\text{m}^2/\text{sec}$) for which detection of confined portions can be performed with high confidence.

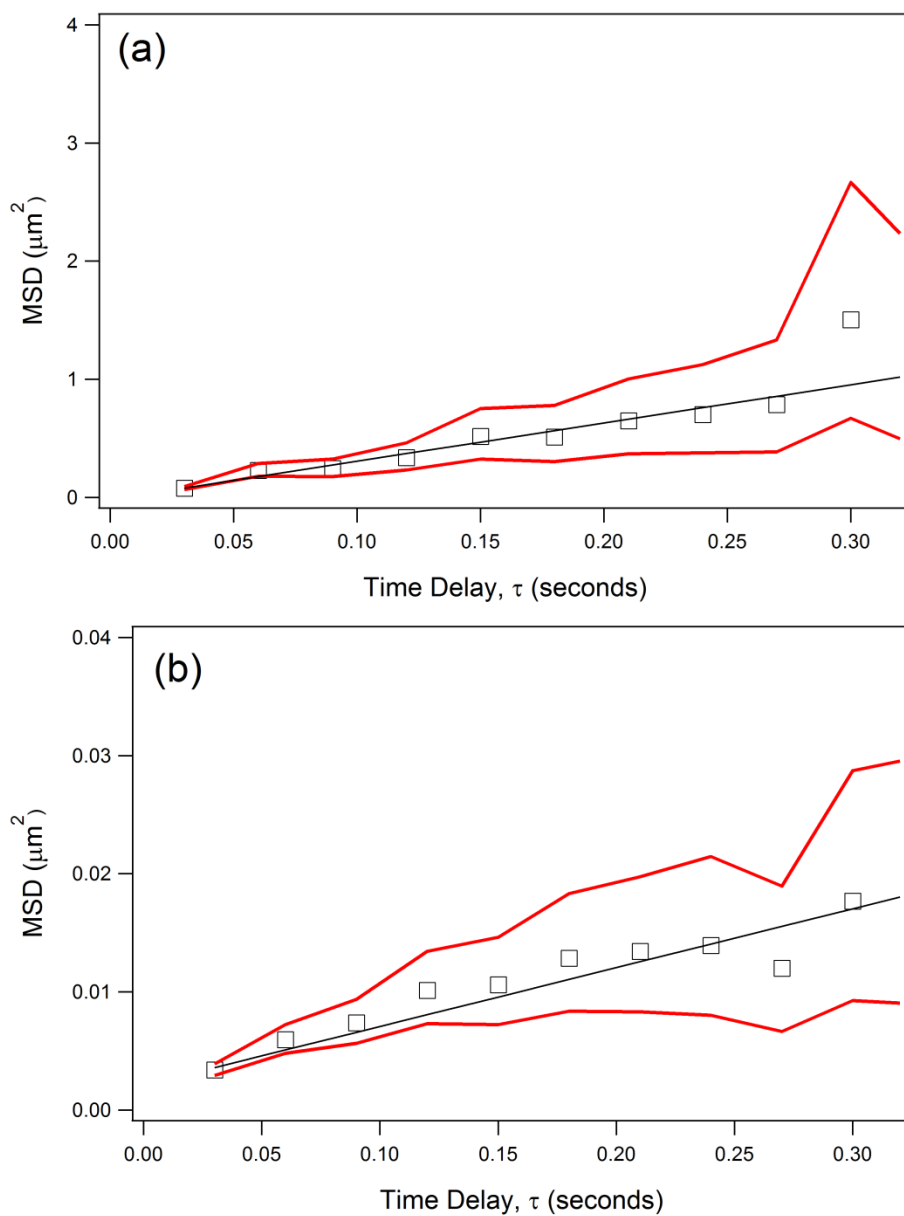


Figure 5.10: Ensemble averaged determination of the diffusion coefficient for the confined (a) and free (b) portions of the trajectories for Molecules 1-5. Note the difference ordinate scales.

Several other conclusions can be drawn from the confinement level calculations. Plots for the probability distribution functions of duration and radius for free and confined events, as

shown in Figure 5.11, show interesting contrasts between the slow and fast periods of motion. Consistent with the assertions based on the R_g data in Figure 5.8, free events last between 0.060 and 0.960 seconds (mean 0.292 sec), while confined events last between 0.090 and 1.560 seconds (mean 0.411 sec). The radius of the area explored for free events is between 1.42×10^{-4} and $0.77 \mu\text{m}$ (mean $0.15 \mu\text{m}$), while confined events explore between 3.63×10^{-4} and $0.0178 \mu\text{m}$ (mean $0.0048 \mu\text{m}$). Given the resolution of the feature finding localization is $\sim 0.04 \mu\text{m}$, the data, even from this very limited test set of trajectories, are easily precise enough for the confinement level calculations to separate confined and free periods.

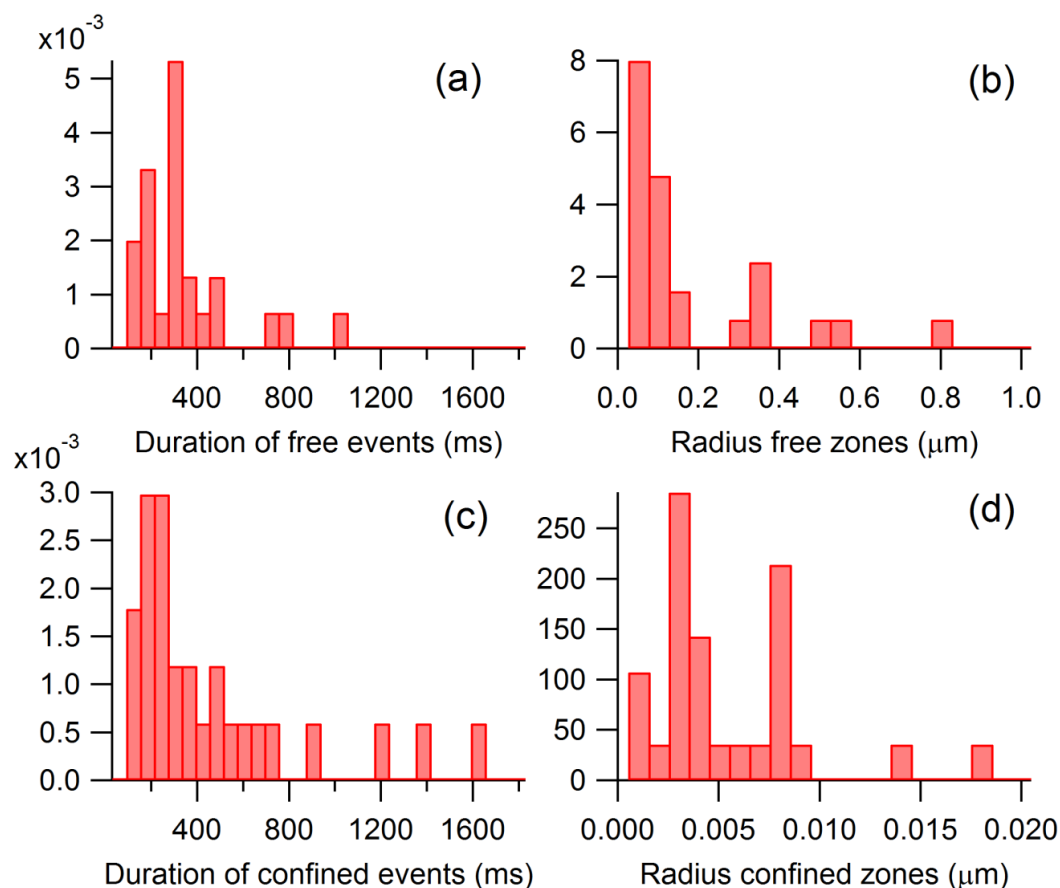


Figure 5.11: Data from confinement level calculations. Histograms for (a) duration of ‘free’ events, (b) radius of ‘free’ zones, (c) duration of ‘confined’ events, and (d) radius of ‘confined’ zones, each normalized to unit total area.

5.6.5 Time series analysis with experimental SMT data. The time series analysis for Molecule 4 is shown in Figure 5.12, results for the rest of the molecules are shown in Figs. A1.5-A1.8, and the results for all molecules are given in Table 5.8. The data in Figure 5.12a determine whether the first ten points of MSD vs. τ are best fit by a linear or a power law function, parameters and residuals being reported in Table A1.1. The residuals from the least squares fits are then used to obtain the parameters for each of the fit functions, and the resulting diffusion coefficients are reported in Table 5.8. Also reported are two additional measures of the heteroscedasticity of the

trajectory. All of the molecules examined here show $k < 2$ (general Weibull) and $d < 2$ (chi), consistent with an excess of short jumps compared to Brownian motion in both models.

Table 5.8: Time series analysis.

Molecule	D ($\mu\text{m}^2 \text{s}^{-1}$) ^a	α ^b	k , GW ^c	d , chi
1	0.61	1.1535	1.2	1.1
2	0.38	1.0464	1.6	1.6
3	0.12	0.9404	1.5	1.3
4	0.45	0.8616	1.5	1.4
5	1.08	0.7499	1.4	1.3

^a D is the individual diffusion coefficient

^b α is the exponent in the MSD v. τ power law fits.

^c k is the dimensionality from the GW fit of the step size distribution
and d is the same for the chi fit

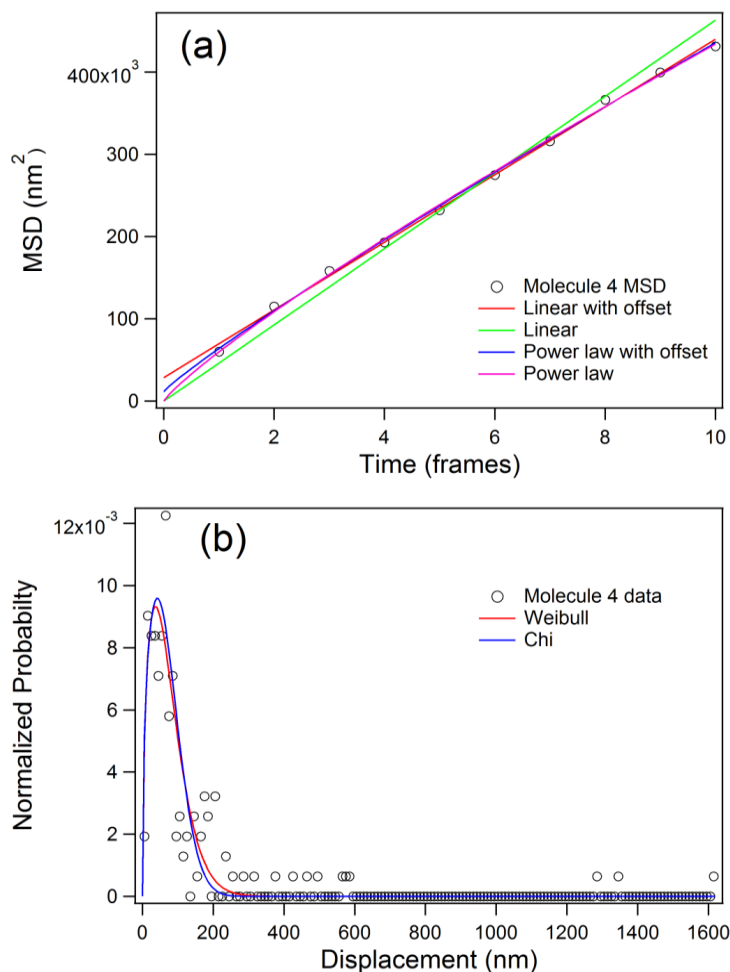


Figure 5.12: (a) Plot of the MSD v. time delay for the trajectory of Molecule 4 over the first ten time delays with best fit traces for two linear and two power law functions. (b) The probability distribution function (histogram) of step size for Molecule 4 with maximum likelihood determined fits for general Weibull and Chi value models.

5.6.6 Statistical analysis of lateral diffusion and multistate kinetics with experimental SMT data. Statistical analysis of lateral diffusion and multistate kinetics leads the user through a decision making process in order to determine the diffusion coefficients, fraction of population, and presence of state transitions, as shown in Figure 5.13. From the fit of the ensemble-average

MSD *vs.* τ , the effective diffusion coefficient of the data (all five molecules) is determined to be $0.47 \mu\text{m}^2/\text{sec}$. In the displacement PDF a large difference exists between the fits of 1 and 2 states, while only an incremental improvement is obtained for the fits of 3 states *vs.* 2 states in Fig 5.13b. Using the results from MSD *vs.* τ and the PDF fits for 1-4 states, data for diffusion coefficient(s) and fraction of states are obtained for each case and reported in Table A1.2. The fits of step size distribution and number of states are then fed into an Akaike information criterion determination (Figure 5.13c), which suggests that a two state solution best describes these data. Note that although the AIC value decreases slightly going from 2 to 3 states, the diffusion coefficients and fraction of each population for 2 states match with corresponding results from confinement level analysis. Therefore, a 2-state model was picked as the best description of this system. In addition, the AIC analysis of the intermittent simulated data with two known diffusion coefficients and known population fractions exhibiting these dynamics, gave similar results (*cf.* Figure 5.5). Thus the smallest number of states producing an AIC value statistically indistinguishable from the absolute minimum, instead of the lowest AIC value, can be chosen. The two states determined in this manner have diffusion coefficients $D_1 = 0.024 \mu\text{m}^2/\text{sec}$ and $D_2 = 1.74 \mu\text{m}^2/\text{sec}$ with 77% of the steps in state 1. Finally, the autocorrelation function is not a δ -function, which confirms that there are state transitions between diffusion coefficients. The results from the statistical analysis confirm what is seen qualitatively in the plots of trajectories in Figure 5.6- that there are sections of higher and lower confinement for each molecule – thereby lending credence to the two-state model obtained from the AIC analysis. This method is especially strong when paired with the confinement level calculations, because the same multiple diffusion coefficients and subpopulation fractions are determined independently.

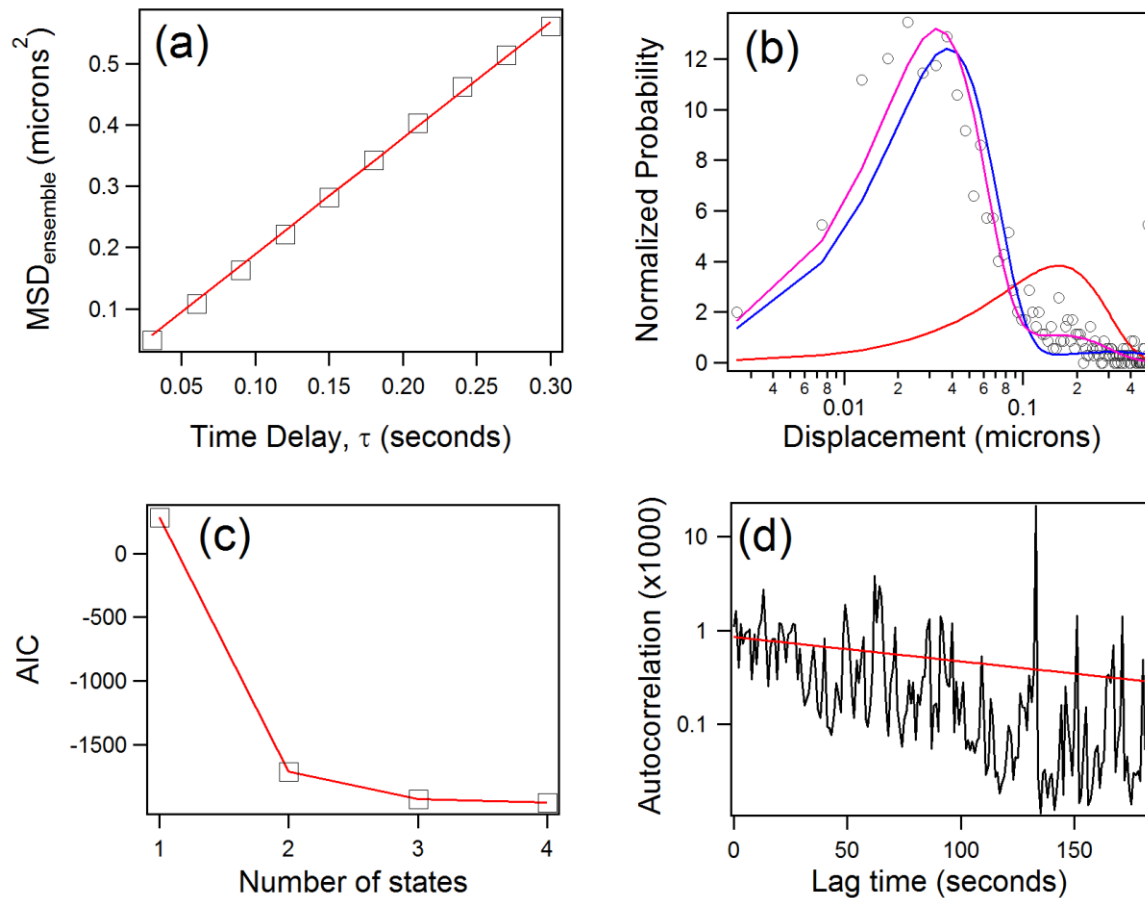


Figure 5.13: Statistical analysis of lateral diffusion and multistate kinetics results. (a)

Ensemble averaged microdiffusion coefficient determination. (b) Step size distribution for the ensemble fit by maximum likelihood estimate for functions with 1, 2, 3, and 4 diffusion states. (c) Akaike information criterion plot showing the most likely number of states. (d) Autocorrelation function of step size with exponential fit function.

5.6.7 Comparison of SMT analysis models with experimental data. Examining the five sample trajectories allows the four SMT data analysis models to be compared side-by-side, as shown succinctly in Figure 5.14. Confinement level, time series analysis, and multistate kinetics

models had previously been described,¹⁹⁻²¹ while radius of gyration evolution is introduced here.²² Figure 5.8, which presents R_g vs. time, visually highlights the staccato nature of mobile-immobile transitions at the single molecule level. Periods of relative immobility are characterized by small slope regions, while mobile periods exhibit much larger slopes. Of course, it is also possible to highlight the transitions between mobility states by plotting derivatives, dR_g/dt (not shown). In addition, the R_g evolution analysis also permits quantitative indicators of the motion to be assessed. For this limited set of sample molecules, periods of confinement were found to last between 0.05 and 3 s, while periods of motion were observed to last between 0.5 and 3 s. R_g over confined regions can be as small as 0.05 μm and overall, the molecules explore $\sim 0.2 \mu\text{m s}^{-1}$. Finally, the R_g evolution promises to extend the utility of previous approaches to the study of single molecule dynamics in network polymers, *e.g.* fluorescence correlation coupled with a small number of short trajectories,³³ single molecule tracking of tagged polyelectrolytes^{34,35} and collapsing single molecule data trajectories to single number descriptors, such as diffusion coefficients.³⁶ Analyzing trajectory data through robust statistical tools, such as the R_g vs. time plots, utilized here allows both ensemble behavior and single molecule deviations from the average to be assessed from a single plot.

Confinement level calculations are consistent with, and build on, the R_g evolution analysis. In particular, this method permits the fraction of steps in confinement to be determined individually and the duration of confined/free trajectory segments grouped over all of the molecules to be measured. For example, the set of molecules studied here exhibits a confined step fraction of 0.16-0.80, with confined segments lasting 0.41 s and free events 0.29 s on average. In addition, the average radius explored during any trajectory segment can be measured, resulting in 0.0048 μm for confined events, while for free events it is 0.15 μm . The

degree of confinement, α_{conf} , Figure 5.14a, neatly reflects the behavior D_{ind} determined by the individual MSD calculations and the time series model, confirming that molecules exhibiting longer confinement periods show a smaller diffusion coefficient averaged over the trajectory, *cf.* Figs. 5.10a and 5.10b. The MSD vs. τ plots show $D_{conf} = 0.0124 \mu\text{m}^2 \text{s}^{-1}$ (61% of the steps), while $D_{free} = 0.81 \mu\text{m}^2 \text{s}^{-1}$ (39% of the steps), displayed in Figure 5.14d, which are reasonable compared to the D_{ind} values from both individual MSD and power law fits in Figure 5.14b.

The results from time series analysis are consistent with these conclusions and also permit the motion to be definitively classified as sub-diffusive. The measures of dimensionality k for a general Weibull model and d for the Chi fit are less than 2 for all molecules, which reinforces the presence of nanometer-scale confinement domains, as shown in Figure 5.14c. Finally, Figure 5.14d also summarizes results from statistical analysis of lateral diffusion/multistate kinetics. As discussed above, the analysis yields a two state model with transitions between subpopulations. Within this model, 77% of the steps (subpopulation 2) are at $D_1 = 0.024 \mu\text{m}^2 \text{s}^{-1}$, while the remaining 23% of the steps (subpopulation 1) are at $D_2 = 1.74 \mu\text{m}^2 \text{s}^{-1}$. These diffusion coefficients clearly bracket the ensemble average value shown in the plot. In addition, they compare quite favorably with the confinement level calculations, which are also shown for comparison. Finally, we note that the multistate kinetics model goes beyond confinement levels by allowing more complex states of motion to be analyzed. For the five molecules examined here, two states are both necessary and sufficient, but one could, in principle, identify more complex dynamics characterized by three or more distinct subpopulations based on this analysis. In such cases, use of confinement level and statistical analysis of lateral diffusion and multistate kinetics in succession could be helpful to separate and analyze a complex group of diffusion states.

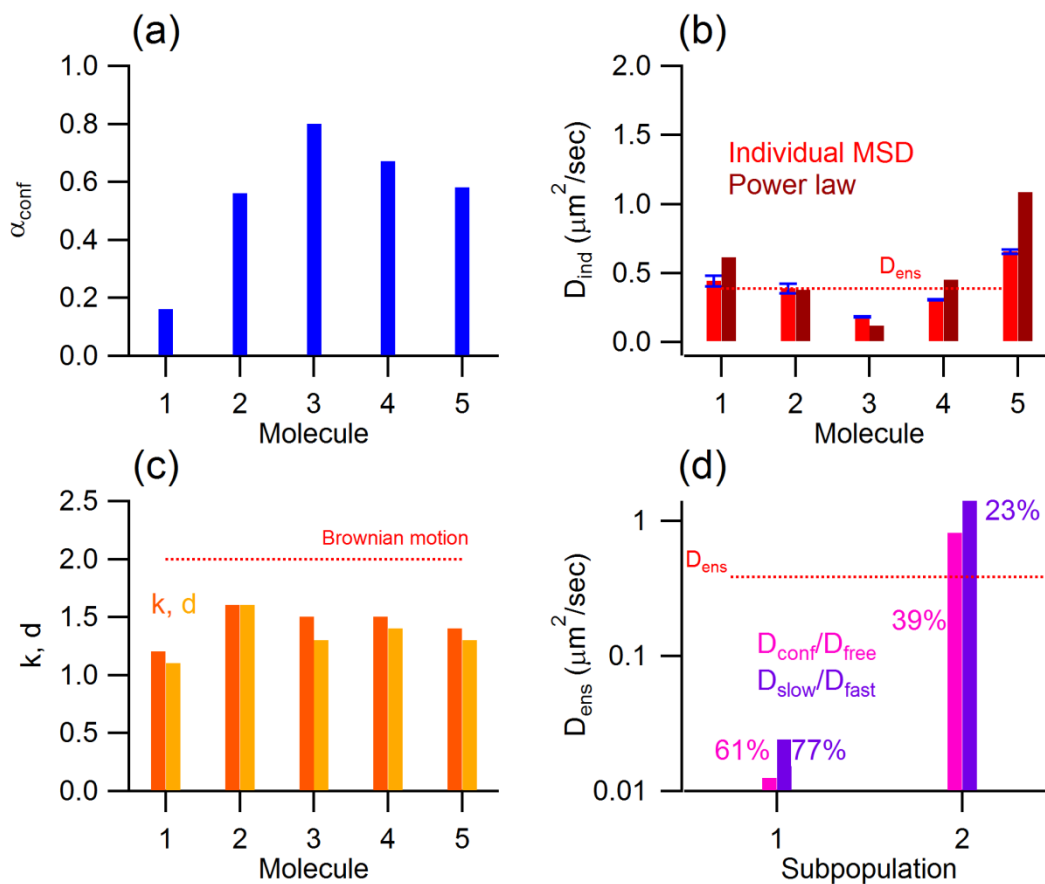


Figure 5.14: Compilation of results from all techniques. (a) Fraction of time spent in confinement, α , for each molecule determined from confinement level. (b) Individual diffusion coefficients found by the individual MSD vs. τ slopes from Table 1 (red) and power law fits from time series analysis (deep red) for all molecules. The ensemble diffusion coefficient found in Fig. 7 is shown for reference. (c) Weibull dimensionality k (dark orange) and the Chi dimensionality d (light orange) from time series analysis. The upper limit of $k, d = 2$ denotes the value for Brownian motion. (d) Diffusion coefficients of fast and slow sub-populations determined through confinement level calculations from Fig. 10 (pink) and statistical analysis of lateral diffusion (purple). The percentage of steps in each category is labeled next to the respective column, and the ensemble diffusion coefficient is displayed for comparison.

5.7 Conclusions

Each of the SMT analysis approaches applied to the data has characteristic strengths, and when taken together, they form solid basis for physical interpretation. Radius of gyration evolution nicely illustrates the area explored and mobile-immobile transitions, and, although quantitative estimates can be obtained, its real power lies in the direct visual qualitative comparisons that can be made simultaneously on both ensembles and individual trajectories. Confinement level analysis, in which each molecule is analyzed throughout its trajectory for intermittent confinement, is a highly quantitative method. The duration and radial zone of both free and confined events are obtained, as well as D_{free} , D_{conf} , and α_{conf} for each trajectory. These can then be compiled for display as histograms to reveal ensemble behavior. In addition, confinement levels can be used to map local and transient confinement in contour movies, if enough trajectories are available. The use of confinement level analysis is complicated by the fact that parameters and thresholds need to be optimized in order to identify confinement correctly and by its inability to differentiate anomalous diffusion from free diffusion.

The great advantage of times series analysis is that no inputs or choices are needed to fit MSD and probability distribution function (PDF) data, which is done for each trajectory. PDF fits characterize the excess/paucity of long/short jumps, but can be difficult to interpret. One benefit of this method is that if MSD vs. τ is non-linear, an instantaneous diffusion coefficient can still be obtained through the power law fits. Time series analysis alone, however, cannot tell the difference between intermittent diffusion and simple Brownian motion with multiple diffusion coefficients, as both confinement level and statistical analysis can. Statistical analysis and multistate kinetics analysis also needs no inputs or parameter choices and takes the user through a decision making process in which the population is analyzed with MSD vs. τ , step size PDF

fitting, Akaike information criterion determination, and autocorrelation of step size. This method is effective in determining whether the SMT is best described by one or more subpopulations with distinct diffusion coefficients, however some user discretion is required to interpret the AIC results.

The analysis of experimental and simulated data described here serves to highlight criteria for the accurate rendering of SMT data. First, in order to obtain accurate outputs from any given technique the steps per trajectory should be on the order of 50. More steps are always better, but below 50 steps the ability to recover physically-relevant information degrades rapidly. This standard is more difficult to realize with single molecules, as opposed to quantum dots, but there are still many interesting experiments for which the standard can be met. Second, in order to accurately differentiate between intermittent states of diffusion, D_{fast} should be at least 5 times larger than D_{slow} (cf. Table 5.1) This was found to be true for both confinement level calculations and statistical analysis.

In general, the various trajectory analysis methods studied partially confirm and partially complement each other. SMT data resulting from more complex physical behavior may well benefit from using these techniques in succession to identify and sort populations. In this way a comprehensive view of molecular mobility in different tracking environments may be generated and correlated to the physical and/or chemical environment in which the fluorescent probes are moving.

5.8 References

- (1) Lokuge, I.; Wang, X.; Bohn, P. W. *Langmuir* **2007**, *23*, 305-311.
- (2) Schatzel, K.; Neumann, W. G.; Muller, J.; Materzok, B. *Appl. Optics* **1992**, *31*, 770-778.

- (3) Ritchie, K.; Shan, X. Y.; Kondo, J.; Iwasawa, K.; Fujiwara, T.; Kusumi, A. *Biophys. J.* **2005**, *88*, 2266-2277.
- (4) Kusumi, A.; Sako, Y.; Yamamoto, M. *Biophys. J.* **1993**, *65*, 2021-2040.
- (5) Batista, F. D.; Treanor, B.; Harwood, N. E. *Immunol. Rev.* **2010**, *237*, 191-204.
- (6) Myong, S.; Ha, T. *Curr. Opin. Struct. Biol.*, *20*, 121-127.
- (7) Ito, S.; Kusumi, T.; Takei, S.; Miyasaka, H. *Chem. Commun.* **2009**, 6165-6167.
- (8) Sims, P. A.; Xie, X. S. *Chemphyschem* **2009**, *10*, 1511-1516.
- (9) Rocha, S.; Hutchison, J. A.; Peneva, K.; Herrmann, A.; Muellen, K.; Skjot, M.; Jorgensen, C. I.; Svendsen, A.; De Schryver, F. C.; Hofkens, J.; Uji-I, H. *Chemphyschem* **2009**, *10*, 151-161.
- (10) Edwards, A. M.; Phillips, R. A.; Watkins, N. W.; Freeman, M. P.; Murphy, E. J.; Afanasyev, V.; Buldyrev, S. V.; da Luz, M. G. E.; Raposo, E. P.; Stanley, H. E.; Viswanathan, G. M. *Nature* **2007**, *449*, 1044-1049.
- (11) Smouse, P. E.; Focardi, S.; Moorcroft, P. R.; Kie, J. G.; Forester, J. D.; Morales, J. M. *Philos. Trans. R. Soc. B-Biol. Sci.* **2010**, *365*, 2201-2211.
- (12) Borger, L.; Dalziel, B. D.; Fryxell, J. M. *Ecol. Lett.* **2008**, *11*, 637-650.
- (13) Fryxell, J. M.; Hazell, M.; Borger, L.; Dalziel, B. D.; Haydon, D. T.; Morales, J. M.; McIntosh, T.; Rosatte, R. C. *Proc. Natl. Acad. Sci. U. S. A.* **2008**, *105*, 19114-19119.
- (14) Codling, E. A.; Plank, M. J.; Benhamou, S. *J. R. Soc. Interface* **2008**, *5*, 813-834.
- (15) Gonzalez, M. C.; Hidalgo, C. A.; Barabasi, A. L. *Nature* **2008**, *453*, 779-782.
- (16) Laherrere, J.; Sornette, D. *Euro. Phys. J. B* **1998**, *2*, 525-539.
- (17) Saxton, M. J. *Biophys. J.* **1995**, *69*, 389-398.
- (18) Coscoy, S.; Huguet, E.; Amblard, F. *Bull. Math. Biol.* **2007**, *69*, 2467-2492.

- (19) Serge, A.; Bertaux, N.; Rigneault, H.; Marguet, D. *Nat. Methods* **2008**, *5*, 687-694.
- (20) Ying, W. X.; Huerta, G.; Steinberg, S.; Zuniga, M. *Bull. Math. Biol.* **2009**, *71*, 1967-2024.
- (21) Matsuoka, S.; Shibata, T.; Ueda, M. *Biophys. J.* **2009**, *97*, 1115-1124.
- (22) Elliott, L. C. C.; Barhoum, M.; Harris, J. M.; Bohn, P. W. *Phys. Chem. Chem. Phys.* **2010**, submitted.
- (23) de Keijzer, S.; Serge, A.; van Hemert, F.; Lommerse, P. H. M.; Lamers, G. E. M.; Spaink, H. P.; Schmidt, T.; Snaar-Jagalska, B. E. *J. Cell Sci.* **2008**, *121*, 1750-1757.
- (24) Meilhac, N.; Le Guyader, L.; Salome, L.; Destainville, N. *Phys. Rev. E* **2006**, *73*, 4.
- (25) Saxton, M. J. *Biophys. J.* **1993**, *64*, 1766-1780.
- (26) Simson, R.; Sheets, E. D.; Jacobson, K. *Biophys. J.* **1995**, *69*, 989-993.
- (27) Prummer, M.; Weiss, M. *Phys. Rev. E* **2006**, *74*, 4.
- (28) Yeow, E. K. L.; Melnikov, S. M.; Bell, T. D. M.; De Schryver, F. C.; Hofkens, J. *J. Phys. Chem. A* **2006**, *110*, 1726-1734.
- (29) Perronet, K.; Bouyer, P.; Westbrook, N.; Soler, N.; Fourmy, D.; Yoshizawa, S. *J. Lumines.* **2007**, *127*, 264-268.
- (30) Elenko, M. P.; Szostak, J. W.; van Oijen, A. M. *Rev. Sci. Instrum.* **2010**, *81*, 9.
- (31) Schuster, J.; Cichos, F.; von Borczyskowski, C. *Opt. Spectrosc.* **2005**, *98*, 712-717.
- (32) Paige, M. F.; Bjerneld, E. J.; Moerner, W. E. *Single Mol.* **2001**, *2*, 191-201.
- (33) Zhao, J.; Granick, S. *Macromolecules* **2003**, *36*, 5443-5446.
- (34) Chun, M. S.; Kim, C.; Lee, D. E. *Phys. Rev. E* **2009**, *79*, 051919.
- (35) Yang, S. L.; Witkoskie, J. B.; Cao, J. S. *J. Chem. Phys.* **2002**, *117*, 11010-11023.
- (36) Ke, P. C.; Naumann, C. A. *Langmuir* **2001**, *17*, 5076-5081.

CHAPTER 6

VARIABLE TEMPERATURE SINGLE MOLECULE TRACKING IN HYDRATED PNIPAAm*

Stimulus-responsive polymers (SRPs) have attracted enormous attention due to their ability to react to external stimuli by increasing or decreasing the free volume between individual polymer chains, resulting in the transport of water into or out of the material, thus producing changes in size or shape of polymer brushes consisting of these materials. Physical and chemical properties such as free volume, thickness, hydrophilicity, and charge state can all be controlled by modulating polymer density, degree of cross-linking, and chemical environment.¹⁻⁴ A variety of external stimuli, *e.g.* electric field, ionic strength and pH of the surrounding solution, analyte concentration, and light exposure, have been exploited to initiate shape/size/property transitions in different SRPs.⁵⁻⁷

One model SRP, poly(N-isopropylacrylamide), pNIPAAm, is a temperature responsive polymer that exhibits a lower critical solution temperature (LCST), at which a transition occurs - from an expanded hydrophilic form ($T < T_{LCST}$) to a collapsed, hydrophobic morphology ($T > T_{LCST}$).^{8,9} The LCST phenomenon in pNIPAAm is of great interest technologically due to its proximity to human body temperature. Thus, applications in controlled drug delivery have been widely studied, and although the phenomenology is controllable, the underlying physical and chemical behavior is found to be quite complex. For example, when the hydrated polymer sample is in a swelled state below the LCST, hydrogen bonding between water and the acrylamide C=O and N-H groups is favorable. However, at higher temperatures (starting near

* Contains material that has been submitted to Soft Matter.

32°C), inter-chain hydrogen bonding becomes more energetically stable, and interstitial water is expelled from the polymer interior in favor of these interactions.^{1,10} In addition, there is evidence from neutron reflectometry¹¹⁻¹³, quartz crystal microbalance and contact angle measurements¹⁴ that the collapse of surface bound pNIPAAm and other thermo-responsive polymer brushes is a two stage process - starting in the interior bulk region and finishing at the water-polymer interface.

While the vast majority of reported applications of SRPs have used μm -mm scale polymer monoliths, the ability to realize size and shape control on the nanometer length scale holds considerable promise for applications in tissue engineering, drug delivery systems, biosensors and actuators, and synthetic extracellular matrices.¹⁵ For example, polymer-peptide bioconjugates that respond to secreted matrix metalloproteases from cells have been used to differentiate stem cells into neurons,¹⁶⁻¹⁸ repair orthopedic defects,^{19,20} and induce vascular angiogenesis.^{21,22} Additionally, glucose-, nucleotide-, glutathione-, and antigen-responsive SRPs are being extensively studied for potential applications in controlled and feedback-looped drug release.²³⁻²⁶ However, at present, nanoscale SRP structures must be designed and tested empirically, since the behavior of SRPs is not understood well enough to support rational design with such fine control. Unfortunately, many common characterization approaches are incompatible with SRPs, because they (a) require high vacuum, as with scanning electron microscopy and transmission electron microscopy, (b) only offer surface or thickness related information, as with atomic force microscopy and profilometry, or (c) provide millimeter scale spatially averaged information, as with ellipsometry. What is needed is detailed, molecular-level information which could be used to develop predictive models for stimulus-initiated molecular reorganization.

A technique that can provide *in situ* measurements of free volume changes in SRPs with sub-micron resolution is single molecule tracking (SMT). SMT has become a viable research tool within the last two decades²⁷⁻³³ following technological advances in collection efficiency and fluorophore quantum yield and lifetime. In SMT, the paths of intrinsic, inserted, or tagged probe molecules are tracked in order to gain information about position and mobility.³⁴ This technique has the advantage of interrogating the population of fluorophores on an individual basis, thus collecting and preserving spatial and temporal heterogeneities. SMT has been applied to various complex systems, such as molecular transport in thin silica sol-gel films,³⁵ membrane dynamics,³⁶ and pore dynamics within polyacrylamide gels.³⁷ Of particular interest in our laboratories is the use of SMT to understand the molecular-scale behavior of SRPs for use in actively controlled micro total analysis systems (μ TAS).³⁸

Thus, SMT is a very attractive approach for real time investigation of spatial and temporal heterogeneities in the structure of soft materials undergoing molecular reorganization at or near the LCST. In order to examine the temperature-dependent behavior of SRPs on a single molecule level, the motions of fluorescent probes, Rhodamine6G (R6G), within surface-bound thin-films of pNIPAAm prepared by atom transfer radical polymerization (ATRP), have been studied using SMT. In addition to the specific temperature-responsive behavior of pNIPAAm studied here, the methodology can be extended to investigate the underlying basis for a wide range of soft material dynamic properties.

6.1 Sample preparation, microscopy, and analysis techniques

6.1.1 Sample preparation. 70 nm unhydrated pNIPAAm samples were prepared for this experiment using the synthetic methods described in Section 3.1.2. Single fluorescent R6G

molecules, used as the fluorescent probe, were partitioned into pNIPAAm film target media by immersion of the film in DI H₂O followed by addition of 1 nM R6G in methanol until a final concentration of 3.3 pM was reached. After partitioning, the film was imaged immediately.

6.1.2 Single molecule fluorescence microscopy. Analogous instrumentation is described in Sections 4.1 and 4.3 and data acquisition parameters are detailed in Section 5.5.1 in detail; however, a brief description follows. The microscope is an objective-based total internal reflection fluorescence (TIRF) microscope, exhibiting a 100-200 nm depth of excitation and an effective pixel size of 267 nm x 267 nm with 60X magnification. Each frame was acquired with a 30 ms exposure, using frame transfer to eliminate delay time between frames. The acquisition protocol produced videos consisting of 1000 frames, which were obtained at 23°C and at 32°C in DI water. The temperature was controlled through a Peltier heating/cooling device with a custom built aluminum sample holder and a copper block was used to control and stabilize the temperature inside the sample holder. Temperature was monitored using a thermocouple immersed in the solution of the sample holder. Single molecule tracking was carried out in a modified Matlab program^{39,40} developed specifically for SMT, discussed in detail in Section 4.10 and elsewhere.^{34,41} Briefly, tracking consists of the linked tasks of identification, localization and trajectory reconstruction. Identification and localization were realized by fitting the spatial intensity profile of each suspect molecule to a 2-D Gaussian,

$$I(x,y) = I_0 \exp\left(-\frac{(x-x_0)^2}{2\sigma_x^2} - \frac{(y-y_0)^2}{2\sigma_y^2}\right) \quad (6.1)$$

from which the centroid (x_0, y_0) and the peak standard deviations (σ_x, σ_y) were obtained using a weighted linear least squares fit. The ratio of the peak height, I_0 , to the standard deviation of the

noise in the area adjacent to the peak was used to calculate the SNR and to determine if the peak qualified as a candidate single molecule. Localization was achieved by identifying the center of the 2D Gaussian, *i.e.* (x_0, y_0) . If the SNR ratio is sufficient, then the centroid can always be localized to better precision than the diffraction limit.^{40,42} After every feature was identified in each frame, the frames were stacked in a movie and trajectories were linked together throughout the course of the movie. The localization reproducibility was determined by imaging a sample of immobilized DiIC₁₈ molecules on a glass coverslip (VWR), the absolute uncertainty being given by the standard deviation of the (x_0, y_0) positions, which were ≤ 50 nm in all cases.

6.1.3 Single molecule data analysis software. Confinement level functions in Matlab were modified to accept trajectory data from an existing tracking program and experimental protocol as covered in Section 5.3.3; this modified function is available online⁴³ and the rest of the program is available from the original authors.⁴⁴ Radius of gyration code was written in Matlab as discussed in Section 5.3.2 and is available online.⁴³

6.2 Single molecule tracking in pNIPAAm results and discussion

6.2.1 Single molecule tracking. Four separate movies of R6G probes in the same pNIPAAm sample (unhydrated thickness 70nm) and the same field of view were analyzed, two each at 23°C and 32°C to assess the reproducibility of data collection. As specified in Section 4.11, trajectories are commonly limited in length by photobleaching and other processes that convert probes to long-lived dark states.⁴⁵⁻⁴⁷ Because short trajectories are less useful for identifying differences between levels of confinement within a single track, only trajectories longer than 50 steps were used for further analysis, which resulted in 340 trajectories (29159 total steps) and

236 trajectories (18923 total steps) from the two movies at 23°C, and 1150 trajectories (99085 total steps), and 1238 trajectories (104565 total steps) from the movies at 32°C. The trajectories for R6G probes from SMT datasets at 23°C and 32°C are shown in Figures 6.1 and 6.2, respectively. It is immediately evident that the partitioning coefficient of R6G into pNIPAAm is larger at 32°C than at 23°C, resulting in many more trajectories at the higher temperature. However, the initial concentration is sufficiently small, even at 32°C, that it did not affect tracking results, meaning that probe-probe interactions, which could begin to occur when two probes occupy adjacent pixels in the same frame, were negligible. However, even if probe molecules appear in adjacent pixels, they are hundreds of nanometers from each other within the x-y plane of the brush and can be as much as tens of nanometers from each other in the film normal, z, direction due to the film thickness. Therefore, remembering that the plots in Figures 2 and 3 are compilations through all 1000 frames of a movie, using adjacent molecule-molecule appearances as a conservative criterion would still result in overestimating probe-probe events and these events were exceedingly rare. The chance of two molecules occupying the same pixel range is readily calculated with the Poisson distribution for rare events,

$$P(n) = \frac{\lambda^n e^{-\lambda}}{n!} \quad (6.2)$$

where λ is the probability of finding one molecule in a picture element and n is the # of events in a picture element, which can be determined with experimental parameters. The size of a frame (262144 pixels), size of a single molecule point spread function (9 pixels), number of features per frame (~300) result in a 1% chance of observing a molecule in one 9 pixel range. Applying Equation 6.2, there is less than 0.003% probability of observing two molecules in the same 9 pixel range.

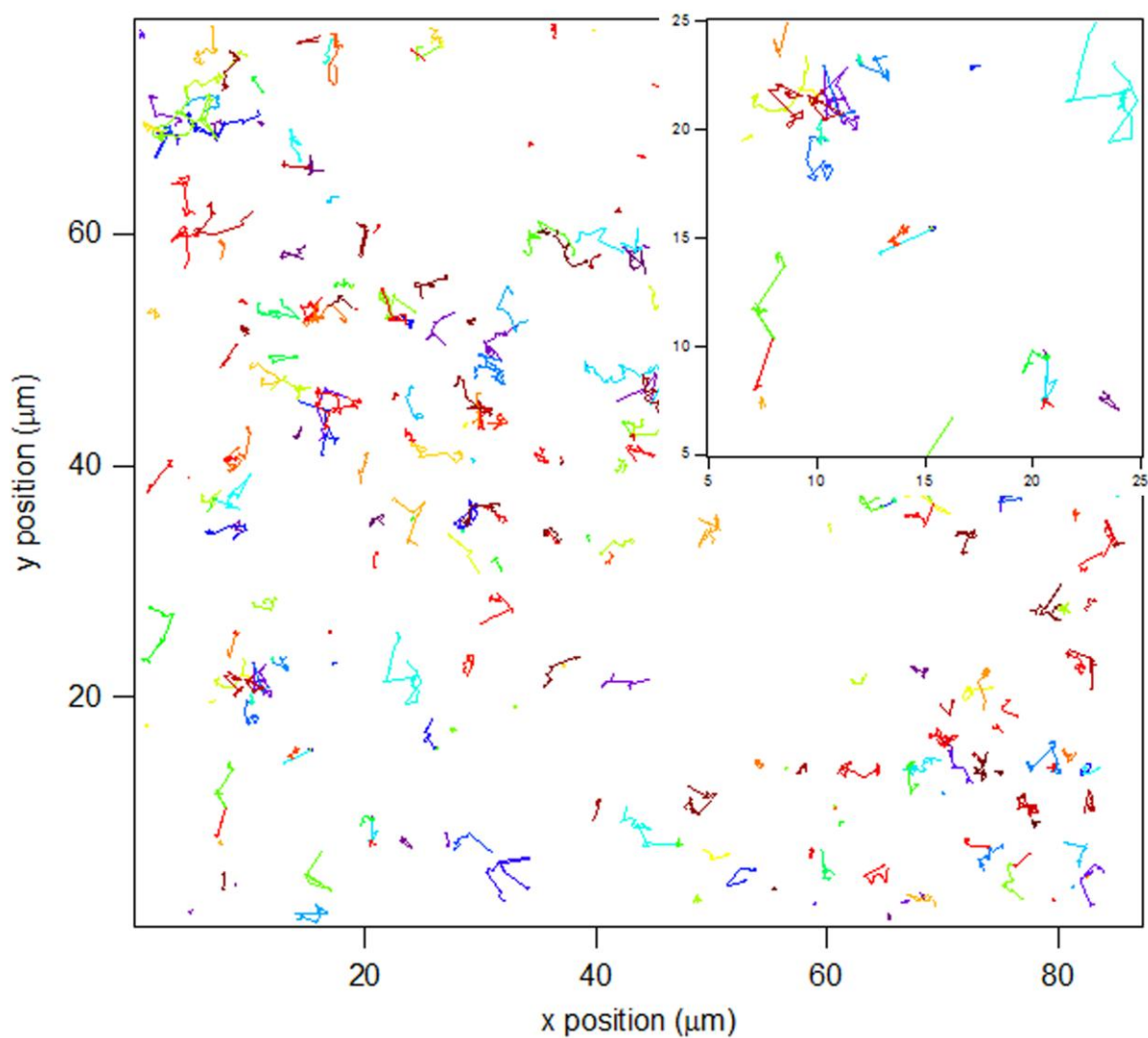


Figure 6.1: Reconstructed SMT trajectories longer than 50 frames for R6G in pNIPAAm on glass at 23°C (polymer brush in expanded state); (*Inset*) 20 μm x 20 μm expanded view.

Different colors are used for clarity.

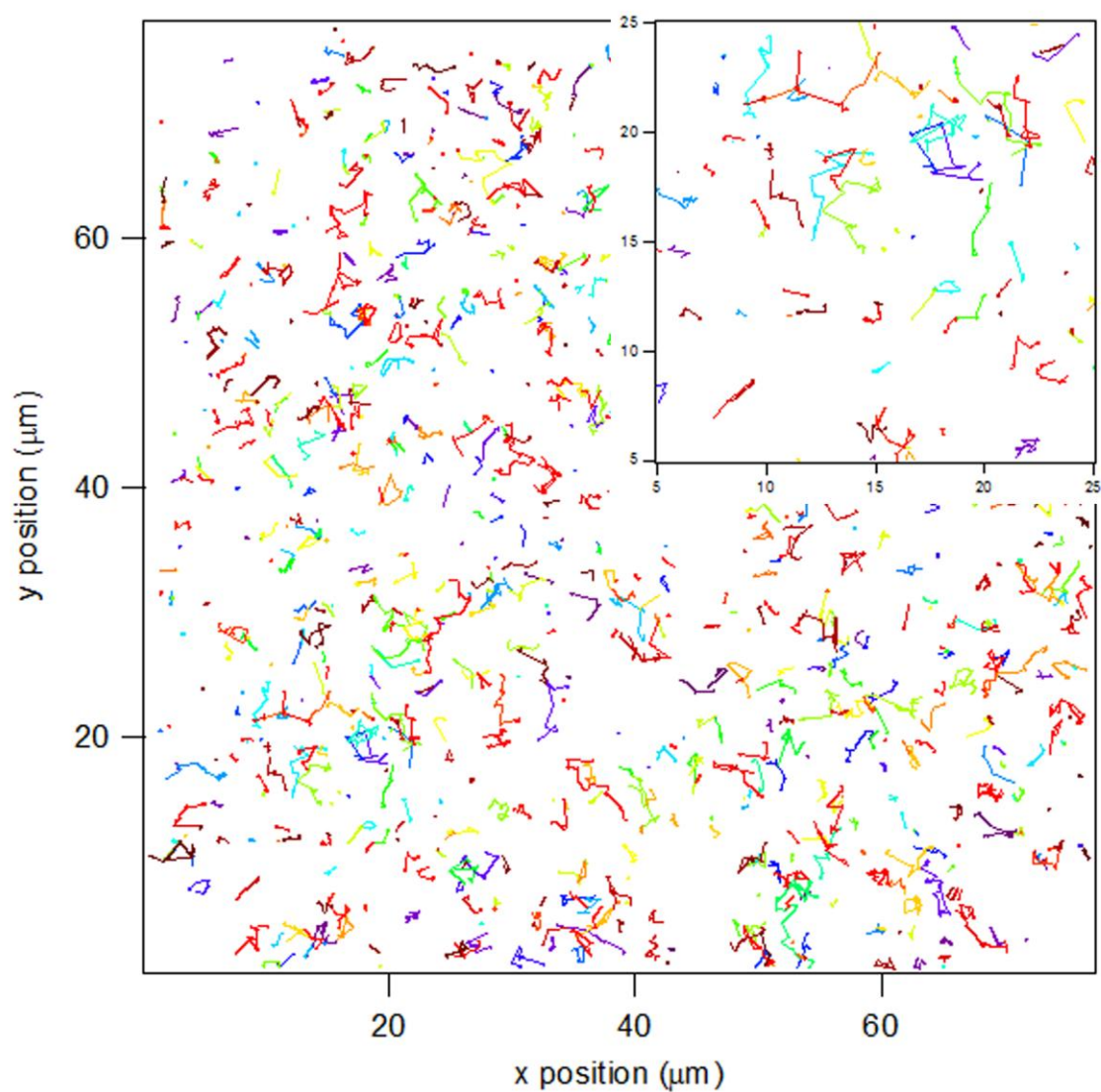


Figure 6.2: Reconstructed SMT trajectories longer than 50 frames for R6G in pNIPAAm on glass at 32°C (polymer brush in collapsed state); (*Inset*) 20 μm x 20 μm expanded view. Different colors are used for clarity.

Position and mobility of the probes are the main focus of the present study, therefore trajectories were used initially to quantify the movement of probe molecules using space explored and time spent in localized areas. In addition, the metrics can be used to categorize probes into one of three classes having: (a) small constant mobility (confined), (b) relatively large mobility (unconfined), and (c) those exhibiting one or more transitions between low and high mobility states (intermittent confinement). These analysis methods are carried out with the aim of exploring free volume changes in the polymer films through the changes in probe mobility.

The diffusion coefficient, D , obtained from the slope of mean squared displacement, $\langle x^2 \rangle$, versus time delay, τ , is a commonly used metric when quantifying motion^{27,48} and is useful as an initial estimate of the mobility in these experiments. In addition, the shape of the $\langle x^2 \rangle$ vs. τ trace is an indication of the type of diffusion in the system- confined (sub-linear), Brownian (linear), or diffusion with flow (super-linear). However, individual probe variation and randomly intermittent behavior is lost in the averaging of the squared displacement. Thus, it is important to distinguish D values calculated for individual probes and those for ensembles of many probe molecules, and D values calculated for categorized segments. The ensemble-averaged diffusion coefficient (D_{ens}) calculated for the molecules studied in these experiments lies in the range $0.18 \mu\text{m}^2 \text{ s}^{-1} < D_{ens} < 0.36 \mu\text{m}^2 \text{ s}^{-1}$ independent of temperature. Since this cursory inspection of population-averaged diffusion coefficients produces the same D_{ens} at 23°C and 32°C trajectories, despite the known LCST phase transition in the SRP, clearly a more thorough analysis is warranted.

6.2.2 Immobilized DiI data. Adsorbed DiI dried on a glass coverslip was used as a check on the spatial resolution limit. A standard example is shown Figure 6.3 for a molecule with SNR in the range 9.7-12.8 throughout a 1000 frame movie. The standard deviation in x and y are both ~ 35 nm, and the average displacement is 50 nm which yields a minimum diffusion coefficient of $0.01 \mu\text{m}^2 \text{s}^{-1}$ with 30 ms exposures.

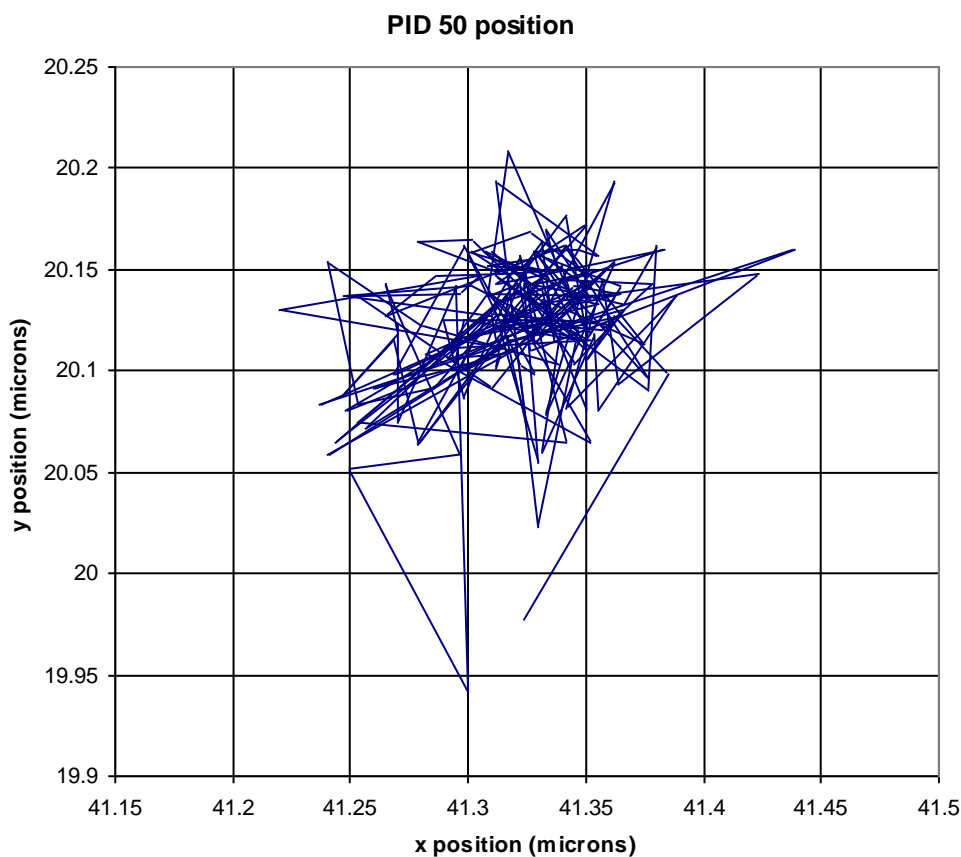


Figure 6.3: Position plot of tracking data obtained from an adsorbed DiIC₁₈ molecule on glass, SNR 9.7-12.8, used for spatial resolution characterization from a movie with 30 ms exposures.

6.2.3 Temperature dependent SMT data. Analysis of the temperature specific behavior of R6G probes was carried out using a suite of robust statistical tools available for comparison of SMT data.⁴³ Among the available tools, confinement level analysis^{44,49} and radius of gyration

evolution,⁴³ methods that are featured in Sections 5.3.3 and 5.3.2, respectively, were found to be most useful in distinguishing between pNIPAAm states and physical properties above and below the LCST. In summary, confinement level calculations are carried out on a molecule-by-molecule basis in order to determine ‘confined’ and ‘free’ segments, *i.e.* portions or whole trajectories that exhibit higher and lower relative confinement relative to a well-defined threshold. Several metrics are obtained from these results, including the fraction of confined steps within the trajectory, α , the duration of confined and free portions of the trajectory, and the radii of free and confined zones. Once all trajectories are evaluated from SMT movies, these quantities can be compiled into histograms that convey the distribution of behavior observed across the entire sample.

The radius of gyration, R_g , of a trajectory describes the amount of space that the molecule explores during its movement, calculated as the root mean square distance from the trajectory’s center of mass,

$$R_g = \sqrt{R_1^2 + R_2^2} \quad (6.3)$$

where R_1 and R_2 are the major and minor eigenvalues, respectively, of the radius of gyration tensor, \mathbf{T} . The tensor \mathbf{T} is calculated from the x and y positions of the particle throughout its trajectory,

$$\hat{T} = \begin{pmatrix} \frac{1}{N} \sum_{j=1}^N (x_j - \langle x \rangle)^2 & \frac{1}{N} \sum_{j=1}^N (x_j - \langle x \rangle)(y_j - \langle y \rangle) \\ \frac{1}{N} \sum_{j=1}^N (x_j - \langle x \rangle)(y_j - \langle y \rangle) & \frac{1}{N} \sum_{j=1}^N (y_j - \langle y \rangle)^2 \end{pmatrix} \quad (6.4)$$

Thus, radius of gyration evolution quantifies the amount of space that a molecule explores. This value evolves over time for each molecule as motion is tracked and can be plotted vs. time in

order to observe the progression. R_g evolution is especially useful in allowing the statistical outliers, for example molecules that exhibit multiple confined-to-mobile or mobile-to-confined transitions, to be identified in the presence of the ensemble-average behavior. In addition, all the values of R_g or the final R_g for each molecule can be plotted in a histogram to identify measurable differences.

6.2.3.1 Confinement level calculations.^{44,49} Free and confined portions of each trajectory were compiled separately, from which individual probe molecule diffusion coefficients were determined from the mean squared displacement. Averaging over all segments placed in each category from all four movies yields $D_{confined} = 0.007 \text{ } \mu\text{m}^2 \text{ s}^{-1}$ and $D_{free} = 1.27 \text{ } \mu\text{m}^2 \text{ s}^{-1}$. The ‘confined’ diffusion segment can be considered immobile within the limits of the instrument and tracking limit given the results from adsorbed DiI tracking. As with the ensemble averaged D , these values are helpful as a guide to the magnitude of the mobility corresponding to qualitatively distinct trajectory segments. In addition, they clearly define how much separation exists between the indicators for confined and free behavior observed in these samples. The next step beyond statistical description of confined and mobile segments examines the confinement level calculations of α , which show a consistent difference between temperatures above and below the LCST, as shown in Figure 6.4. Statistical parameters from the Gaussian fits of the α distributions are compiled in Table 6.1.

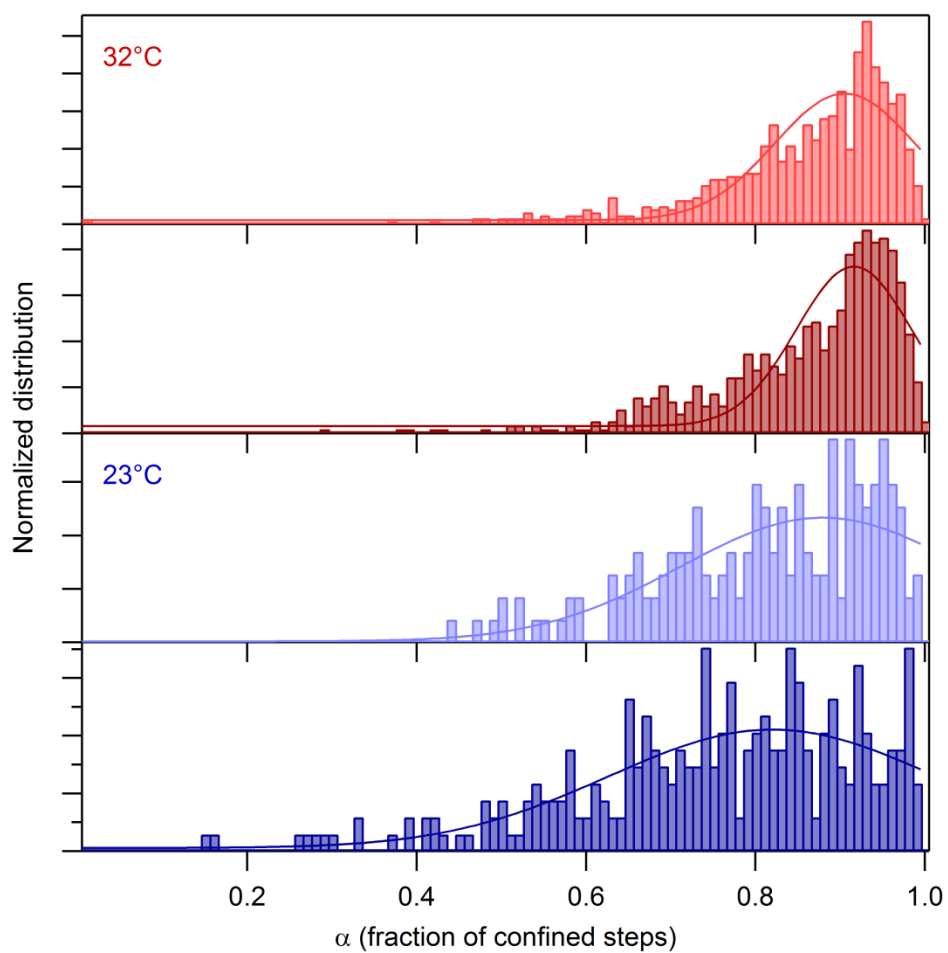


Figure 6.4: Confinement level analysis results for two separate samples of R6G probes in the same pNIPAAm sample on glass at 23°C (dark blue, light blue) and 32°C (dark red, light red). Solid lines are Gaussian curve fits with peak and width parameters given in Table 6.1.

Table 6.1: Degree of confinement fit parameters

Dataset	Peak	Width
32- #2	0.91	0.12
32- #1	0.92	0.10
23- #2	0.88	0.24
23- #1	0.82	0.27

Consistent differences between high and low temperature fraction of confinement can be clearly observed in both the peak positions and widths of the α distributions. Both of the high temperature experiments exhibit a large fraction of confined steps, while the 23°C data show smaller peak α values. More strikingly, the low temperature distributions have a much longer tail at smaller α values, indicating a larger number of trajectories that exhibit a smaller fraction of confined steps. The usual increase in diffusion coefficient with temperature predicted by the Stokes-Einstein equation, corresponding to an increase in MSD under free diffusion conditions, stands in contrast to the larger degree of confinement at higher temperature seen in these data. This obvious, reproducible indication of the higher level of confinement at 32°C correlates intuitively with a collapsed morphology of pNIPAAm, in spite of the increased thermal energy available to the probes. This higher confinement is explained by a decrease in the amount of water between chains, which is caused by collapse of the pNIPAAm chains at $T > T_{LCST}$. Thus, the dissolved fluorophore molecules have less space between polymer chains to explore.

Two additional metrics that can be extracted from confinement level analysis provide interesting insights into the differences between states of pNIPAAm above and below the LCST. Figure 6.5a shows the duration of confined events, compiled as histograms of the confined portions of all trajectories. The 32°C traces (red) clearly show a long duration tail, giving a distribution that can be fit by a double Lorentzian function, while the 23°C traces (blue) show a single peak that fits a single Lorentzian. Furthermore, the fit parameters given in Table 6.2 confirm that the higher temperature distributions exhibit a second population of confined probe molecules that are immobile for ~ 4 times as long as the main part of the population. Additional insight into this phenomenon can be gleaned from the Lorentzian fits for the distributions of confined zone radii displayed in Figure 6.5b, which also exhibit systematic differences between

$T > T_{LCST}$ and $T < T_{LCST}$. At 23°C the radii of confined zones in the two experiments peak at 54 nm with FWHM 70 nm and 43 nm with FWHM 31 nm, while at 32°C the distributions are sharper and smaller at 32 nm with FWHM 20 nm and 31 nm with FWHM 20 nm, a 34% average decrease at higher temperature.

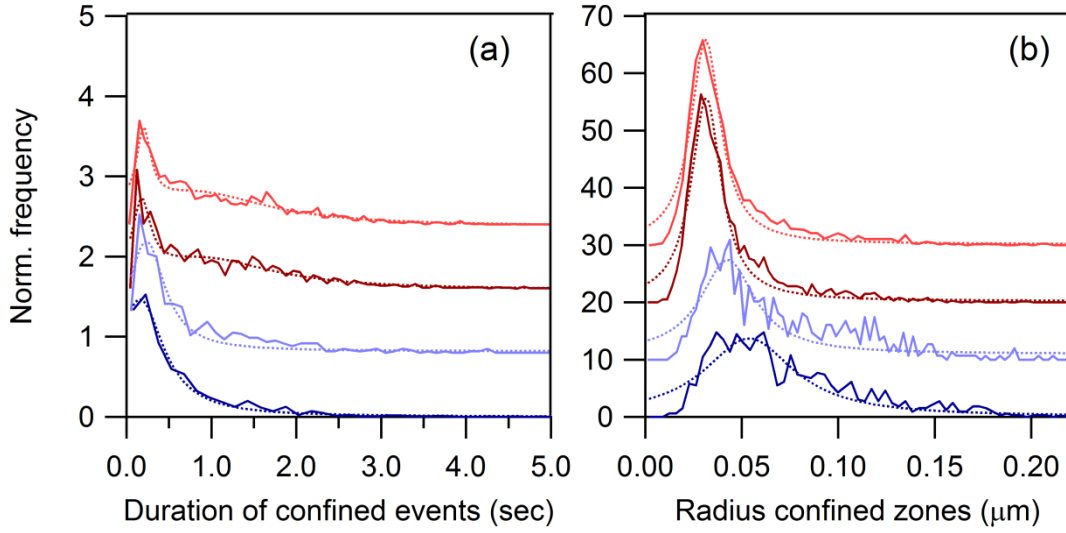


Figure 6.5: Confinement level analysis for R6G in pNIPAAm at 23°C (dark blue, light blue) and 32°C (dark red, light red), two trials each. Traces are offset for clarity and the inset emphasizes the difference between the tail at 23°C and 32°C. (a) Normalized histograms of the duration of confined events, with fits (dashed lines) for single (23°C) and double (32°C) Lorentzian functions. Fit parameters are given in Table 6.2. (b) Distribution of the radius of confined zones. Single Lorentzian functions (dashed lines) are fit to these distributions, with peak and width parameters given in Table 6.3.

Table 6.2: Duration of confined events fit parameters

Dataset	Peak A (sec)	Width A (sec)	Peak B (sec)	Width B (sec)
32- #2	0.20	0.06	0.82	0.31
32- #1	0.18	0.01	0.91	2.04
23- #2	0.23	0.52	--	--
23- #1	0.16	0.68	--	--

Table 6.3: Radius of confined zones fit parameters

Dataset	Peak (nm)	Width (nm)
32- #2	31	20
32- #1	32	20
23- #2	43	31
23- #1	54	70

When considered together, the confinement level analysis shows that in the 32°C state R6G probes in pNIPAAm: (i) exhibit a higher fraction of confined steps, (ii) are confined for longer periods of time, and (iii) are confined to smaller areas than in the 23°C state. In addition, the fact that two Lorentzian peaks best fit the duration of confined event histograms at 32°C suggests that there may be more than one distinct confinement mechanisms in pNIPAAm above the LCST.

6.2.3.2 Radius of gyration evolution. Radius of gyration evolution for two experiments, one at 23°C and the other at 32°C, are shown in Figures 6.6a and 6.6b, respectively. Only trajectories longer than 150 steps were included in these two plots in order that individual traces could be visually resolved. Differences between low and high temperature probe movement are readily apparent. Relatively immobile molecules, showing little increase in R_g over the course of the

trajectory, and intermittent confinement behavior, as evidenced by consecutive increases and plateaus/decreases in R_g , are observable in both plots. However, the magnitude is clearly different above and below T_{LCST} .

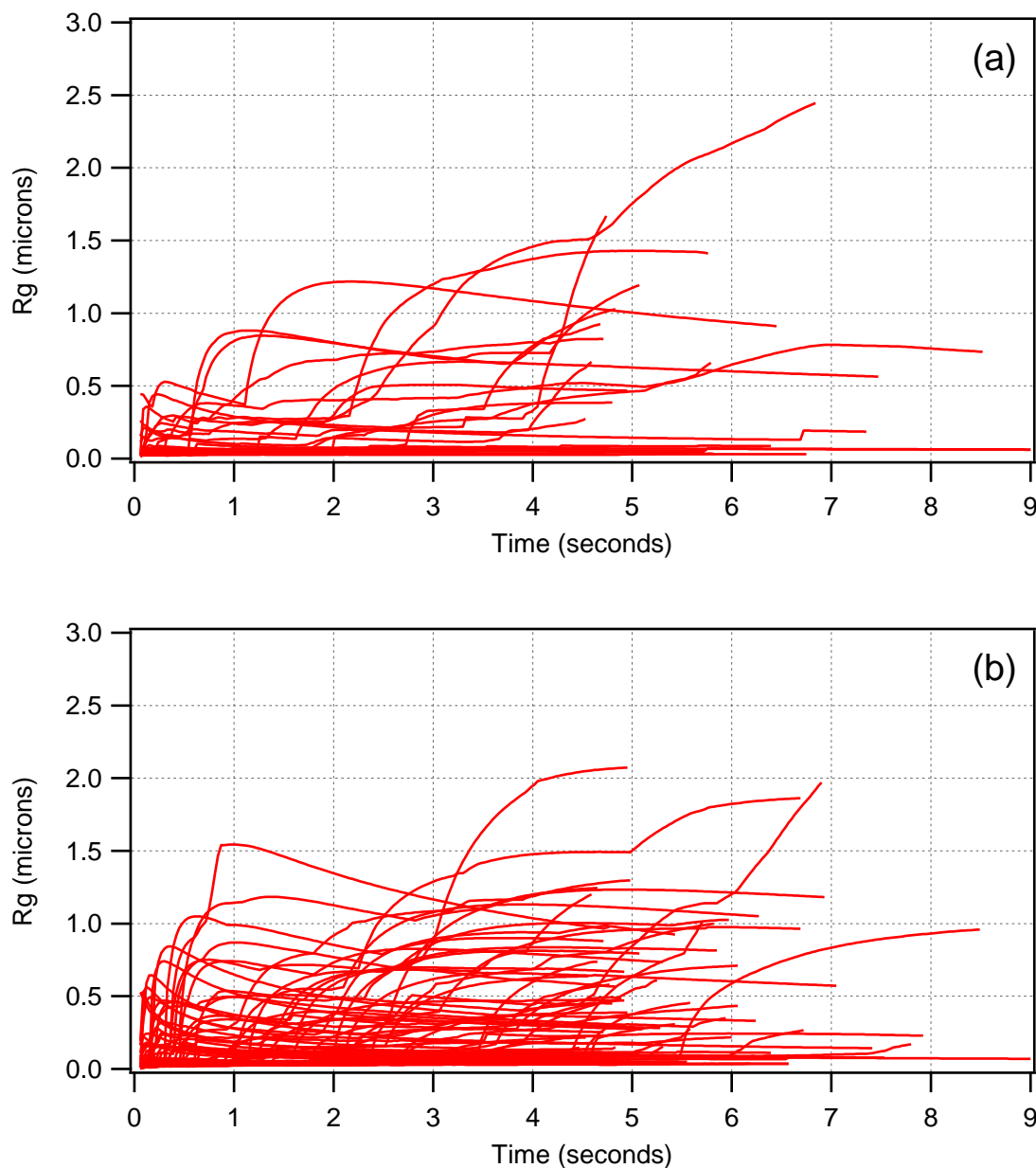


Figure 6.6: Radius of gyration evolution for trajectories at 23°C (a) and 32°C (b) of R6G in pNIPAAm on glass. Only trajectories longer than 150 steps only are included.

The difference in probe mobility between low and high temperature can be seen in the histogram of final R_g values for each molecule (trajectories longer than 50 steps) shown in Figure 6.7. The peak and width of fits to the final R_g histograms, representing the amount of space that a molecule explores throughout its trajectory are given in Table 6.4. On average these values are larger for the low temperature pNIPAAm films (70 nm with FWHM 71 nm and 48 nm with FWHM 29 nm) than for those studied at high temperature (46 nm with FWHM 29 nm and 46 nm with FWHM 17 nm).

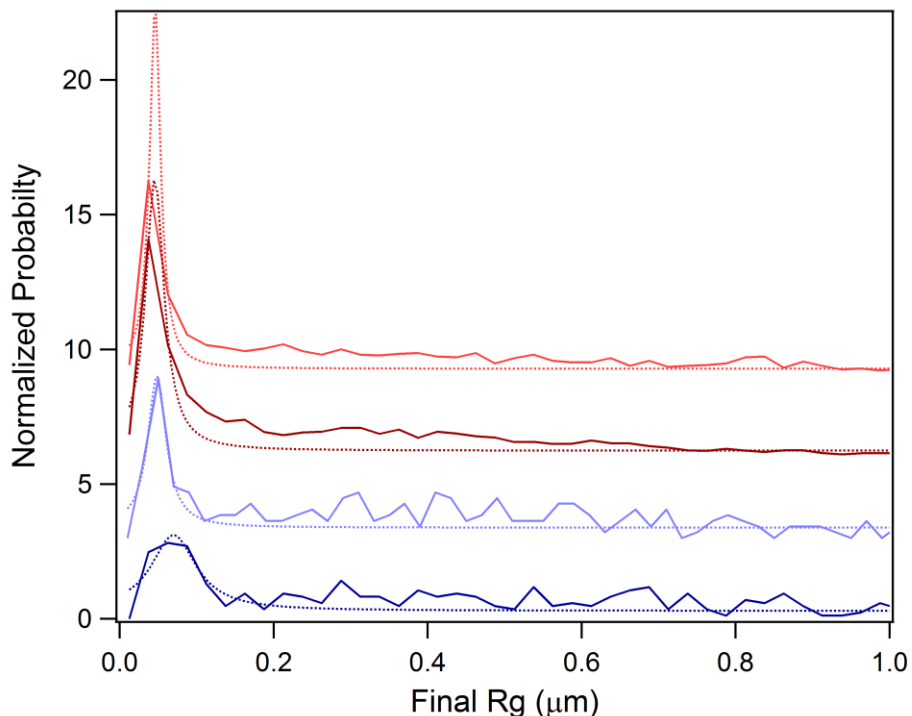


Figure 6.7: Histograms of the final R_g value for each molecule in SMT movies 23°C (dark and light blue) and 32°C (dark and light red). The traces are offset for clarity. Peaks and FWHM from Lorentzian fits to the experimental histograms are given in Table 6.4.

Table 6.4: R_g histogram fit parameters

Dataset	Peak (nm)	Width (nm)
32- #2	46	17
32- #1	46	29
23- #2	48	29
23- #1	70	71

These results agree with those obtained from confinement level analysis, thereby augmenting the evidence for enhanced confinement in pNIPAAm at $T > T_{LCST}$. At 23°C the average radius of confinement of trajectory segments is 49 nm and the average final R_g is 59 nm, an increase of 20%. At 32°C the corresponding values are 32 nm and 46 nm, an increase of 44%. Therefore, single R6G molecule probes in PNIPAAm at 32°C explore less space and have larger jumps between confined zones than at 23°C.

6.2.4 Interpretation of increased confinement in single molecule trajectories. These experiments do not differentiate between the two possible mechanisms- physical (steric hindrances) or chemical (interactions between probe and sample)- for the increased confinement observed in these variable temperature SMT studies. Physical confinement could, for example, be due to collapse of local structure in pNIPAAm and the corresponding decrease in free volume when water is expelled. The change in water content can be calculated for an 80 nm unhydrated pNIPAAm sample using the temperature dependent refractive index of hydrated pNIPAAm (from Figure 3.7), pure water ($n = 1.33$), and unhydrated pNIPAAm brush ($n = 1.55$). Using this method, the water content at 23°C is found to be 61%, while the corresponding water content at 32°C is 50%, an ~20% decrease. Chemical interactions could arise from electrostatic attraction between the cationic R6G and anionic surface charge of the silica substrate, which would

become stronger when the polymer collapsed and the proximity between the silica surface and the probe molecules increased. Another source of chemical interactions could be hydrophobic van der Waals (vdW) interactions between the probes and the pNIPAAm chains, which could increase when the polymer enters the hydrophobic regime above the LCST. The ~3X increase in the number density of fluorophores observed in pNIPAAm at 32°C relative to 23°C (Section 6.2.1) provides some evidence for the increase in probe-chain vdW interactions. In order to have switching between free and associated states as observed at both temperatures, the intermolecular forces involved would have to be close to this strength, (thermal energy at 23°C is 3.7 kJ/mol and 32°C is 3.8 kJ/mol) which makes van der Waals forces, ~4 kJ/mol, the most likely contribution (hydrogen bonding and electrostatic interactions are 5-10X stronger than kT at these temperatures). Based on the similarity in energy levels, it is possible, therefore, that vdW forces contribute to the confinement exhibited by the tracked molecules at $T > T_{LCST}$ and $T < T_{LCST}$.

A comparison of the diffusion of two different probe populations within pNIPAAm can be used to qualitatively explore the effect that vdW forces have in these experiments. The two data sets are from the tracking movies at 23°C presented in this chapter for R6G and from the five sample trajectories of DiIC₁₈ in pNIPAAm at 23°C from Chapter 5. Both sets of data have enough steps to accurately characterize the motion exhibited by probe molecules (based on the 50 step cutoff established by simulation trajectories). The two types of probe molecules are similar in size, possess the same charge, and yet DiIC₁₈ is much more hydrophobic than R6G. Despite the large difference in polar/non-polar character, however, the average diffusion coefficients of the two probe populations differ by only ~1.5X ($D_{R6G} = 0.26 \mu\text{m}^2/\text{sec}$ and $D_{DiIC18} = 0.40 \mu\text{m}^2/\text{sec}$). This strongly suggests that the interactions between the probes and the polymer chains do not play such a large role in the confinement behavior of these probe molecules.

Rather it is more likely that confined trajectories result from physical confinement due to the pNIPAAm chains.

6.3 Conclusions

A new method utilizing single molecule tracking to explore materials exhibiting temporally and spatially heterogeneous behavior has been applied to pNIPAAm, an archetypal SRP, at temperatures below and above its LCST, where it has been shown to exist in swelled and collapsed states, respectively. Several major conclusions can be drawn from a careful analysis utilizing confinement level and radius of gyration evolution to quantify the motion of R6G single molecule probes. First, probe behavior in the pNIPAAm films is best characterized by the degree of confinement that correlates with film morphology between swelled ($T < T_{LCST}$) or collapsed ($T > T_{LCST}$) states of the polymer and that behavior can be used to understand the different states of the brush. In addition, a combination of confinement level metrics - α , duration of confined events, and radius of confined zones - and radius of gyration evolution results can be used to illuminate the differing transport properties of hydrated pNIPAAm in swelled and collapsed states. Of particular note here is the consistent interpretation of probe motion in the collapsed state above the LCST as: (1) being confined to smaller areas, (2) showing a higher fraction of confined segments, and (3) having a greater propensity to exhibit larger jumps between confined zones. At this point, it is not possible to quantify how much of the mechanism for probe molecule confinement has a physical (entanglement under collapsed chains) or chemical (specific interactions with domains in the polymer) origin. However, as indicated by the comparison of two probes, R6G and DiIC₁₈, the chemical interactions likely play a small role compared to physical entanglement, which is a significant factor based on the

change in water content. Finally, this analysis of the non-Brownian (sub-diffusive) motion of single probe molecules serves to highlight the benefits of tracking individual molecular probes as an approach to understanding the complex dynamics of network-based SRPs. In addition to exploring the macromolecular reorganization in network polymers, we believe that this technique will find application to a wide range of soft materials in which nanometer-scale state changes are crucial to function, such as molecular gates devices, artificially engineered tissue, 3-D cell supports, extracellular matrix mimetics, and controlled drug delivery systems.

6.4 References

- (1) Urban, M. W. *Polym. Rev.* **2006**, *46*, 329-339.
- (2) Ahn, S. K.; Kasi, R. M.; Kim, S. C.; Sharma, N.; Zhou, Y. X. *Soft Matter* **2008**, *4*, 1151-1157.
- (3) Stuart, M. A. C.; Huck, W. T. S.; Genzer, J.; Muller, M.; Ober, C.; Stamm, M.; Sukhorukov, G. B.; Szleifer, I.; Tsukruk, V. V.; Urban, M.; Winnik, F.; Zauscher, S.; Luzinov, I.; Minko, S. *Nat. Mater.* **2003**, *9*, 101-113.
- (4) Yim, H.; Kent, M. S.; Mendez, S.; Lopez, G. P.; Satija, S.; Seo, Y. *Macromolecules* **2006**, *39*, 3420-3426.
- (5) Gil, E. S.; Hudson, S. A. *Prog. Polym. Sci.* **2004**, *29*, 1173-1222.
- (6) *Field Responsive Polymers. Electroresponsive, Photoresponsive, and Responsive Polymers in Chemistry and Biology. ACS Symposium Series 726* American Chemical Society: Washington, DC, 2000; Vol. 122.
- (7) Gehrke, S. H. *Adv. Polym. Sci.* **1993**, *110*, 81-144.
- (8) Pelton, R. H.; Chibante, P. *Coll. Surf.* **1986**, *20*, 247-256.

- (9) Kaholek, M.; Lee, W. K.; Ahn, S. J.; Ma, H. W.; Caster, K. C.; LaMattina, B.; Zauscher, S. *Chem. Mat.* **2004**, *16*, 3688-3696.
- (10) Zhulina, E. B.; Borisov, O. V.; Pryamitsyn, V. A.; Birshstein, T. M. *Macromolecules* **1991**, *24*, 140-149.
- (11) Zhang, J. M.; Nylander, T.; Campbell, R. A.; Rennie, A. R.; Zauscher, S.; Linse, P. *Soft Matter* **2008**, *4*, 500-509.
- (12) Yim, H.; Kent, M. S.; Huber, D. L.; Satija, S.; Majewski, J.; Smith, G. S. *Macromolecules* **2003**, *36*, 5244-5251.
- (13) Yim, H.; Kent, M. S.; Satija, S.; Mendez, S.; Balamurugan, S. S.; Balamurugan, S.; Lopez, G. P. *Phys. Rev. E* **2005**, *72*, 051801.
- (14) Laloyaux, X.; Mathy, B.; Nysten, B.; Jonas, A. M. *Langmuir* **2010**, *26*, 838-847.
- (15) Chaterji, S.; Kwon, I. K.; Park, K. *Prog. Polym. Sci.* **2007**, *32*, 1083-1122.
- (16) Tibbitt, M. W.; Anseth, K. S. *Biotechnol. Bioeng.* **2009**, *103*, 655-663.
- (17) Park, K. I.; Teng, Y. D.; Snyder, E. Y. *Nat. Biotechnol.* **2002**, *20*, 1111-1117.
- (18) Nur-E-Kamal, A.; Ahmed, I.; Kamal, J.; Schindler, M.; Meiners, S. *Stem Cells* **2006**, *24*, 426-433.
- (19) Lutolf, M. R.; Weber, F. E.; Schmoekel, H. G.; Schense, J. C.; Kohler, T.; Muller, R.; Hubbell, J. A. *Nat. Biotechnol.* **2003**, *21*, 513-518.
- (20) Liu, Y. C.; Ahmad, S.; Shu, X. Z.; Sanders, R. K.; Kopesec, S. A.; Prestwich, G. D. *J. Orthop. Res.* **2006**, *24*, 1454-1462.
- (21) D'Andrea, L. D.; Del Gatto, A.; Pedone, C.; Benedetti, E. *Chem. Biol. Drug Des.* **2006**, *67*, 115-126.

- (22) Rouet, V.; Hamma-Kourbali, Y.; Petit, E.; Panagopoulou, P.; Katsoris, P.; Barritault, D.; Caruelle, J. P.; Courty, J. *J. Biol. Chem.* **2005**, *280*, 32792-32800.
- (23) Kashyap, N.; Kumar, N.; Kumar, M. *Crit. Rev. Ther. Drug Carr. Syst.* **2005**, *22*, 107-149.
- (24) Kang, S. I.; Bae, Y. H. *J. Control. Release* **2003**, *86*, 115-121.
- (25) Kakizawa, Y.; Harada, A.; Kataoka, K. *Biomacromolecules* **2001**, *2*, 491-497.
- (26) Miyata, T.; Asami, N.; Uragami, T. *Nature* **1999**, *399*, 766-769.
- (27) Kusumi, A.; Sako, Y.; Yamamoto, M. *Biophys. J.* **1993**, *65*, 2021-2040.
- (28) Ishihara, A.; Jacobson, K. *Biophys. J.* **1993**, *65*, 1754-1755.
- (29) Ghosh, R. N.; Webb, W. W. *Biophys. J.* **1994**, *66*, 1301-1318.
- (30) Kubitscheck, U.; Wedekind, P.; Peters, R. *Biophys. J.* **1994**, *67*, 948-956.
- (31) Saxton, M. J. *Biophys. J.* **1995**, *69*, 389-398.
- (32) Cherry, R. J.; Wilson, K. M.; Triantafilou, K.; O'Toole, P.; Morrison, I. E. G.; Smith, P. R.; Fernandez, N. *J. Cell Biol.* **1998**, *140*, 71-79.
- (33) Simson, R.; Sheets, E. D.; Jacobson, K. *Biophys. J.* **1995**, *69*, 989-993.
- (34) Crocker, J. C.; Grier, D. G. *J. Colloid Interface Sci.* **1996**, *179*, 298-310.
- (35) McCain, K. S.; Hanley, D. C.; Harris, J. M. *Anal. Chem.* **2003**, *75*, 4351-4359.
- (36) Saxton, M. J.; Jacobson, K. *Annu. Rev. Biophys. Biomolec. Struct.* **1997**, *26*, 373-399.
- (37) Dickson, R. M.; Norris, D. J.; Tzeng, Y. L.; Moerner, W. E. *Science* **1996**, *274*, 966-969.
- (38) Lokuge, I.; Wang, X.; Bohn, P. W. *Langmuir* **2007**, *23*, 305-311.
- (39) Anthony, S.; Zhang, L. F.; Granick, S. *Langmuir* **2006**, *22*, 5266-5272.
- (40) Anthony, S. M.; Granick, S. *Langmuir* **2009**, *25*, 8152-8160.
- (41) Weeks, E. R.; Crocker, J. C.; Levitt, A. C.; Schofield, A.; Weitz, D. A. *Science* **2000**, *287*, 627-631.

- (42) Qu, X. H.; Wu, D.; Mets, L.; Scherer, N. F. *Proc. Natl. Acad. Sci. U. S. A.* **2004**, *101*, 11298-11303.
- (43) Elliott, L. C. C.; Barhoum, M.; Harris, J. M.; Bohn, P. W. *Phys. Chem. Chem. Phys.* **2010**, submitted.
- (44) Serge, A.; Bertaux, N.; Rigneault, H.; Marguet, D. *Nat. Methods* **2008**, *5*, 687-694.
- (45) Deschenes, L. A.; Bout, D. A. V. *Chem. Phys. Lett.* **2002**, *365*, 387-395.
- (46) Schuster, J.; Brabandt, J.; von Borczyskowski, C. *J. Lumines.* **2007**, *127*, 224-229.
- (47) van Dijk, M. A.; Kapitein, L. C.; van Mameren, J.; Schmidt, C. F.; Peterman, E. J. G. *J. Phys. Chem. B* **2004**, *108*, 6479-6484.
- (48) Ritchie, K.; Shan, X. Y.; Kondo, J.; Iwasawa, K.; Fujiwara, T.; Kusumi, A. *Biophys. J.* **2005**, *88*, 2266-2277.
- (49) de Keijzer, S.; Serge, A.; van Hemert, F.; Lommerse, P. H. M.; Lamers, G. E. M.; Spaink, H. P.; Schmidt, T.; Snaar-Jagalska, B. E. *J. Cell Sci.* **2008**, *121*, 1750-1757.

CHAPTER 7

FUTURE DIRECTIONS

7.1 Summary

The work in this thesis has demonstrated that the tracking of single molecule probes is an effective tool to learn about differences in the free volume of stimulus responsive polymers. SMT experiments have been carried out on fluorophore populations in pNIPAAm brushes. Position data from SMT movies at temperatures above and below the LCST has been obtained through automated Matlab algorithms. Four analysis methods have been developed and compiled that quantify the length- and time-scales of these differences. The following are suggestions for possible extensions of the work in this project.

7.2 Future directions

7.2.1 Complementary SMT and neutron reflectometry experiments. A relevant question with which to complement SMT results would address how probe fluorophores partition in to pNIPAAm films. The widefield and TIRF microscopes that were used in this project track position in the plane of the polymer only, providing no information about probe position or movement normal to the substrate surface (in the z-direction). The optics in these experiments could be modified to give 3-D information by inserting an additional lens into the collection path,^{1,2} however, this would only reveal whether the probes were moving in and out of the pNIPAAm, since the thickness of the brush phases studied are less than the z-resolution that can be obtained by optical microscopy. Given that there is evidence that the temperature induced transition in pNIPAAm brushes is a two phase process involving differences between the surface

and the bulk, knowing the location of the probe molecules relative to the substrate would be very useful. This could be done with neutron reflectometry (NR), the technique that has been used to elucidate polymer brush density profiles in the z-direction and to explore the two phase collapse in pNIPAAm.³⁻⁸ NR requires that a neutron scattering contrast exists between the fluorophore and the hydrated polymer sample, which precludes the use of dyes that are composed only of carbon, nitrogen, and oxygen. One candidate fluorophore that meets the requirements for NR and has been used for SMT is Bodipy FL. Neutron reflectometry, which supplies nanometer resolution z-density profiles but averages over the x-y plane, and SMT, which provides tens of nanometer x-y resolution, but no z information, would be an interesting combination. The success of using these two techniques together depends on getting results from both sets of experiments. The challenge lies in producing pNIPAAm samples for NR with sufficiently small surface roughness and homogeneous x-y coverage on silicon that are similar enough to compare to the SMT samples on silica. The optimal polymer thickness for NR samples is ~35 nm thick unhydrated, and the most interesting SMT results were obtained from 70 nm thick unhydrated samples. Another difference is the amount of fluorophore needed for the two techniques; a solution concentration of 10^{-10} - 10^{-12} M is optimal to obtain sufficient SMT spacing for Bodipy FL, for example, in contrast to the much higher concentration that can be found using NR scattering calculations. Deuterated water is also required for NR experiments to provide scattering contrast between the polymer-water region and the fluorophore. Thus, it would be necessary to test the assumption that the partitioning of the dye or the temperature response of the pNIPAAm would not be affected by the relative amounts of fluorophore in the polymer brush within this concentration range or by the difference between H₂O and D₂O. The validity of the first assumption is more problematic than the second, since chemical and physical properties

such as hydrogen bonding do not change in deuterated solvents. A joint proposal with Susan Fullerton at Notre Dame for neutron beam-time at the NIST facility has been approved to implement these experiments.

7.2.2 Further analysis of SMT data. During the collection of SMT movies with Bodipy FL, R6G, and DiIC₁₈, two observations were made concerning differences in the behavior of the probe molecules. The partitioning of fluorophore into the polymer layer and the blinking rates of fluorophores in the polymer layer appeared to be temperature dependent. Both these observations could be further analyzed and added to the information that is gained from tracking the probe population. An interesting question to ask about partitioning would be about the relative effects of properties such as confinement zone sizes and local hydrophobicity/hydrophilicity. On/off rates of confined fluorophores have been shown to be sensitive to local environment⁹ and could be used as another measure of local confinement. SMT experiments with a series of porous glass substrates of varying pore sizes or pNIPAAm samples with varying grafting density could be used to probe the dependence of confinement zone. A second set of porous glass substrates with constant pore size and monolayer coatings of varying hydrophilic character could be used to understand the influence of local hydrophilicity.

7.2.3 Additional SMT experiments in pNIPAAm- temperature. The temperature dependent SMT data presented in this thesis focuses on the endpoints of the LCST transition in samples (23 and 32°C). It would be interesting to further characterize the phase transition by studying SMT behavior at intervals between 20 and 35°C. These datasets would be particularly interesting

when coupled with information about the z-position of the probes from NR experiments at corresponding temperatures.

7.2.4 Additional SMT experiments in pNIPAAm- other. As discussed previously, the LCST of pNIPAAm depends on factors other than temperature, and it would be interesting to study how they affect the SMT trajectories in pNIPAAm. Readily adjustable parameters include molecular weight, which can be achieved with reaction time modulation; grafting density, which can be controlled by initiator density;¹⁰ and salt concentration, pH, or solvent, which are simple experimental changes. It would be particularly relevant to measure the grafting density and molecular weight of pNIPAAm in future experiments so that the conclusions drawn can be compared with Yim *et al.* results.⁵

7.2.5 Hydrophilic-hydrophobic dye series. Initial results with a DiIC₅, DiIC₁₂, DiIC₁₈ series carried out in collaboration with Moussa Barhoum at University of Utah in Prof. Joel Harris' lab suggest that SMT with fluorophores with varying lipophilic character could be used to explore the interplay between the hydrophilic and hydrophobic switching. The first set of movies that we obtained was inconclusive but promising and this idea is worth pursuing further. This would be particularly useful in understanding controlled drug delivery devices and synthetic cell substrates, as the local hydrophilic/hydrophobic balance is crucial for both of these applications.

7.2.6 pNIPAAm sample longevity. An important question that many studies fail to address concerns the long term stability of materials subjected to a large number of temperature cycles through the LCST as well as the effects of storage in different environments. So far in the work

with pNIPAAm discussed in this thesis, these questions have been largely ignored. A general convention used in these experiments is that newer samples are always better and that longer than samples should not be stored ~2 weeks in storage in order to maintain pNIPAAm samples for SMT experiments, however this has not been specifically examined. Length of time between silane monolayer formation and ATRP polymerization is the one factor has been tested and characterized. These experiments showed that samples carried immediately from silanization to polymerization within less than 1 hour result in more homogeneous and reproducible polymer thickness compared to samples prepared with 6-24 hours delay between the two steps. Surprisingly, this held true even for silanized samples that were stored in an inert atmosphere. In addition, a higher degree of cleanliness for SMT pNIPAAm samples was maintained in DI water filled containers than in air filled, sealed containers. However, no long term trials regarding polymer brush stability have been done and no cycling experiments have been carried out.

7.2.7 SMT experiments with other responsive polymers. The study of thermo-responsive polymers other than pNIPAAm, which shows neurotoxicity in monomer form,^{11,12} and voltage-responsive polymers could readily be carried out with the existing SMT instrumentation and analysis. Voltage-responsive polymers are a particularly attractive option for molecule gating, since applied electric fields have already been incorporated into many versions of molecular gates devices for separations.

7.2.8 From materials properties to device function. The motivation for basic SRP research asserts that nanoscale understanding of the structure and dynamics of the brush would result in construction of better devices with enhanced control in molecular gating applications. It would

interesting to use SMT data to estimate device function, then test whether these estimates translate to predictable behavior in simple molecular gating or drug diffusion experiments. The applications of these trials could be similar to previous experiments involving diffusion of FITC labeled-Dextrans across a pNIPAAm coated NCAM.^{13,14} However, in this case the devices would be constructed using information gained about copolymers, molecular weight, grafting density, salt concentration, etc.

7.3 References

- (1) Dickson, R. M.; Norris, D. J.; Tzeng, Y. L.; Moerner, W. E. *Science* **1996**, 274, 966-969.
- (2) Toprak, E.; Balci, H.; Blehm, B. H.; Selvin, P. R. *Nano Lett.* **2007**, 7, 2043-2045.
- (3) Laloyaux, X.; Mathy, B.; Nysten, B.; Jonas, A. M. *Langmuir* **2010**, 26, 838-847.
- (4) Yim, H.; Kent, M. S.; Huber, D. L.; Satija, S.; Majewski, J.; Smith, G. S. *Macromolecules* **2003**, 36, 5244-5251.
- (5) Yim, H.; Kent, M. S.; Mendez, S.; Lopez, G. P.; Satija, S.; Seo, Y. *Macromolecules* **2006**, 39, 3420-3426.
- (6) Yim, H.; Kent, M. S.; Satija, S.; Mendez, S.; Balamurugan, S. S.; Balamurugan, S.; Lopez, G. P. *Phys. Rev. E* **2005**, 72, 051801.
- (7) Yim, H.; Kent, M. S.; Satija, S.; Mendez, S.; Balamurugan, S. S.; Balamurugan, S.; Lopez, C. P. *J. Polym. Sci., Part B: Polym. Phys.* **2004**, 42, 3302-3310.
- (8) Yim, H.; Kent, M. S.; Mendez, S.; Balamurugan, S. S.; Balamurugan, S.; Lopez, G. P.; Satija, S. *Macromolecules* **2004**, 37, 1994-1997.
- (9) Dickson, R. M.; Cubitt, A. B.; Tsien, R. Y.; Moerner, W. E. *Nature* **1997**, 388, 355-358.
- (10) Bao, Z. Y.; Bruening, M. L.; Baker, G. L. *Macromolecules* **2006**, 39, 5251-5258.

- (11) Tanii, H.; Hashimoto, K. *Toxicol. Lett.* **1991**, 58, 209-213.
- (12) Vihola, H.; Laukkanen, A.; Valtola, L.; Tenhu, H.; Hirvonen, J. *Biomaterials* **2005**, 26, 3055-3064.
- (13) Lokuge, I.; Wang, X.; Bohn, P. W. *Langmuir* **2007**, 23, 305-311.
- (14) Lokuge, I., University of Illinois, U-C, 2006.

APPENDIX A

A.1 Supplementary material from Chapter 5

Additional Confinement Level Results

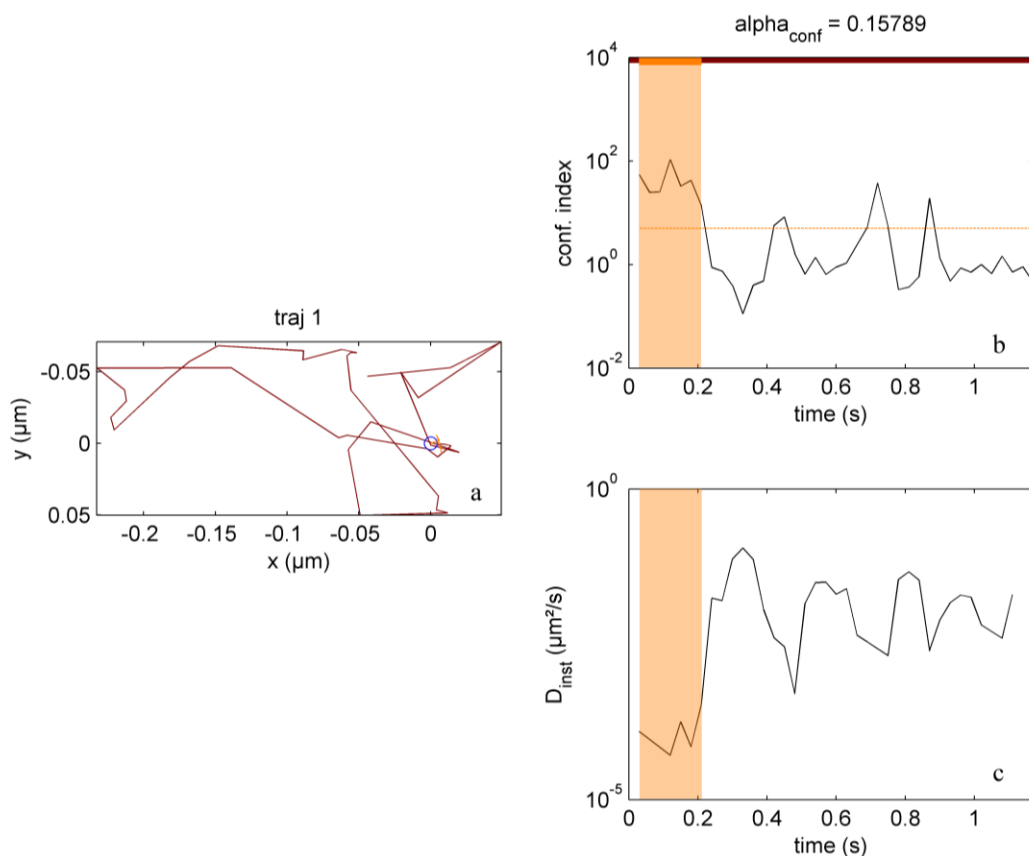


Figure A.1: Confinement level results for Molecule 1. In panel **a** the trajectory is shown with ‘free’ periods in red and ‘confined’ periods in orange, the start marked by a blue circle. Panel **b** shows the confinement level L throughout the trajectory. ‘Confined’ periods are shaded orange and the fraction of confinement α_{conf} is listed above the plot. The minimum confinement level L_{\min} is displayed as the horizontal orange line across the plot. Panel **c** shows the instantaneous diffusion coefficient throughout the trajectory. Note the log-scale ordinate in **b** and **c**.

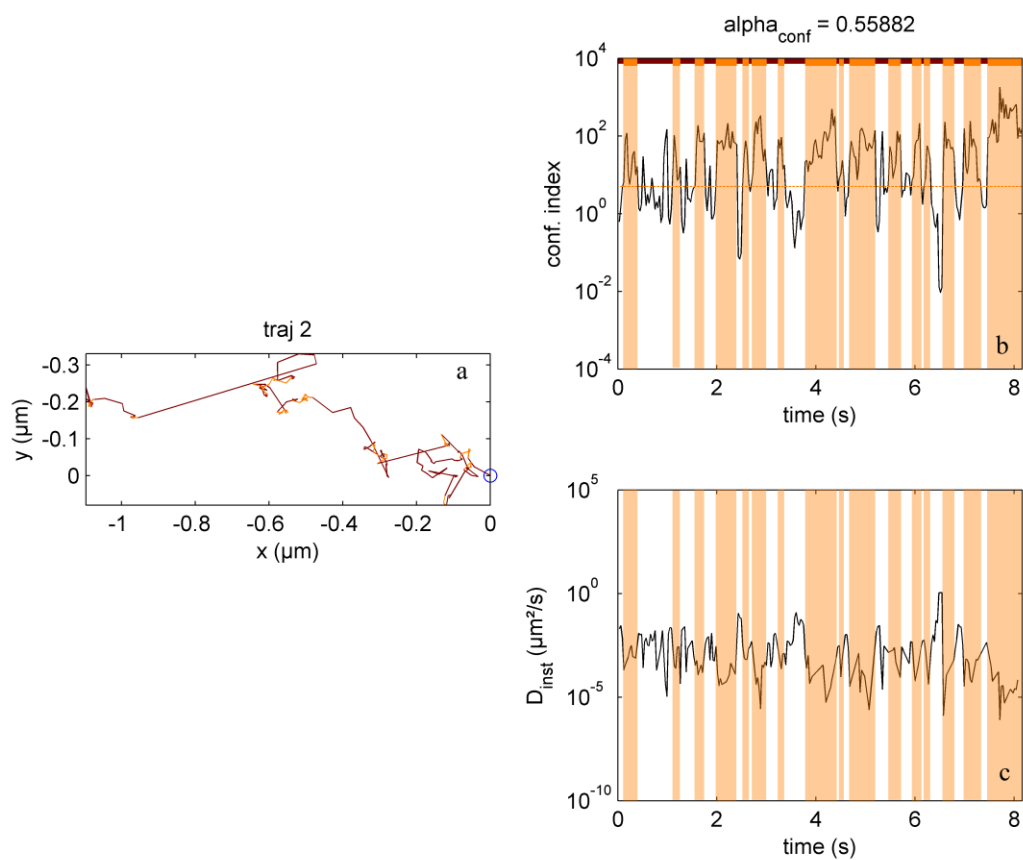


Figure A.2: Confinement level results for Molecule 2. Plot details as in Fig. A.1.

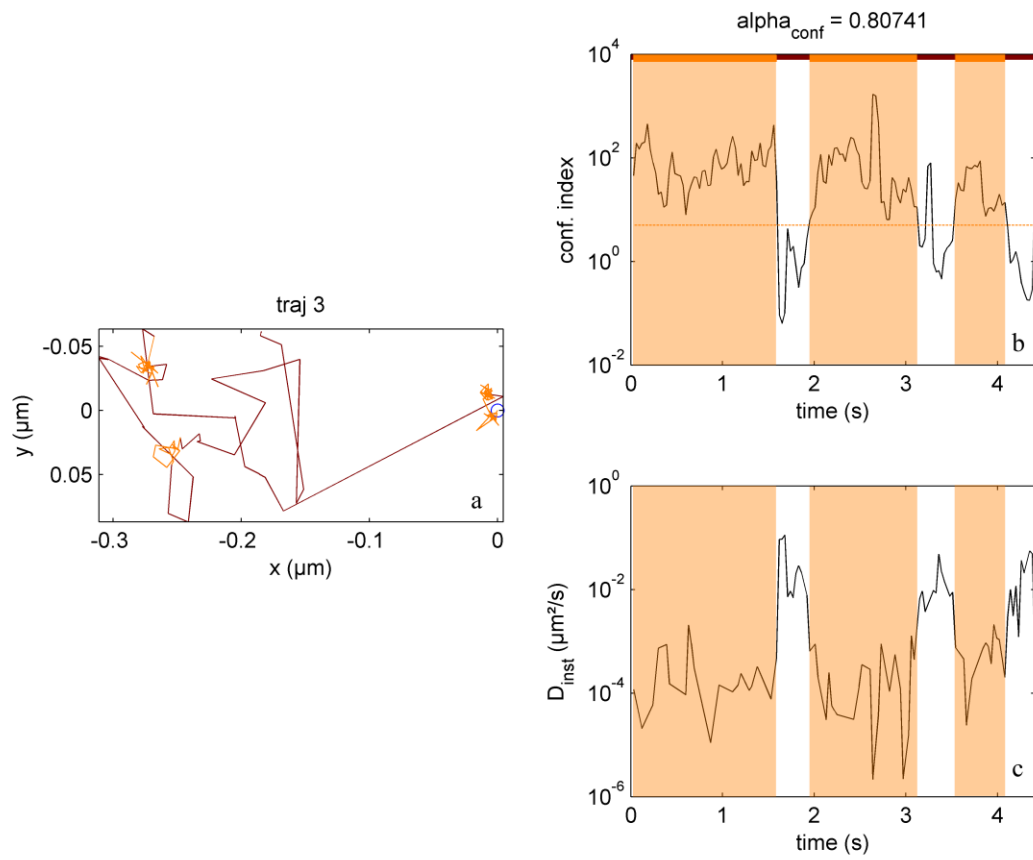


Figure A.3: Confinement level results for Molecule 3. Plot details as in Fig. A.1.

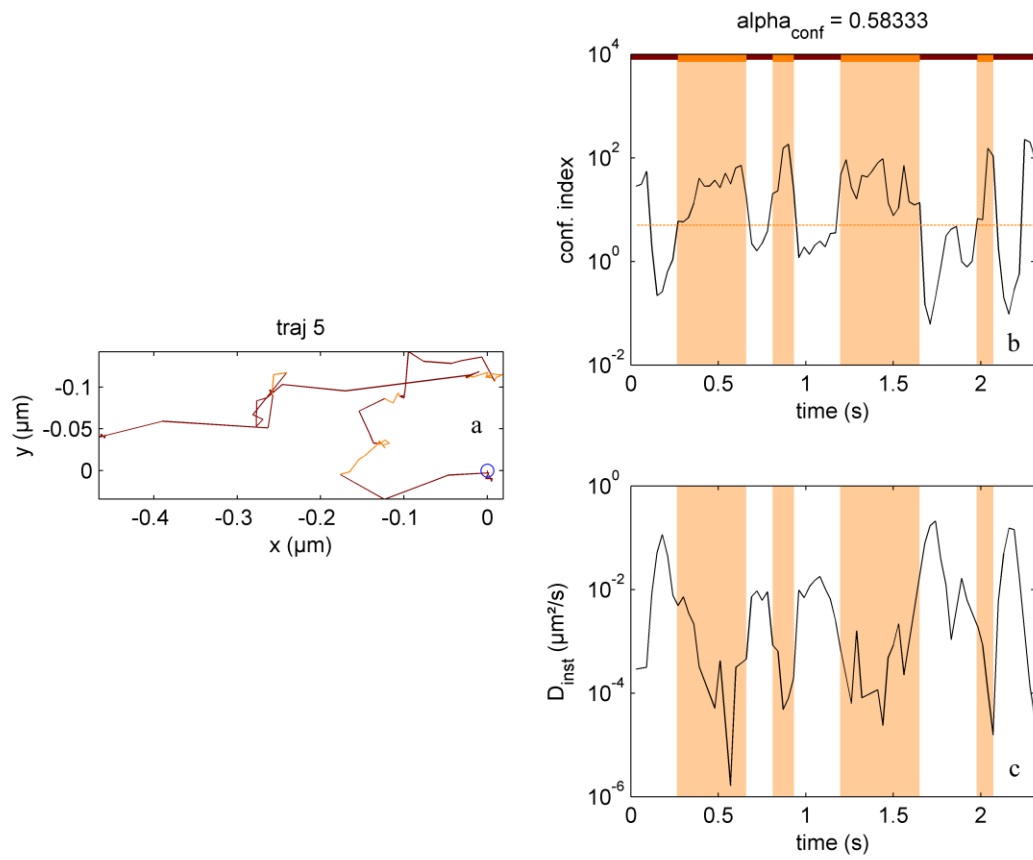


Figure A.4: Confinement level results for Molecule 5. Plot details as in Fig. A.1.

Additional Time Series Analysis Results

Figures and output tables from Times series analysis. Descriptions of all the values and equations for the models can be found in Section 5.4.3.

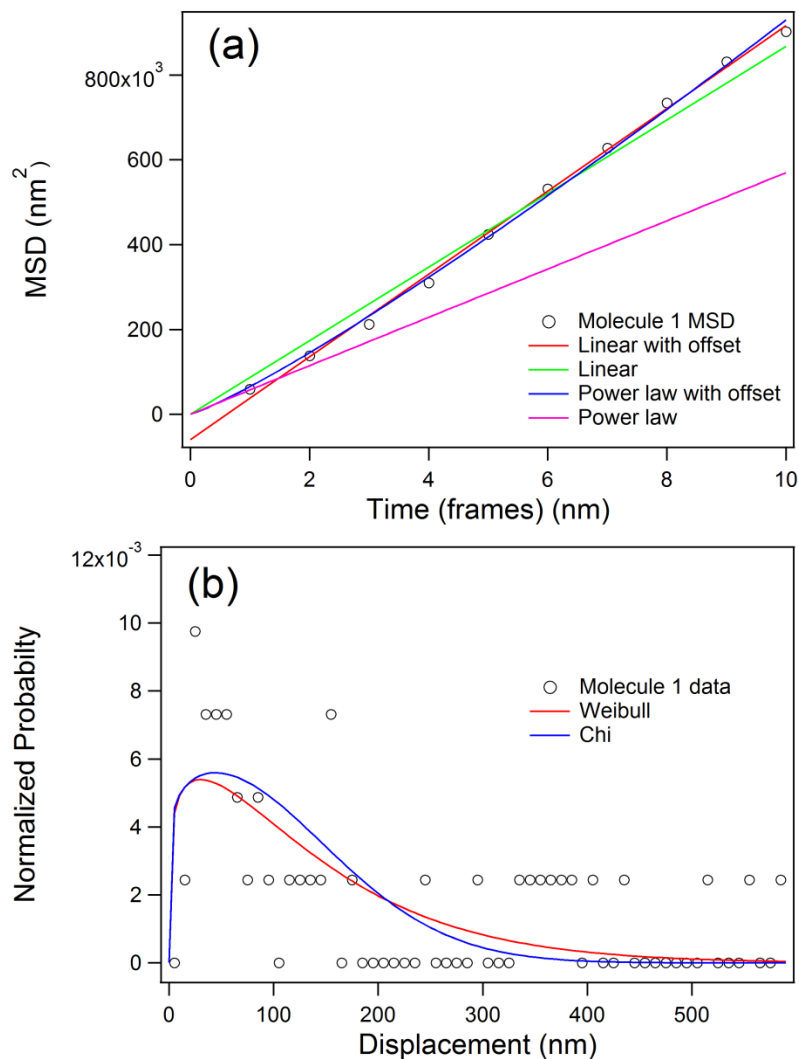


Figure A.5: Time series analysis results for Molecule 1. Panel (a) shows MSD data and fitting with two linear and two power law models, panel (b) shows step size distribution data and fitting with general Weibull and Chi models.

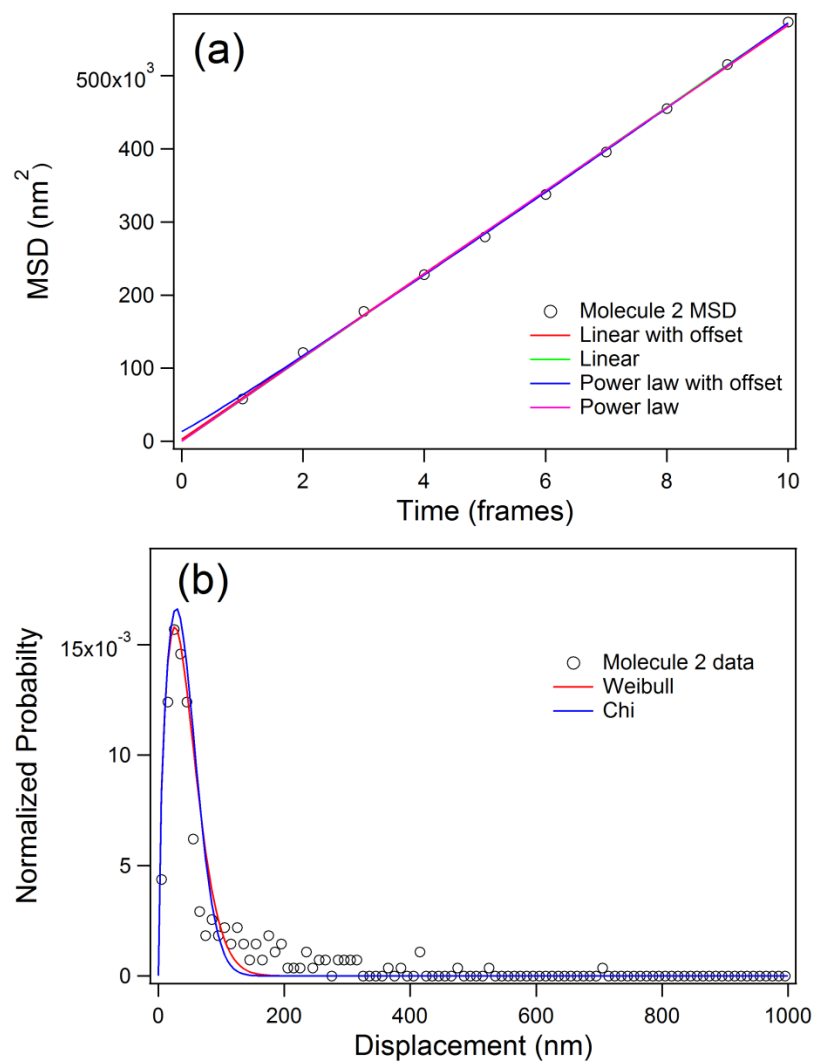


Figure A.6: Time series analysis results for Molecule 2. Plot details as in Fig. A.5.

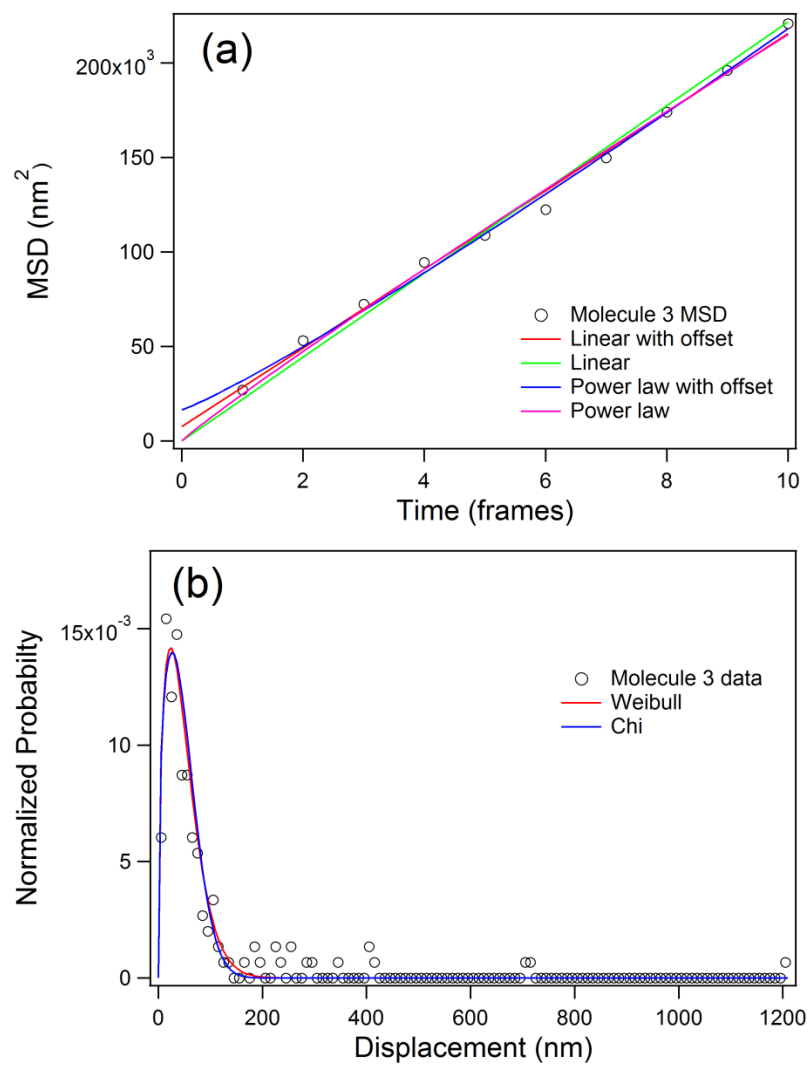


Figure A.7: Time series analysis results for Molecule 3. Plot details as in Fig. A.5.

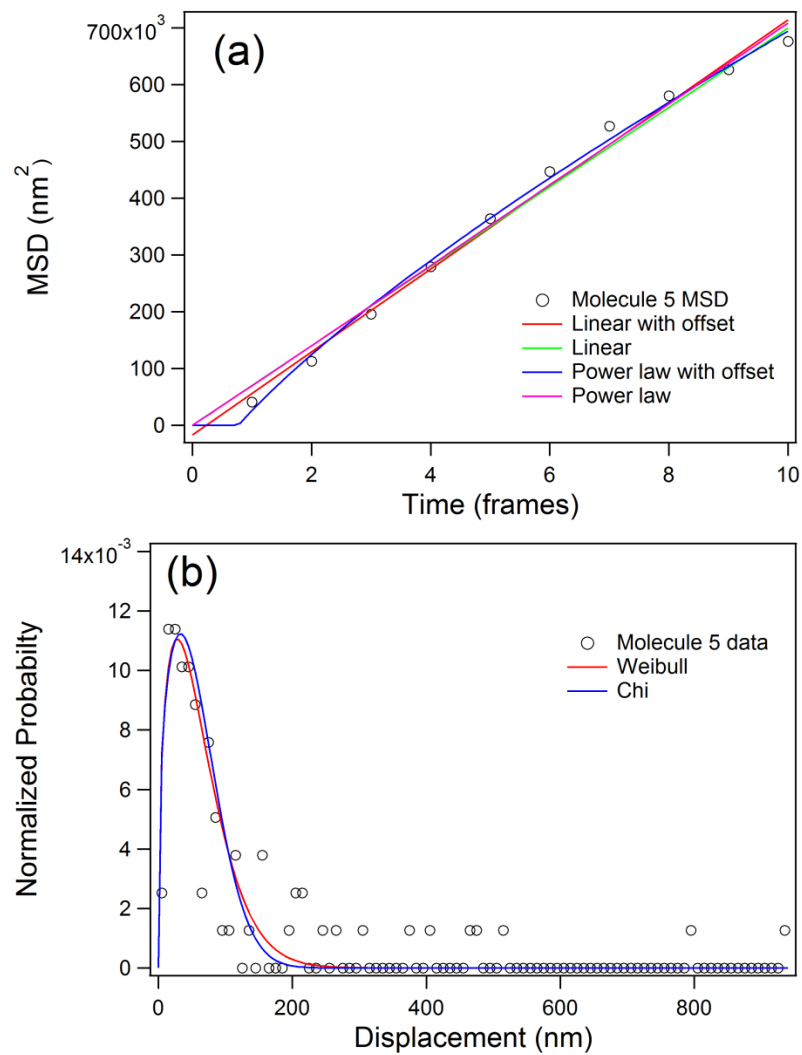


Figure A.8: Time series analysis results for Molecule 5. Plot details as in Fig. A.5.

Table A.1 shows the fitting parameters and least squares residuals found for the mean squared displacement vs. time delay for the linear with offset and power law with offset for all molecules.

Table A.1: Estimates output from time series analysis for all molecules.

Molecule	A1 ^a	B1	R1	a1 ^b	b1	α 1	r1
1	97638	-59733	13804	65310	-0.0537	1.1535	46064
2	56646	2893	4035	50244	13196	1.0464	11075
3	20794	7574	4272	24662	-0.0278	0.9404	15308
4	41121	28483	5511	59675	-0.0678	0.8616	15664
5	73111	-17146	20758	144536	-118577	0.7499	43553

^aA1, B1, and R1 are the optimized parameters and residual, respectively, from the least square fitting for the linear equation with offset: $y = A1 * x + B1$

^ba1, b1, α 1 and r1 are the optimized parameters and residual, respectively, from the least square fitting for the power law equation with offset: $y = a1 * x^{\alpha 1} + b1$

Additional Statistical Analysis and Multistate Kinetics Results

The fitting parameters for the step size distribution fitting from the statistical analysis and multistate kinetics are shown in Table A.2.

Table A.2: Parameters determined from the step size distribution fitting.

	1 state	2 states	3 states	4 states
D ₁	0.4174	0.0239	0.0177	0.0141
D ₂	---	1.7412	10.0799	17.6058
D ₃	---	---	0.4159	0.1304
D ₄	---	---	---	0.9355
x ₁	1	0.7709	0.690	0.600
x ₂	---	0.2291	0.029	0.014
x ₃	---	---	0.282	0.251
x ₄	---	---	---	0.135

States 1-4 include the diffusion coefficient(s) first and then the fraction of each population for the step size pdf fits in Figure 5.13. The most likely number of states is then determined by applying the Akaike information criterion and the diffusion coefficient(s), and the fraction of states for each sub-population is taken from these values for the ensemble of all molecules.

AUTHOR'S CURRICULUM VITAE

LINDSAY C.C. ELLIOTT

·232 Village Dr, Apt D ·Mishawaka, IN 46545 ·(217) 649-1862 ·lelliott2@nd.edu

OBJECTIVE

To obtain a post-doctoral position involving analytic and materials chemistry related energy and sustainable resources research.

EDUCATION

Ph.D. Materials Chemistry	University of Illinois at Urbana-Champaign	1/2011
	Advisors: Paul W. Bohn, Paul V. Braun	GPA: 3.63/4.00

Relevant coursework- Design and Use of Biomaterials, Surfaces and Colloids, Experimental Spectroscopy, Physical Methods in Materials Chemistry, Topics in Inorganic Chemistry

B.S. Chemistry with Distinction	Purdue University, West Lafayette, IN	5/2003
Physics minor		GPA: 3.91/4.00

RESEARCH EXPERIENCE

Research Associate	University of Notre Dame	1/2011-present
	Advisor: Paul W. Bohn	

- Examined the reaction of bacteria with surface bound siderophores in real-time using surface plasmon resonance angle imaging
- Studied the temperature dependent z-profile concentration of fluorophores in surface tethered poly(n-isopropylacrylamide) brushes through neutron reflectometry experiments

Graduate Research Assistant	University of Illinois at Urbana-Champaign	12/2004-1/2011
	Advisor: Paul W. Bohn	

- Investigated free volume changes in stimulus responsive polymer brushes
- Synthesized surface initiated polymer brushes
- Designed and constructed widefield and total internal reflection fluorescence microscopes
- Programmed Matlab data analysis software
- Carried out single molecule tracking and diffusion analysis

L.C.C. Elliott, M. Barhoum, J.M. Harris, P.W. Bohn. *Trajectory Analysis of Single Molecules Exhibiting Non-Brownian Motion*, *Phys Chem Chem Phys*, **2011**, DOI: 10.1039/c1030cp01805h.

L.C.C. Elliott, M. Barhoum, J.M. Harris, P.W. Bohn. *Single Molecule Tracking Studies of Lower Critical Solution Temperature Transition Behavior in Poly(N-isopropylacrylamide)*, **2011**, submitted.

Dissertation, *Single Molecule Tracking Studies of Lower Critical Solution Temperature Transition Behavior in Poly(N-isopropylacrylamide)*

RESEARCH EXPERIENCE (cont.)

Graduate Research Assistant University of Illinois at Urbana-Champaign 6-9/2003
Advisor: Ralph G. Nuzzo

- Developed a PDMS based, membrane-less micro fuel cell
- Engineered multilayer devices using rapid prototyping and soft lithography
- Fabricated electrodes through metal film thermal and e-beam deposition
- Measured and compared electrochemical properties of the micro fuel cell

S.M. Mitrovski, L.C.C. Elliott, R.G. Nuzzo. *Microfluidic Devices for Energy Conversion: Planar Integration and Performance of a Passive, Fully Immersed H₂-O₂ Fuel Cell*, *Langmuir*, **2004**, 20(17), 6974-6976.

Undergrad Research Assistant Purdue University 4/2000-5/2003
Advisor: Jillian M. Buriak

- Constructed surfaces composed of covalently bound molecular wires
- Synthesized novel organometallic compounds utilizing air-free procedures and chromatography
- Produced porous silicon with semiconductor processing techniques
- Functionalized por-Si with Ru²⁺, Co²⁺, Cu²⁺, and Zn²⁺-pyridine based coordination polymers
- Characterized compounds and surfaces through NMR, IR, and UV-vis
- Studied electroless deposition of Au, Ag, and Pt nanoparticle films onto Ge and GaAs

Undergraduate thesis, *Metal-Oligopyridine Complexes Covalently Bonded to Porous Silicon*, **2003**.

L.A. Porter Jr, H.C. Choi, J.M. Schmeltzer, A.E. Ribbe, L.C.C. Elliott, J. M. Buriak. "Electroless Nanoparticle Film Deposition Compatible with Photolithography, Microcontact Printing, and Dip-pen Nanolithography Patterning Technologies", *Nano Letters* **2002**, 2, 1369.

SKILLS

Foreign Language: basic conversational and scientific German

Software/Programming: MATLAB, ImageJ, Igor Pro, ChemOffice, Endnote, Adobe Photoshop, SigmaPlot, Origin, FORTRAN, C, UNIX, Access, Frontpage, Galactic Grams32 AI, OpenLab, LABVIEW

SELECTED PRESENTATIONS

- 2008 MRS Fall Meeting, Boston, MA, Paper, *Studies of Structural Heterogeneities in Temperature and Voltage Responsive Hydrogels through Single Particle Tracking*, Dec 4, **2008**.
- 59th Pittsburgh Conference on Analytical Chemistry and Applied Spectroscopy, New Orleans, LA, Paper, *Towards Characterization of Nanoscale Perturbation-Induced Swelling in Hydrogel Polymer Brushes through Single Molecule Tracking*, March 2-8, **2008**.
- International Symposium on Stimulus-Responsive Materials, Hattiesburg, MS, Poster, *Single molecule tracking studies of free volume transition in nanoscale hydrogel films*, Oct. 30-Nov. 1, **2007**.

SELECTED PRESENTATIONS (cont.)

- 58th Pittsburgh Conference on Analytical Chemistry and Applied Spectroscopy, Chicago, IL, Paper, *Single Molecule Tracking for the Characterization of Nanoscale Perturbation-induced Swelling in Hydrogel Polymer Brushes*, Feb. 25-Mar. 2, **2007**.
- 215th ACS National Meeting, New Orleans, Sci-Mix and Inorganic Division Poster - *Metal-Oligopyridine Complexes Covalently Bonded to Semiconductor Surfaces*, March 23-27, **2003**.
- Butler Undergraduate Research Conference, Indianapolis, IN, Paper, *Coordination Polymers on Porous Silicon*, April 12, **2002**.
- Purdue University Undergraduate Research Day, West Lafayette, IN, Poster, *Ruthenium Polymers on Porous Si*, April 7, **2001**.
- Butler Undergraduate Research Conference, Indianapolis, IN, Paper, *Ruthenium Polymers on Porous Silicon*, April 13, **2001**.

INSTRUMENTATION

Varian Gemini 200, INOVA 300, Varian Unity 400 and 500 MHz NMR Spectrometers
Nicolet Nexus 670 FT and Biorad Digilab FTS-60A Infrared Spectrophotometers
Varian Cary 300 Bio UV-Vis Spectrophotometer
Varian CP-3800 Gas Chromatograph
Temescal FC-1800 Electron-beam Evaporator
Materials Research Laboratory Class 100 Clean Room
Karl Suss MJB3 Mask Aligner
Leica SP2 Confocal and Multiphoton Microscope
Gaertner L116C Fixed Wavelength Variable Angle Stokes Ellipsometer
Varian NRC 3117 Thermal Evaporator
Carl Zeiss Axiovert 200 Fluorescence Light Microscope
Digital Instruments Multimode Nanoscope IIIa Atomic Force Microscope
FEI Company Philips XL30 ESEM-FEG
Asylum Research MFP-3D Atomic Force Microscope
Sloan Dektak³ ST Stylus Surface Profilometer
Kratos Axis ULTRA X-ray Photoelectron Spectrometer

HONORS AND AWARDS

National Defense Science and Engineering Graduate Fellowship	2005
National Science Foundation Graduate Research Fellowship	2005
University of Illinois Roger Adams Fellowship	2004
NSF GRF Honorable Mention	2003
Purdue School of Science Outstanding Senior	2003
Margerum Award Recipient	2003
ACS Division of Inorganic Chemistry Travel Grant	2003
Reilley Pharmacia Chemistry Merit Scholarship	2003
Purdue University Dean's List and Semester Honors	9/1999-5/2003
Bruce Helfert Memorial Award	2002
Phi Beta Kappa Member	2002
WLCSC Community Honor Roll	2002
National Merit Scholar	1998
Tri-Kappa State Scholarship Recipient	1999

SERVICE EXPERIENCE AND COMMUNITY INVOLVEMENT

Habitat for Humanity	6/2006-present
Northwest Florida and Philo Neighborhood Watch	8/2005-3/2007
Department of Chemistry Graduate Student Advisory Committee	3/2005-3/2007
Graduate Seminar in the Applied Chemical Sciences	1/2006-3/2007
AmeriCorps Alums Month of Service	6/2006
Orpheum Children's Museum Science Day	4/2005
AmeriCorps*NCCC	9/2003-7/2004

ACTIVITIES AND ORGANIZATIONS

American Chemical Society Member	3/2005-present
Materials Research Society Member	3/2005-present
United Soccer Federation of Central Illinois	3/2005-3/2007
American Chemical Society Student Affiliate	9/2001-5/2003
Purdue University Golden Honors Day	10/2002
Women's Club Lacrosse	2/2001-12/2002
West Lafayette HS Assistant Girls Soccer Coach	7/2000-10/2002
Purdue Symphony Orchestra	1/2000-5/2002
National Chemistry Week Volunteer	10/2001
Society of Women Engineers Rube Goldberg Team	1-4/2001

REFERENCES

Professor Paul W. Bohn
University of Notre Dame
Chem & Bio Engr/Chemistry
301 Cushing Hall of Engineering
Notre Dame, IN 46556
(574) 631-1849
pbohn@nd.edu

Professor Joel M. Harris
University of Utah
Chemistry
Henry Eyring Building
315 S 1400 E Room 2020
Salt Lake City, UT 84112
(801) 581-3585
harrisj@chem.utah.edu

Assistant Professor Susan Fullerton
University of Notre Dame
Center for Nano Science & Technology
Electrical Engineering
317 Cushing Hall
Notre Dame, IN 46556
(574) 631-1367
susan.fullerton.3@nd.edu

Professor Paul V. Braun
University of Illinois, Urbana-Champaign
Materials Science & Engineering
1304 W Green, M/C 246
Urbana, IL 61801
(217) 244-7293
pbraun@illinois.edu